ABSTRACT

Title of Dissertation:	THE HYGROSCOPICITY OF PLASTIC AEROSOLS
	Chun-Ning Mao, Doctor of Philosophy, 2023
Dissertation directed by:	Professor Akua Asa-Awuku, Department of Chemical and Biomolecular Engineering

Polymeric nanoparticles affect many aspects of human life. They directly absorb or scatter sunlight, or indirectly act as cloud condensation nuclei (CCN) to change the Earth's climate. Additionally, micro-plastics released into the environment have the potential to degrade into nano-size particles. Plastic nanoparticles' sizes, number concentration, and hygroscopicity are important properties to understanding nano-plastics' fates. In this work, I explored aerosol measurement techniques, aerosol hygroscopicity, and polymer nanoparticles to understand subsequent effects in the environment and on human health. The project was divided into three objectives:

For the first objective, I developed the single-parameter hygroscopicity model for polymeric aerosols with Flory-Huggins Köhler theory. Traditional hygroscopicity, derived from Raoult's law, depends on the molecular volume of the solute. For polymers with a high

molecular volume, the predicted hygroscopicity from traditional Köhler theory is zero. However, the experimental results showed that polymers could take up water and readily act as CCN. I developed the expression of the hygroscopicity for polymers and showed the relation between the polymer-water interaction parameter and the water-uptake ability. I also considered water-insoluble polymers and the water-adsorption model combined with Köhler theory to define water-uptake. Thus the CCN activity of polystyrene and surface modified polystyrene particles were also measured.

For the second objective, I predicted the fraction of the multiply charged particles, showing that the extinction cross section measured by Cavity Ring Down Spectroscopy (CRD) was influenced by a small amount of multiply charged particles using a Differential Mobility Analyzer (DMA). The initial results indicated that ~4% to ~6% of the total number concentration are triply and quadruply charged particles at 200 nm electrical mobility. This small percentage if neglected could induce errors greater than 5% in subsequent extinction cross section measurements. Thus, the errors induced with commercially available DMAs in the extinction cross section measurement were evaluated.

For the third objective, I studied the fate of the nano-plastics in the environment. Results showed that low density polyethylene (LDPE) powders generated particles less than 100 nm at temperatures above 40 ^{o}C. I quantified the number concentration of 5 materials in water via traditional atmospheric aerosol measurement techniques. The five materials are cellulose, SiO_2,

LDPE, polyethylene terephthalate (PET), and polyvinyl chloride (PVC). They were all common materials used for food packaging. Furthermore, the hygroscopicities of the nano-plastics were measured. I demonstrated that the nano-plastics could act as CCN under a supersaturated environment and hence affect the climate. The results showed that the plastic materials (LDPE, PVC, PET) were more hygroscopic than cellulose. The nano-plastics could travel further and be found in remote and cold areas like Antarctica, the Arctic, and high mountains. The work in this objective provided evidence of wet deposition being a possible route for nano-plastics to come to the ground.

Plastics are relatively new materials compared to papers, clays, and glasses, but have already been massively produced. The work in this thesis contributed to our understanding of the impact on nano-plastics to the environment. The interaction of the water and nano-plastics in the environment was studied. The measurements of size distribution and hygroscopicity of nano-plastics can be applied in the climate model to reduce the uncertainties in the indirect effect of the aerosols in future studies.

THE HYGROSCOPICITY OF PLASTIC AEROSOLS

by

Chun-Ning Mao

Dissertation submitted to the Faculty of the Graduate School of the
University of Maryland, College Park, in partial fulfillment
of the requirements for the degree of
Doctor of Philosophy
2023

Advisory Committee:
Professor Akua Asa-Awuku, Chair
Professor Srinivasa R. Raghavan
Professor Kyu Yong Choi
Dr. James G. Radney
Professor Russell R. Dickerson, Dean's Representative

Dedication

To my parents.

To my father who taught me science.

To my mother who taught me English.

Acknowledgements

I want to thank my family for the great support during my PhD program. To my husband, who comes to and stays in University of Maryland for me, who is always be there with me. I would like to give special thanks to my advisor, Dr. Akua Asa-Awuku. It is my greatest fortune to know her and be guided by her. To my mentors, Dr. Christopher Zangmeister and Dr. James Radney, who give a lot of helps. To group EARL, my co-workers as well; I am lucky to know you all.

Thanks to everybody who encourages, supports, and be there with me during my PhD program. From the bottom of my heart, thank you.

Table of Contents

List of Tables

List of Figures

List of Abbreviations

AG	aerosol generator
AOM	acousto-optic modulator
APM	aerosol particle mass analyzer
AS	ammonium sulfate
CCN	cloud condensation nuclei
CCNC	cloud condensation nuclei counter
CCNN	the concentration of particles that form droplets counted by CCNC
CN	the total particle concentration counted by condensational particles counter
CPC	condensational particles counter
CRD	cavity ring down spectroscopy
DD	diffusion dryer
DLS	dynamic light scattering
DMA	differential mobility analyzer
FHH-AT	Frenkel-Halsey-Hill adsorption theory
FHK	Flory-Huggins- Köhler
FTIR	Fourier transform infrared spectroscopy
Imp	impactor

IPCC	Intergovernmental Panel on Climate Change
LDPE	low density polyethylene
NTA	nanoparticle tracking analysis
OPC	optical particle counter
PCIe	Peripheral Component Interconnect express
PEG	polyethylene glycol
PET	polyethylene terephthalate
PSL	Polystyrene Latex particles
PVC	polyvinyl chloride
RH	relative humidity
RI	refractive index
RK	Raoult-Köhler
SEM	scanning electron microscopy
SMCA	scanning mobility CCNC analysis
SMPS	scanning mobility particle sizer
TDMA	tandem DMA
TEM	transmission electron microscopy
TK	traditional Köhler

List of Symbols

A	a coefficient related to the droplet properties
A_{FHH}	compound specific empirical parameters in FHH-AT model, represent the interaction of water and nuclei surface
B_{FHH}	compound specific empirical parameters in FHH-AT model, represent the interaction of water molecules and bulk nuclei
C	the Cunningham slip correction factor
C_{ext}	extinction cross section
$C_{ext,calc}$	the theoretically calculated C_{ext} using Mie theory and only those particle sizes that could be identified in the TDMA data
$C_{ext,dist}$	average extinction cross-section
$C_{ext,ens}$	ensemble extinction cross-section
D	wet diameter
D_c	measured critical dry diameter
D_d	particle dry diameter
D_m	electrical mobility diameter
$D_{p,c}$	critical wet droplet diameter
D_{ve}	volume-equivalent diameter

D_w	the diameter of a single water molecule (0.275 nm)
F	the reciprocal of the chain segments of the polymer
G_f	hygroscopic growth factor
I_0	the initial intensity
I	the measured laser intensity at time
L	length between exit slit and polydisperse aerosol inlet
L_{aero}	length of the cavity filled with aerosols
L_{cavity}	length of the total cavity
M_s	molecular weight of the solute
M_w	molecular weight of water (18.02 g mol^{-1})
N	particle number concentration
P	pressure
Q_{sh}	sheath flow rate
R	the gas constant (8.314 J K^{-1} mol^{-1})
R^2	coefficient of determination
S	saturation ratio
T	temperature
V	voltage difference

V_s	total volume of solute
V_w	total volume of water
Z_p	electrical mobility
a_w	water activity
c	speed of light
e	elementary charge ($\approx 1.602 \times 10^{-19}$ C)
k	imaginary part of refractive index
m	refractive index
m_{p}	particle mass
n	real part of refractive index
q	the number of elementary charges on the particle
r	radius of the new origin
r_1	inner radius of annular space
r_2	outer radius of annular space
s	supersaturation
t	time
v_s	Van't Hoff coefficient of the solute
x_w	mole fraction of water

α_{ext}	extinction coefficient
β	decay constant
$\beta_{abs,aero}$	decay constant of the absorption of light by aerosols
$\beta_{abs,gas}$	decay constant of the absorption of light by gases
β_{mirror}	decay constant of mirror losses
$\beta_{scat,aero}$	decay constant of the scattering of light by aerosols
ε	the tolerance of error
θ	surface coverage
θ_c	critical surface coverage
κ	hygroscopicity
$\kappa_{FHH,exp}$	experimental adsorption hygroscopicity
$\kappa_{FHH,the}$	theoretical adsorption hygroscopicity
κ_{FHK-s}	simplified Flory-Huggins-Köhler hygroscopicity
κ_{sub}	hygroscopicity at sub-saturation environment
λ_c	classification parameter
λ_g	mean free path of the gas
ρ_s	density of the solute
ρ_w	density of water (1000 kg m^{-3})

σ_w	surface tension of the droplet
μ	gas viscosity
τ	ring-down time
φ	volume fraction of the polymer
φ_c	critical polymer volume fraction
χ	the Flory-Huggins interaction parameter
ω	rotation speed

Chapter 1: Introduction

1.1 Nano-plastics as aerosols

Aerosols are small particles suspended in the air that have the potential to affect both air quality and climate (D. P. Singh et al. 2007). They can be either solid or liquid, including dust and smoke, and can be both natural and man-made in origin. They affect several aspects of human life. They influence climate by scattering and absorbing radiation, leading to changes in temperature and precipitation patterns. Aerosols also indirectly act as cloud condensation nuclei (CCN). CCN interact with water molecules, form clouds, and change climate and the energy balance of Earth (Seinfeld, Pandis, and Noone 1998).

Aerosols can range from micrometers to nanometer in diameters (10^{-8}~10^{-4} m). Since the size of aerosols is small, they can travel for long distances, even across the sea. For example, Saharan dust particles can transport across the northern Atlantic and are observed in satellite images (Kallos et al. 2006; d'Almeida 1986). These kind of mineral dust aerosols can affect air quality by reducing visibility and increasing the concentration of pollutants in the air.

Small inhalable particles can also be exploited to enhance our quality of life. Specifically, aerosol therapy is a non-invasive common drug delivery for nano- or micro-sized drug particles. They are studied to cure asthma, and even diabetes (Muralidharan et al. 2015; Gill et al. 2007;

Malcolmson and Embleton 1998; Agnihotri, Mallikarjuna, and Aminabhavi 2004; Azarmi, Roa, and Löbenberg 2008). In conclusion, nano-sized aerosols can have impacts on the environment and human health.

The lifetime of aerosols depends on their size, composition, and other environmental factors. Larger aerosols tend to settle out of the atmosphere more quickly than smaller aerosols. Smaller aerosols can remain suspended for longer periods of time. Typically, aerosols can stay in the atmosphere for 7 to 10 days. Aerosols can be deposited onto surfaces through two primary processes: dry deposition and wet deposition. Dry deposition is the free fall to Earth directly from the atmosphere. Dry deposition occurs when aerosols settle onto surfaces through gravitational settling or by being absorbed onto surfaces. Wet deposition is the process whereby atmospheric gases mix with suspended water in the atmosphere. Wet deposition occurs when aerosols are removed from the atmosphere through precipitation, like rain or snow (Seinfeld, Pandis, and Noone 1998).

There are several sources of aerosols. Natural sources include sea salt spray, volcanic eruptions, and dust storms. Anthropogenic aerosols can come from industrial processes, transportation, agriculture, household product or waste management (Pöschl 2005). Among these sources, airborne plastic in nano–sizes are an emerging concern and will be a focus in this thesis work.

Plastics are used everywhere and therefore their transport route to the atmosphere, water, soil and biological systems is of interest. Geyer, Jambeck, and Law estimated that 8300 million metric tons (of virgin plastics) have been produced and approximately 6300 million metric tons of plastic waste has been generated since 19th century (Geyer, Jambeck, and Law 2017). They estimated 79% of the waste plastics were accumulated in landfills or the natural environment. Waste plastics released into the environment are believed to break down into smaller debris in micro- or even nano-sizes (Andrady 2011; Shah et al. 2008). They can be released into the air through a variety of sources, including sea spray (Allen et al. 2020), the use of personal care and household products (Hernandez, Yousefi, and Tufenkji 2017), and the release of microfibers from synthetic clothing during washing (Yang, Luo, and Nowack 2021). These small plastic particles have been found in cold areas far from human activity (Munari et al. 2017; Cózar et al. 2017; Allen et al. 2019).

There is no consensus in definition of nano-plastics. The word *nano* refer to particles and hole sizes that are smaller than 100 nm in nanotechnology application (Klaine et al. 2012). However, nano-plastics larger than 100 nm are still released into the environment. In most of the nano-plastics related studies, nano-plastics are defined in the size range of 1 nm to 1000 nm in diameter (da Costa et al. 2016b; Hartmann et al. 2017; Gigault et al. 2016; Yang, Luo, and Nowack 2021). In this work particles released from plastic materials and smaller than 1000

nm are called nano-plastics, particles diameter lower than 5 mm are called micro-plastics.

The presence of micro- and nano-plastics in the air can have potential health and environmental impacts (Yin et al. 2021). Inhalation of nano-plastics can lead to potential health risks, such as inflammation and genotoxicity (Prata 2018). In addition to potential health risks, the presence of nano-plastics in the air can also have environmental impacts. They can accumulate in the soil and water, potentially affecting the health of plants and animals. They can be ingested by marine life (Haegerbaeumer et al. 2019), leading to potential negative impacts in the food chain (Ma et al. 2016; Sökmen et al. 2020). However, the impact of the micro- and nano-plastic to human body has not been fully understood. Further research is needed to improve our understanding of micro- and nano-plastics fate and health effects.

Yet, nano-plastic particles possess a high surface area to volume ratio and are thought to be more dangerous than micro-plastic. It has been difficult to prove the degradation into the nano-scale because the mass concentration of nano-plastic particles is likely small and below chemical instrument detection limits (Andrady 2011). A typical method to measure nano-plastic utilizes scanning electron microscopy (SEM) and Fourier transform infrared spectroscopy (FTIR). Hernandez et al. used SEM and FTIR to investigate the nano-polyethylene in facial scrubs (Hernandez, Yousefi, and Tufenkji 2017). However, SEM images could not quantify the amount of the degraded nano-plastics. Recently, the number

concentration of nano-plastics in water were measured by nanoparticles tracking analyzer (Lambert and Wagner 2016). In 2022, Zangmeister et al. used a differential mobility analyzer (DMA) and condensational particles counter (CPC) in series and measured the full size distribution of nano-plastics generated from single used consumer plastic products (Zangmeister et al. 2022b). The DMA and CPC are commonly used instrumentation to acquire the size distribution and particle number concentration in nano-sized aerosol studies. They aerosolized nano-plastics in the water and show that aerosol measurement techniques have the ability study the nano-plastics as aerosols.

Furthermore, nano-plastics can act as both ice nuclei and CCN (Aeschlimann et al. 2022a). They may adsorb water and become droplets. As a result, nano-plastics as aerosols have the potential to affect the climate indirectly. In addition, wet deposition is hypothesized to be a possible route for nano-plastic deposition to the earth surface. The ability of aerosols to uptake water (in other words, the hygroscopicity) determines their fate and final places in the environment. The life cycle of the nano-plastics in the environment must be established. Large plastic wastes generated from human activity break down into smaller pieces in the environment. From the smaller pieces, micro- and nano-size plastic particles could be potentially released into environment through degradation in aqueous environments. These smaller particles are light, come into the atmosphere, and then travel to far places (Allen et al.

2019). When they arrive an environment with high relative humidity and low temperature, they form large droplets or snow and rain down to the surface. In summary, the hygroscopicity of nano plastic plays an important role in their fate. Figure 1-1 shows the potential journey of micro- and nano-plastics travel in the air.

Overall, it is necessary to better understand the properties and impacts of nano-plastics in the atmosphere and their interactions with water. Water uptake ability of plastic materials are unknown. In this thesis work, we develop hygroscopicity models to describe their water uptake ability. Plastics are polymers, hence the hygroscopicity based on Flory-Huggins polymer thermodynamics theory is developed and applied. The role of molecular weight in the water uptake ability is also examined (Chapter 2). Flory-Huggins theory assumes that polymers are water-soluble but plastics can also be water-insoluble. Thus, the hygroscopicity based on an adsorption model is developed and applied to describe the droplet growth of hydrophobic polystyrene latex particles (Chapter 3). Nano-plastics as aerosols can be studied by the series of DMA and CPC. In Chapter 4, we cooperate with researchers at the National Institute of Standards and Technology (NIST) and quantify instrumentation error and the multiple charging correction of the DMA with respect to aerosol extinction measurement. In Chapter 5 we demonstrate that nano-plastics can be measured by a DMA and CPC, and demonstrate their size distribution. Lastly in Chapter 6, the hygroscopicity models developed in Chapter 2 and 3

are applied to nano-plastics and their water activity are measured.

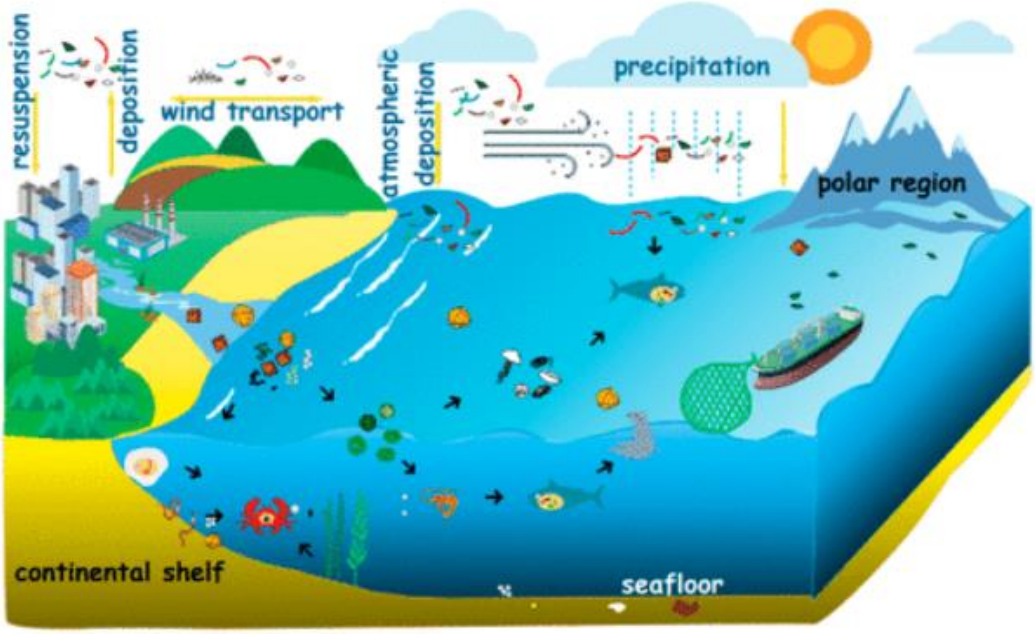

Figure 1-1: The potential journey of micro- and nano-plastics travel in the air. Picture credit: Liu et al. 2019

1.2 The Köhler theory and the single parameter hygroscopicity

Much of the work in this thesis measures and predicts droplet growth. A droplet is a small particle of any liquid. In this work, droplets refer to the water droplets if not specified. Droplets are in the size range of 1×10^{-6} m ~ 2×10^{-4} m in diameter. A typical cloud drop is 2×10^{-5} m in diameter (Eldridge 1957). Droplet growth occurs when water vapor in the air condenses onto small particles called CCN (Seinfeld, Pandis, and Noone 1998). This process is driven by

the transfer of energy from the surrounding air to the water vapor, which causes the water vapor to lose heat and change from a gas to a liquid. The thermodynamics of droplet growth was first described by Köhler theory (Köhler 1936).

Even under super-saturated condition, cloud droplets would not form without a seed, known as CCN. This is due to the curvature effect (Kelvin effect); the curve of the droplet reduces the surface tension comparing to a flat surface. However, with the existence of the cloud condensation nuclei (CCN), the solutes and solvent tend to form solution and increase the system entropy. Rain droplets can stably exist in the atmosphere. This is called the Raoult effect. Köhler theory considers both the Kelvin and Raoult effects and states that

$$S = a_w exp(\frac{A}{D}) \qquad (1.1)$$

where S is the saturation ratio. S is the same as relative humidity (RH) at sub-saturation region. $S = 0.8$ is 80% relative humidity in the environment. a_w is the water activity of the solution and D is the wet diameter of the droplet. A is a coefficient related to the droplet properties and equals

$$A = \frac{4M_w\sigma_w}{RT\rho_w} \qquad (1.2)$$

where M_w is the molecular weight of water (18.02 g mol^{-1}), R is the gas constant (8.314 J K^{-1} mol^{-1}), T is the temperature and ρ_w is the density of water (1000 kg m^{-3}). σ_w is the surface tension of the droplet which is assumed to be the same as pure water (0.072 J m^{-2}).

The traditional Köhler theory considers the water activity as the mole fraction of the water,

and assumes ideal mixing, which is

$$a_w = x_w \qquad (1.3)$$

Where x_w is the mole fraction of water.

Droplet growth depends on both the water and the nuclei solute property. Particle shape, size, and porosity are important physical properties that affect droplet growth (Dusek et al. 2006). The chemical properties of the nuclei are just as important and can be described by a representative single hygroscopicity parameter. Hygroscopicity is the particle intrinsic ability to uptake water. In 2007, Petters et al. developed a single parameter to represent the hygroscopicity of aerosol substances (M. D. Petters and Kreidenweis 2007). The definition of the hygroscopicity (κ) is:

$$\frac{1}{a_w} = 1 + \kappa \frac{V_s}{V_w} \qquad (1.4.1)$$

$$a_w = \frac{V_w}{V_w + \kappa V_s} \qquad (1.4.2)$$

Where V_s and V_w are the total volume of solute and water respectively. κ- Köhler theory is often written as (M. D. Petters and Kreidenweis 2007):

$$S = \frac{D^3 - {D_d}^3}{D^3 - {D_d}^3(1-\kappa)} exp(\frac{A}{D}) \quad (1.5)$$

Where D_d is the particle dry diameter. Equation (1.5) shows the relation between saturation ratio and particle hygroscopicity. Other particle properties that related to the saturation ratio (e.g. the aerosol light-scattering enhancement factor) are also related to and can be expressed by κ.

Based on the traditional Köhler theory, the theoretical hygroscopicity (or the intrinsic hygroscopicity) is as follows (R. C. Sullivan et al. 2009):

$$\kappa_{RK} = \frac{v_s M_w \rho_s}{M_s \rho_w} \qquad (1.6)$$

Where v_s is the Van't Hoff coefficient of the solute. M_w and M_s is the molecular weight of the water and the solute respectively, and ρ_w and ρ_s is the density of the water and solute. It was assumed that the intrinsic hygroscopicity agreed with experimentally determined hygroscopicity that depends on the measured critical dry diameter (D_c) and the saturation (S) (M. D. Petters and Kreidenweis 2007):

$$\kappa_{RK} = \frac{4A^3}{27{D_c}^3(ln\ S)^2} \quad (1.7)$$

Theoretical hygroscopicity can be directly calculated if the nuclei density and molecular weight are known. However, the experimental hygroscopicity requires particle size distribution measurements under a constant supersaturation environment.

At sub-saturation environment, the growth of the droplet can be represent by the hygroscopic growth factor (G_f) (Massling, Stock, and Wiedensohler 2005):

$$G_f = \frac{D}{D_d} \qquad (1.8)$$

Based on the Köhler theory, the hygroscopicity at sub-saturation environment (κ_{sub}) is related to the hygroscopic growth factor (T. V. Vu, Delgado-Saborit, and Harrison 2015):

$$\kappa_{sub} = ({G_f}^3 - 1)\left[\frac{1}{S}\exp\left(\frac{A}{D_d G_f}\right) - 1\right] \quad (1.9)$$

1.3 The experiment set-up of aerosol hygroscopicity study

One of the key challenges in understanding the impacts of aerosols is the difficulty in accurately measuring and modeling their behavior in the atmosphere. The Intergovernmental Panel on Climate Change (IPCC) report shows that aerosol-cloud and aerosol-radiation interactions still remain the largest source of uncertainty in climate prediction (IPCC 2021). This is due to the complex chemical composition of CCN that govern droplet formation and evolution. Modeling, field study and lab experiments all contribute to reducing this uncertainty and the understanding of aerosol science. In this thesis work, we focus on the lab scale study. Subsequently, we will introduce the instrumentation for particle size and number concentration measurement.

1.3.1 The differential mobility analyzer (DMA)

Understanding particle size is critical to determining aerosol environmental fate and effects. Electrical mobility particle size classifiers are often used to measure particles below 500 nm (Johnson et al. 2020). DMA is one of the most widely used electrical mobility classifying instruments (Johnson et al. 2020; Radney et al. 2013; Mason et al. 2012; Moore, Nenes, and Medina 2010). A DMA can quickly classify particle sizes down to 10 nm every second (Knutson and Whitby 1975; Winklmayr et al. 1991). DMA selects nanoparticles by their

electrical mobility diameter (D_m). DMA is a column with an iron rod inside. A neutralizer charges the aerosols before the particles pass through the DMA. A voltage difference is applied across the rod and the column. The charged particles are distributed across the column by the mobility. At the end of the column, there is a small slit to allow a small range of the electrical mobility particles to pass through. The electrical mobility (Z_p) is calculated from the geometry of the DMA (Knutson and Whitby 1975),

$$Z_p = \frac{Q_{sh}}{2\pi VL} \ln\left(\frac{r_2}{r_1}\right) \quad (1.7)$$

where Q_{sh}, V, L, r_2 and r_1 are sheath flow rate, voltage difference, length between exit slit and polydisperse aerosol inlet, and outer and inner radius of annular space respectively. The mobility diameters of the multiply charged particles can be calculated through the electrical mobility equation,

$$Z_p = \frac{qeC}{3\pi\mu D_{\mathrm{m}}} \quad (1.8)$$

where q, e, C, μ and D_m are the number of elementary charges on the particle, the elementary charge ($\approx 1.602 \times 10^{-19}$ C), the Cunningham slip correction factor, the gas viscosity and the mobility diameter, respectively.

The Cunningham slip correction equation is as follows (Li and Wang 2003):

$$C_{\mathrm{c}}(D) = 1 + \frac{2\lambda_{\mathrm{g}}}{D}\left[1.142 + 0.558e^{\left(-0.999D/2\lambda_{\mathrm{g}}\right)}\right] \quad (1.9)$$

where λ_g is the mean free path of the gas at the temperature (T) and pressure (P) of the measurement. For air at T = 298.15 K and P = 101.325 kPa: $\mu = 1.837 \times 10^{-5}$ kg m^{-1} s^{-1} and λ_g

= 67.9 nm.

However, the DMA measurement assumes each particle has the same positive charge. Thus understanding the distribution of charges in aerosol population is necessary to understand subsequent aerosol measurement. For example, doubly charged particles with diameter of 327 nm have the same electrical mobility as the 200 nm singly charged particles. The multiple charging error can be thus corrected by the charging theory.

The probability of charging is determined by the collision of the ions to the aerosols and charging theory (Fuchs 1963). For different types of neutralizers, different charging theories should be developed. In 2015, Tigges et al. proposed a set of parameters to calculate the probability for particles carrying $-2 \leqq q \leqq +2$ in a soft X-ray type neutralizer (Tigges et al. 2015). For particles carrying more than 3 charges, the Gunns model was suggested (Gunn 1955). From charging theory, the probability of aerosols carrying more than 3 charges was small (Gunn 1955; Tigges et al. 2015). In the model that Tigges proposed, the probability of a 150nm sphere particles that carries +3 charges in the soft x-ray neutralizer is only 0.6%. As a result, the number concentration of the triply or more charged particles is low. When considering the number of charges in the aerosol measurement, people usually include only singly and doubly charged particles in the calculation.

1.3.2 The condensation particle counter (CPC)

Particle number concentration are counted by CPC (Stolzenburg and McMurry 2007). In a butanol based CPC, nanoparticles are enlarged in a super-saturated butanol environment to be counted by the laser light. The principle of the CPC counting is very similar to an optical particle counter (OPC). An OPC is a device used to measure the size and concentration of particles suspended in a gas or liquid. It operates on the principle of laser scattering. A laser beam is directed through the sample, and the amount of light scattered by the particles is measured using a detector. The size of the particles can be determined based on the angle of scattering, and the concentration of the particles can be calculated based on the intensity of the scattered light.

Unlike the OPC, in a CPC the limit of particle counting can reach sizes down to 4 nm. Particles in nano-sizes come into a high supersaturated butanol environment and grow into large droplets that can be detected. The enlarged droplets then come into a laser viewing volume and scatter the light. A photodetector collects the light-pulses caused by droplets scattering. The light-pulse is then converted into electrical signals and the rate is counted to calculate the number concentration.

1.3.3 The cloud condensation nuclei counter (CCNC) and the scanning mobility CCNC analysis (SMCA)

The Droplet Measurement Technology cloud condensation nuclei counter (CCNC)

(Roberts and Nenes 2005) is a long tube with temperature controlled at the top, in the middle, and at the end of the tube. The wall of the tube is saturated by water. Since mass transfer is faster than heat transfer, a steady supersaturation environment will be established. The mono-dispersed particles come into the tube and grow or not depending on the controlled supersaturation, then come into an OPC to measure the number concentration.

The scanning mobility CCNC analysis (SMCA) method uses a particle size classifier, usually a DMA, a CPC and a CCNC (Moore, Nenes, and Medina 2010). Monodisperse particles that have been classified by the DMA would come into CPC and CCNC which are in parallel. The number concentration ratio of the all the particles counted (measured by CPC) and the particles that activated under a constant supersaturation (measured by CCNC) shows the particles cloud condensation activity. Ideally, for a small dry diameter particle, the number concentration ratio should be zero. There should be no particles count in the CCNC since the cloud condensation nuclei are not large enough. Once reaching a specific dry diameter, the cloud condensation nuclei are large enough and suddenly all the particles should activate. The number concentration ratio will be 1 and the specific dry diameter is referred to as the critical dry diameter. In reality, the shape of the CCN activation is sigmoidal instead of a step function. We hence define the critical dry diameter as the diameter where 50% of the particles grow into droplets. The dry diameter and supersaturation data applied with the Köhler theory are used to

find the hygroscopicity.

In the following chapters, a common measurement procedure is used to measure aerosol hygroscopicity in this thesis work, shown in Figure 1-2. For example, known compounds of the highest purity are purchased. The selected material is then put into ultra-purified water. A solution, or particle suspension in liquid water, is made, then passed through the atomizer and wet particles would be generated. Water is removed from the particle via evaporation when passed through the dryer. A DMA then classifies the particles by the electrical mobility, and the mono-dispersed particles are then separated into the CPC with a flow ratio of 0.3 L min^{-1} and a CCNC with a flow ratio of 0.5 L min^{-1} to count and compare the number concentration.

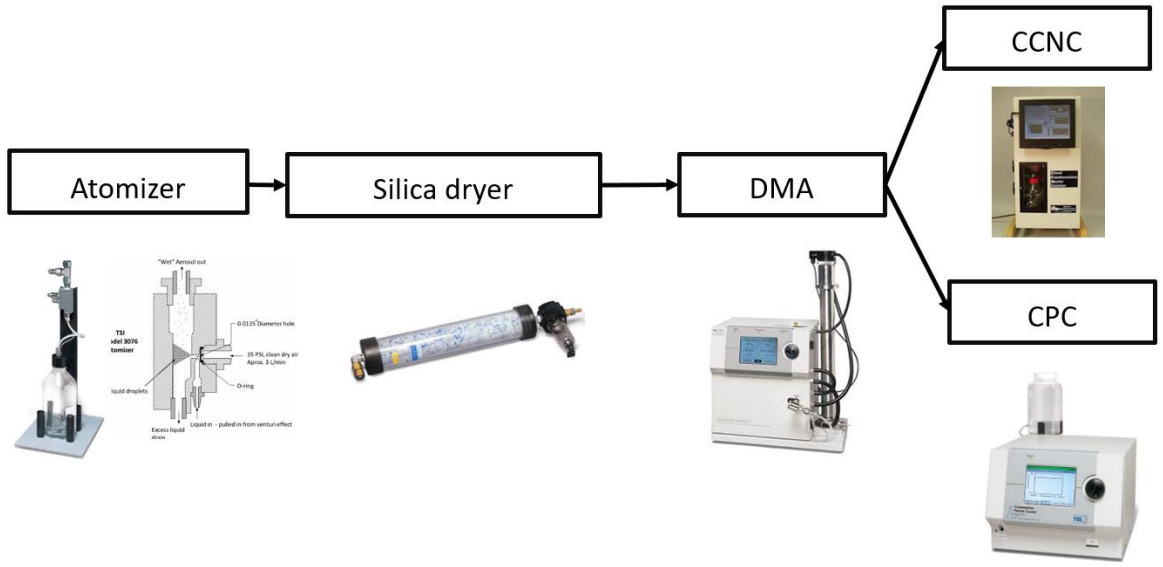

Figure 1-2: The experimental set-up for SMCA measurement.

1.4 Thesis Outline

The results of the doctoral thesis work contribute answers to the following scientific questions:

(1) How can we predict the droplet growth of polymer particles of known size and what is the adequate hygroscopicity model to describe their water-uptake?

(2) How do molecular-level surface modifications modify the hygroscopicity of polystyrene particles? Can current bulk-dissolution models be applied to the surface-modified particles?

(3) How do uncertainties in DMA measurement affect subsequent aerosol scattering and absorption estimates?

(4) Can traditional atmospheric aerosol instruments be used to measure plastic nanoparticles generated in solution?

(5) Why nano-plastics can travel to far and cold area? What is the hygroscopicity of nano-plastics and can we apply an adequate thermodynamic model?

To answer these questions, the following work is separated into five distinct chapters (Chapter 2 to Chapter 6). In each chapter, the background and motivation as it pertains to atmospheric aerosol or polymer nanoparticles will be discussed. The relevant measurement and

analytical theory will also be presented. In addition to current theory, we develop new parametrizations for water-uptake (Chapter 2 and 3), and propose new analysis to quantify sources of error in measurement (Chapter 4). Using the techniques developed in previous chapters, we investigate the size and number distribution of nano-plastics in the environment (Chapter 5) and their hygroscopicity (Chapter 6). The size distribution and hygroscopicity can help us understanding the lifetime and transport of nano-plastics, and can also be applied to the climate model to reduce uncertainties from indirect effect. Overall, the thesis work will contribute to our scientific understanding of aerosol metrology and polymer nanoparticles. Future work and the broader impact of this thesis work is outlined in Chapter 7.

Chapter 2: The Hygroscopicity of Water Soluble Polymer

Access published article at:

Chun-Ning Mao, Kotiba A. Malek & Akua Asa-Awuku **(2021)** Hygroscopicity and the water-polymer interaction parameter of nano-sized biodegradable hydrophilic substances, Aerosol Science and Technology, 55:10, 1115-1124, DOI: 10.1080/02786826.2021.1931012

2.1 Background

Organic aerosol is ubiquitous and regularly breathed in by the human body. Indeed, organic particles can contribute up to 30%-80% of the atmospheric aerosol mass burden (Q. Zhang et al. 2007) and can comprise of short dicarboxylic acids to long polymeric chains (Kalberer et al. 2004). Additionally, organic nanoparticles are intentionally produced and inhaled for aerosol therapy (Muralidharan et al. 2015; Gill et al. 2007; Agnihotri, Mallikarjuna, and Aminabhavi 2004; Malcolmson and Embleton 1998; Azarmi, Roa, and Löbenberg 2008). The health effects of inhaled particles depends on the deposition in the respiratory system; the final particle deposition is controlled by particle size (Gill et al. 2007; Malcolmson and Embleton 1998). These particles might not stay at nano-size but likely up-take water and grow to larger particles after exposure to high relative humidity in the respiratory system (Kim, Xi, and Si 2013; Shelly, Lloyd, and Park 1988). Larger particles have greater gravitational settling and impaction; thus affecting the drug delivery efficiency or potentially causing unwanted

health effects (Longest and Hindle 2012; T. V. Vu, Delgado-Saborit, and Harrison 2015; Longest, Tian, and Hindle 2011; Hindle and Longest 2010; Broday and Georgopoulos 2001). Longest and Hindle, 2012 proposed that nanoparticle enhanced condensational growth (ECG) could reduce the number of exhaled particles and increase the deposition efficiency of drug particles in respiratory tract. Longest and Hindle, 2012 used a non-hygroscopic drug, budesonide, and hygroscopic excipient mimics (sodium chloride, citric acid and mannitol) in the study. The ECG simulations showed that larger wet particles can be ~ 3 to 4 times greater than the initial dry particle diameter and the ability of modeled inhaled organic nanoparticles to swell was governed by aerosol size and hygroscopicity (Longest and Hindle 2012). Hence an improved understanding and measurement of aerosol water-uptake is needed to predict inhaled particle deposition.

Hygroscopicity is related to but different than solubility (R. C. Sullivan et al. 2009). It is an important property in aerosol science, applied to predict aerosol droplet formation (Man, Kreidenweis, and Chan 2008) and drug efficiencies in pharmaceutical science (Visalakshi et al. 2005; Anbarasan et al. 2018). Hygroscopicity can be measured with bulk and nano-scale measurements. However, the experimental methods to measure hygroscopicity differs vastly between nano- and macro- scales (Tang et al. 2019). Bulk (macro-scale) hygroscopicity measurements require significant amounts of substance (~milligrams) and are usually

measured by gravimetric sorption methods that weigh the mass difference before and after the water sorption (Anbarasan et al. 2018; Visalakshi et al. 2005; Weinmüller et al. 2006). Several aerosol, particularly nanoparticle, methods exist and have been recently reviewed (Tang et al. 2019). One of the most versatile methods to estimate hygroscopicity exposes particles to supersaturated water humidities using a CCNC [e.g., but not limited to CCN (M. D. Petters and Kreidenweis 2007; Dinar, Anttila, and Rudich 2008; Kumar, Nenes, and Sokolik 2009; D. Vu et al. 2019)]. Bulk and nano-scale methods produce different hygroscopicity estimates; the total surface area of nanoparticles can be larger than bulk substances and the water vapor liquid equilibrium occurs on significantly different time scales. Furthermore, as water vapor condenses on nanoparticle seeds, the concentration of solute at equilibrium could be much more dilute than the equilibrium concentration of a bulk scale experiment. Indeed, the mechanism of nanoparticle enhanced condensation growth in human respiratory system parallels that of nanoparticle hygroscopic growth in the atmosphere. Thus single-parameter hygroscopicity estimates proposed for atmospheric nanoparticles (M. D. Petters and Kreidenweis 2007) may be applied to predict the final droplet size of inhaled nanoparticles.

The hygroscopicity of water-soluble inorganic materials behaves ideally and the water activity of dilute droplets can be approximated with Raoult's law and Köhler theory (R. C. Sullivan et al. 2009; M. D. Petters and Kreidenweis 2007). Hence the derived thermodynamic hygroscopicity is simply the ratio of the molecular volume of the solute to water, multiplied

with the Van't Hoff disassociation coefficient (R. C. Sullivan et al. 2009). However, organic interactions with water can be non-ideal. The predicted hygroscopicity derived from Raoult-Köhler theory deviates from measurements as the molecular weight of the solute surpasses 300 g mol^{-1}. This is particularly true for large molecular weight organic polymers (Petters et al. 2009).

Polymer nanoparticles are common drug delivery materials (Azarmi, Roa, and Löbenberg 2008; Muralidharan et al. 2015) and are also formed in the atmosphere (Kalberer et al. 2004). Thus, there exists thermodynamic theory to account for the polymeric water-uptake of nanoparticles (Petters et al. 2006; Petters et al. 2009). To account for polymer nanoparticle behavior in a solvent, previous work by Petters et al. 2006 combined the water activity from Flory-Huggins theory with Köhler theory to predict the final wet droplet size of organic particles. Flory-Huggins theory (Flory 1942) assumes the interaction parameter is independent of organic volume fraction if the solvent readily dissolves the solute. Petters et al. 2006 applied the model of Wolf et al. (Wolf 2003) into Flory-Huggins- Köhler (FHK) theory, transforming the interaction parameter as a function of volume fraction and three additional fitted parameters. FHK theory (Petters et al. 2006) also assumes that the molar volume of the solute approaches infinity, the contribution of the molecular weight is negligible and the water polymer interaction defined by three fitted parameters dominates.

The water polymer interaction parameter has been previously measured with bulk

gravimetric sorption techniques (Weinmüller et al. 2006; Karimi et al. 2005). However as with hygroscopicity measurements, the equilibrium concentration and water polymer interactions derived from bulk measurements may be different at nano-scales. The equilibrium water uptake on a nanoparticle is large; the wet particle diameter can be 10 to 100 times greater than the dry particle diameter thus forming a dilute solution. Conversely, for macro-scale measurements water absorbs on the surface of the material. Visalakshi et al. 2005 measured the water uptake behavior of 0.1g of different antituberculosis drugs by a gravimetric method; the water content was sub-saturated and ranged from 2% to 55% at high relative humidity (~93%). For polymer like hydrogels, Weinmüller et al. 2006 used water vapor sorption method with hydrogel layer 1×10^{-6} to 3×10^{-6} m, and the sorption water activity ranged from 0.077 to 0.85. Again, Flory-Huggins theory assumes the interaction parameter is constant for very dilute solutions. Hence the Flory-Huggins theory assumption may be inadequate for bulk hygroscopic estimates but appropriate for hydrophilic substances at nano-scale.

Four common hydrophilic organic inhalable drug delivery materials are experimentally tested in this study with atmospheric CCN activation measurement and modelling techniques. Mannitol, lactose, gelatin and polyethylene glycol (PEG) have significantly different molecular weights (182, 342, 75000, and 100000 g mol^{-1}, respectively; see Table 2-1). The range in properties will be used to examine and derive physical meaning to the relationship of nanoparticle hygroscopicity and the water-interaction parameter. Furthermore, experimental

results will be compared to a combination of existing theory, explicit and empirical droplet models.

2.2 Experimental Methods

Dry nanoparticles particles were generated from atomized organic solutions. Specifically, 0.01g of mannitol (Sigma Aldrich, 99+), lactose (Sigma Aldrich, 99+), gelatin (Sigma Aldrich, 99+), and polyethylene glycol (PEG, Sigma Aldrich, 99+), were dissolved into 250 mL of ultra-purified water (Milipore® 18MΩ cm). Additional properties of these compounds are presented in Table 2-1. A Collison type atomizer then generated wet droplets from the solution to be subsequently heated to 100℃ and dried via a silicon dryer. The dry poly-disperse ultrafine aerosols are then sampled at 0.8 liter per minute with a scanning mobility particle sizer (SMPS). The SMPS consists of an Electrostatic Classifier, Differential Mobility Analyzer and Condensation Particle Counter. The DMA size selects the poly-dispersed dry aerosols by electrical mobility and produces mono-mobile aerosols. The mono-disperse aerosols were then split into the CPC and Cloud Condensation Nuclei Counter (Roberts and Nenes 2005) with the flowrate 0.5 liter per minute and with the flowrate 0.3 liter per minute to analyze the CCN activity. The total particle concentration (CN) is counted by the CPC and the concentration of particles that form droplets at a selected size and constant supersaturation (CCNN) is counted

by the CCNC. The ratio of the CCNN to CN is computed with Scanning Mobility CCN Analysis Method (SMCA) (Moore, Nenes, and Medina 2010) and a critical diameter (D_c) is computed. For a given constant supersaturation, s, and compound, the experiment is repeated four times. By measuring the CCNN/CN ratio at several different supersaturations, supersaturation and dry diameter (s-D_c) data is obtained. The supersaturation is then varied from 0.2% to 1.2%. s-D_c measurements are required to calculate nanoparticle hygroscopicity.

Table 2-1: Nanoparticle Properties of Compounds used in this study

Compound Name	**Formula**	**Classification**	**Molecular Weight** [kg mol^{-1}×10^{-3}]	**Molar Volume** [m^3 mol^{-1}]	**Density** [kg m^{-3}]	**Van't Hoff Factor**
Ammonium Sulfate	$(NH_4)_2SO_4$	Inorganic Salt	132.14	74.70	1769	2.5
Mannitol	$C_6H_{14}O_6$	Polyol	182.17	113.85	1600	1
Lactose	$C_{12}H_{22}O_{11}$	Disaccharide	342.3	222.27	1540	1
Gelatin	$C_{10}H_{15}O_{39}N_{31}$	Polymer	75000	55555.5	1350	1
Polyethylene Glycol (PEG)	$C_{2n}H_{4n+2}O_{n+1}$	Polymer	100000	89285.7	1120	1

2.3 Theory and Calculations

Droplet formation is a function of saturation ratio (*S*) and can be can be described with Köhler theory (Köhler 1936) as follows:

$$S = a_w exp(\frac{A}{D}) \qquad (2.1)$$

where a_w is the water activity of the solution and *D* is the wet diameter of the droplet. *A* is a coefficient related to the droplet properties and equals

$$A = \frac{4M_w\sigma_w}{RT\rho_w} \qquad (2.2)$$

where M_w is the molecular weight of water (18.02 g mol^{-1}), R is the gas constant (8.314 J K^{-1} mol^{-1}), T is the temperature and ρ_w is the density of water (1000 kg m^{-3}). σ_w is the surface tension of the droplet which is assumed to be the same as pure water (0.072 J m^{-2}). Although solute dissolves in the solution, the droplet is assumed to be dilute and have the properties of pure water.

For the simple Köhler theory (M. D. Petters and Kreidenweis 2007), a_w is approximated by Raoult's law and is equal to the molar fraction of water, x_w. Henceforth, we refer to this model as Raoult-Köhler (RK) theory (M. D. Petters et al. 2009). For organic polymers in RK theory, the Van't Hoff coefficient, v_s = 1 and the single-parameter hygroscopicity, κ is the ratio of the molecular volume of water and the molecular volume of solute. If saturation, *S,* and particle diameter, D_c are experimentally known, κ- hygroscopicity with RK assumptions is

determined from experimental data as follows (M. D. Petters and Kreidenweis 2007):

$$\kappa_{RK} = \frac{4A^3}{27{D_c}^3(ln\ S)^2} \qquad (2.3)$$

FHK theory expands RK to account for polymer behavior (Markus D. Petters et al. 2006) (*see* Appendix) such that:

$$S = (1-\varphi)\, exp[(1-F)\varphi + \chi\varphi^2]\, exp(\frac{A}{D}) \qquad (2.4)$$

where φ is the volume fraction of the polymer, F is the reciprocal of the chain segments of the polymer equal to the ratio of the molecular volume of water and the solute and χ is the Flory-Huggins interaction parameter. The interaction parameter, χ is related to the solubility of the solute and solvent. The droplet will separate into two phases if the interaction parameter is larger than 0.5. The solvent is considered a good solvent if the interaction parameter is smaller than 0.5. The interaction parameter for a given solute is often unknown and it is assumed constant. Furthermore, water is assumed to dissolve the solute and is thus assumed to be a good solvent in droplet studies. χ is obtained from the curve fittings of the (s-D_c) data. Equation (2.5) is combined with the single-parameter hygroscopicity, κ (M. D. Petters and Kreidenweis 2007) in Eq. 4, and the term for Flory-Huggins-Köhler hygroscopicity, κ_{FHK}, is as follows:

$$\kappa_{FHK} = \frac{1-\varphi}{\varphi}\left[-1 + \frac{1}{(1-\varphi)\, exp[(1-F)\varphi+\chi\varphi^2]}\right] \qquad (2.5)$$

Equation (2.5) accounts for entropic and enthalpic changes of polymers in droplet solutions. Specifically, the first term in the exponent [(1-F)φ] relates to the entropic disorder

of the molecules mixing and particle sizes that relate to the processes of mixing. The second term in the exponent [$\chi\varphi^2$] is the enthalpy term and molecular interactions are represented by the interaction parameter. The above equation can be simplified such that,

$$\kappa_{FHK-S} = -(\chi - 0.5)\varphi + F \quad (2.6)$$

Where κ_{FHK-S} is the simplified hygroscopicity from Equation (2.6). The thermodynamic interpretation is more explicit in the simplified equation; In Equation (2.7), the hygroscopicity is the ratio of the molecular volume of water and the solute, adjusted by the water affinity-the interaction parameter, and is a combination of the entropy and enthalpy terms. This shows that the hygroscopicity depends not only on the molar volume now but also the molecular interaction. Notice that the when χ equals to zero, the ideal solution formed and the hygroscopicity is purely entropic controlled by the polymer model. For the non-polymer chemical, this entropy model may not be applicable. With the χ as a degree of freedom, the deviation from an inaccurate model may be included into χ and cause χ to be highly negative. If the saturation increases for a given nano-polymer, there exists a critical polymer volume fraction, φ_c at the point of droplet activation. φ_c is determined from the derivative of saturation to volume fraction equal to zero:

$$\varphi_c = \left(-6\chi\frac{Dd}{A}\right)^{-3/5} \quad (2.7)$$

Thus, the simplified Flory-Huggins-Köhler hygroscopicity $\kappa_{FHK\text{-}s}$ can be predicted from experimental parameters as follows:

$$\kappa_{FHK-S} = -(\chi - 0.5)\left(-6\chi\frac{Dd}{A}\right)^{-3/5} + F \qquad (2.8)$$

If the nanoparticle solute has $F \rightarrow 0$ then the single-parameter κ-hygroscopicity will be proportional to ${D_d}^{-3/5}$. Thus, hygroscopicity decreases when the dry diameter increases. When the interaction parameter is 0.5, κ-hygroscopicity = F. In other words, for a polymer where $F \rightarrow 0$ the solute does not dissolve; $\kappa = 0$ and the particle is non-hygroscopic(R. C. Sullivan et al. 2009). For inhaled hydrophilic biodegradable nanoparticle systems, water is assumed a good solvent. Equation (2.8) will be compared to experimental data to test the new model.

2.4 Results and Discussion

Figure 2-1 shows the CCN activation data of $(NH_4)_2SO_4$ and four hydrophilic biodegradable nanoparticles exposed to ~1% supersaturation. Data of different supersaturation are in Appendix A.2. Notice that the range of CCNN/CN should be from 0 to 1, where zero means no activation, while 1 means that all particles are activated. Hence in Figure 2-1, all CCNN/CN ratio larger than 1 are considered as 1. The number concentration of particles at large sizes are At 50% CCNN/CN efficiency, the critical activation diameter, D_c is defined. At 1% *s* $(NH_4)_2SO_4$ activates at 25 nm. $(NH_4)_2SO_4$ is inorganic, readily disassociates and is more hygroscopic than mannitol (D_c = 46 nm), lactose (D_c = 50 nm), gelatin (D_c = 74 nm), and PEG

(D_c = 54 nm). A smaller D_c for a constant s indicates more hygroscopic material and thus the organic nanoparticles have larger D_c than $(NH_4)_2SO_4$. In RK theory, D_c is expected to increase as the molecular weight increases (M. D. Petters et al. 2009). However, for PEG (100,000 g mol^{-1}) the activation dry diameter is similar to lactose (360 g mol^{-1}) and RK theory prediction for hygroscopicity fails.

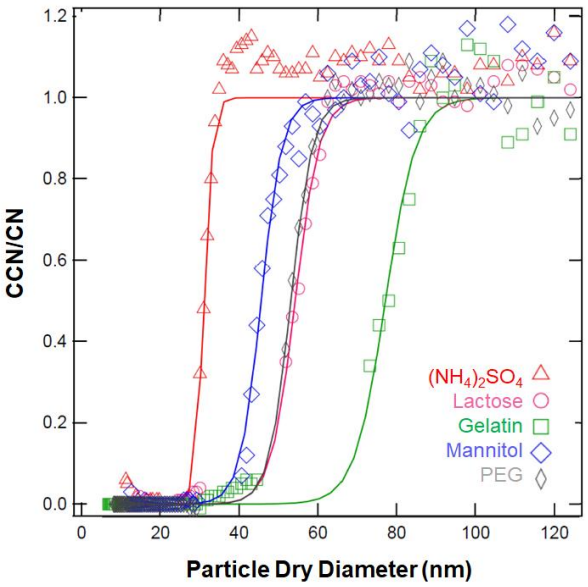

Figure 2-1: The droplet activation for ammonium sulfate (red triangles, 132 g mol^{-1}), mannitol (blue diamonds, 182 g mol^{-1}), lactose (pink circles, 342 g mol^{-1}), gelatin (green squares, 75000 g mol^{-1}), and PEG (grey rhombus, 100000 g mol^{-1}) at ~1% supersaturation. A sigmoidal fit (solid line) determines critical dry diameter, $D_{c,}$ at CCNN/CN=0.5.

The experiments are repeated over a range of s and the s-D_c data is shown in Figure 2-2. s-D_c is used to determine organic nanoparticle κ-values derived from RK theory and FHK

theory and the water-polymer interaction parameter, χ. Lower molecular weight compounds mannitol and lactose (< 500 g mol^{-1}) are shown in Figure 2-2a and higher molecular weight polymers (gelatin and PEG) are shown in Figure 2-2b. The hydrophilic organic compounds deviate from RK theory (M. D. Petters et al. 2009) (Figure 2-2). However, the RK prediction deviates more for larger molar volume molecules (Figure 2-2 and 2-3). FHK, assumes the nanoparticle behaves as a polymer and when χ =0, the FHK model is an improvement over RK theory for gelatin and PEG. FHK with χ =0 is similar to RK for lactose and mannitol and underpredicts the hygroscopicity of non-polymers. The FHK model is improved by decreasing χ. A smaller χ implies that a smaller supersaturation with the same dry diameter is required for droplet formation and therefore greater water up-take will occur for the same amount of solute. The best fit χ for mannitol and lactose (-12 and -8.3, respectively) agree well with the non-exponential response of the s-D_c data (Figure 2-2a.).

The polymer interaction parameter for PEG and gelatin range from 0.42~0.46 in the previous study (Dormidontova 2002; Borchard, Bremer, and Keese 1980). In our study, we obtain the polymer water interaction parameter from fitting and get a number way more negative (-2.6 for PEG and -0.42 for gelatin) than the previous study. Previous studies obtained the polymer-water interaction parameter from the density differences of the melting temperature differences by changing the concentration of polymer in water. Our study acquired χ from polymer nanoparticles in supersaturated environment. In order to simplified the model,

we do not consider the curvature effect. The surface tension of the droplet is assumed to be the same as pure water at 25℃ due to dilute solution assumption. However, both PEG and gelatin decreases the surface tension. The negative χ for both PEG and gelatin shows that the curvature effect may be non-negligible. However, polymer behavior at nano-scale may be different from bulk scale. This is found in surface property (Hahm 2014), mechanical property (Crosby and Lee 2007) and glass transition temperature (Napolitano and Wübbenhorst 2011) studies. It is possible that χ would become smaller at nano-scale comparing to the bulk phase study. Either the negative χ comes from neglecting the surface tension contribution or the nature of the nano-sizes, more studies need to be done to understand the polymer water interaction derived from CCN activation.

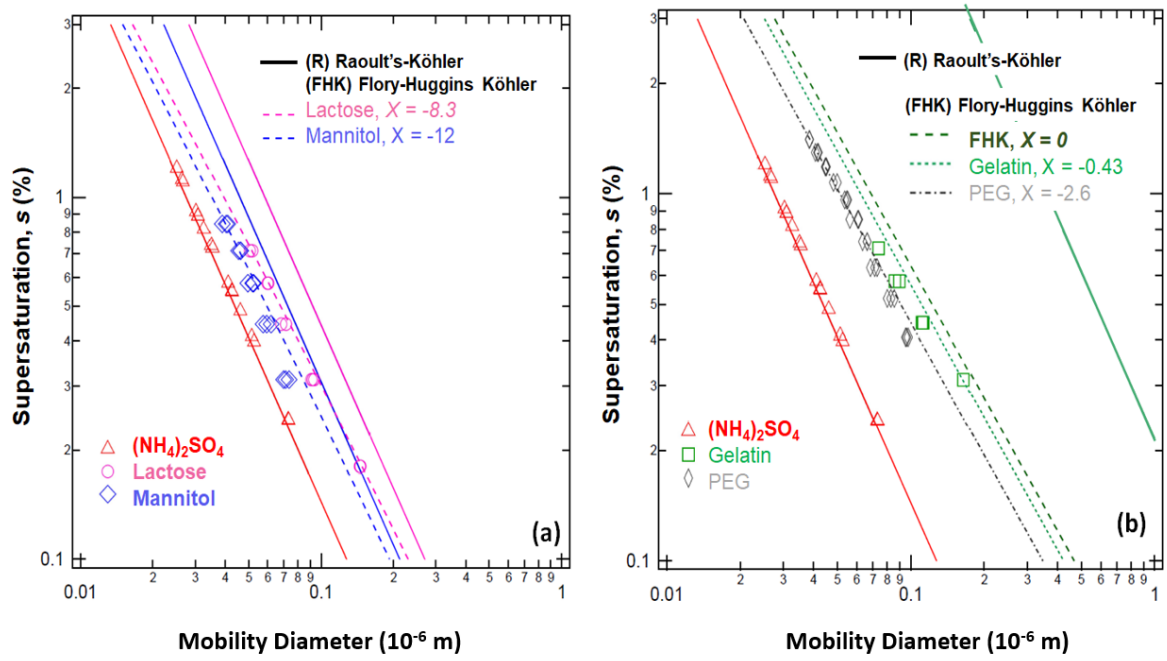

Figure 2-2: The relationship between supersaturation and nanoparticle dry diameter activation and droplet growth. (s-D_c) data for ammonium sulfate (red triangles) and RK theory (solid lines) are shown for reference. Dashed lines apply FHK theory with $\chi = 0$ and best fit single water-activity interaction parameter, χ. (a) Shows data and theoretical fits for gel-like low molecular weight non-polymers, mannitol and lactose. (b) Shows data and theoretical fits for polymers PEG and gelatin. Raöult-Köhler (RK) theory predicts a smaller activation dry diameter with a smaller molecular weight. The RK line for PEG is beyond the range of the figure. RK theory fails (not shown) for PEG with a molecular weight of 100,000 g mol^{-1}. Super saturation is $s = (S - 1)$.

Figure 2-3 compares the calculated hygroscopicity (κ_{RK} or κ_{FHK}) as a function of the

solute molar volume. Each solutes D_c is used to estimate the κ_{RK} and κ_{FHK} at supersaturation = 1%. The experimentally determined κ_{RK} and κ_{FHK} values for non-polymer are similar (< 0.05 deviation) and within experimental uncertainty of mannitol and lactose data points. κ_{RK} and κ_{FHK} can be calculated from theoretical known values and compared to the calculated values from experimental data. κ_{RK} derived from experimental data do not fall on the theoretical κ_{RK} line (Figure 2-3). RK theory assumes the ideal dilute droplet solution has a water activity equal to mole fraction of water and thus an increase in solute molar volume results in an exponential decrease in hygroscopicity. The dashed lines represent the Flory-Huggins Köhler theory under a constant dry diameter and best fit interaction parameter. For small molar volumes (< 100 mol cm^{-3}), the FHK and RK converge with hygroscopicity in range of 0.3 to 0.4. However, as the molar volume increases, κ_{FHK} plateaus, and deviates from theoretical RK behavior. Hence, κ_{FHK} depends on both the dry diameter and the interaction parameter when the molar volume is large.

It is noted that the interaction parameter is an experimentally determined parameter and additional parameters are likely the reason why the predicted FHK hygroscopicity fits much better than the RK hygroscopicity. This is also why the Wolf model, with three additional fitting parameters for the interaction parameter is avoided. Instead, the interaction parameter is considered a constant in this work. To reduce the fitting parameters and make physical meaning between the parameters more explicit, we consider the interaction parameter as a constant independent to the volume fraction and compare the simplified model ($\kappa_{FHK\text{-}s}$) to κ_{FHK}.

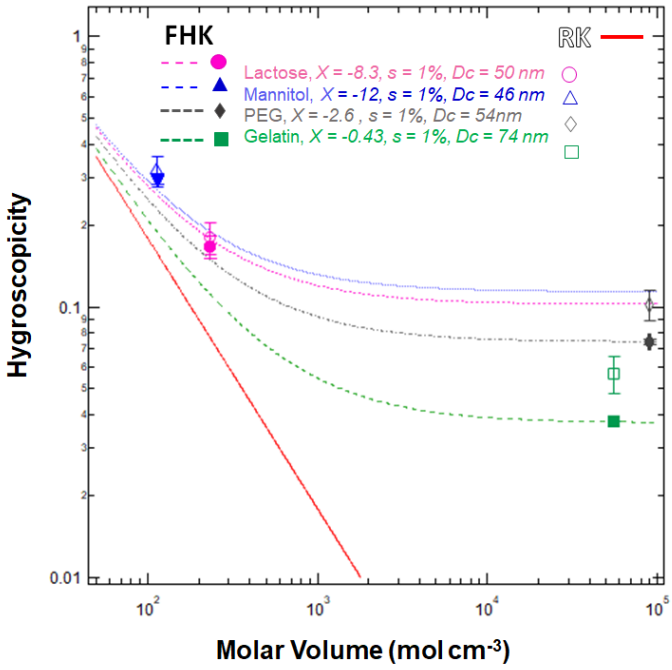

Figure 2-3: Nanoparticle hygroscopicity as a function of molar volume. Data points are the critical activation diameters, D_c at s = 1% for lactose (pink circles), mannitol (blue triangles), PEG (grey rhombus) and Gelatin (green squares). The solid line is the RK prediction while the dashed lines are the FHK prediction for the measured D_c and best fit interaction parameter, χ. In FHK, hygroscopicity is a function of both the dry diameter and the interaction parameter (Equation 2.6). The dry diameter can be measured and the interaction parameter is determined from Figure 2-2.

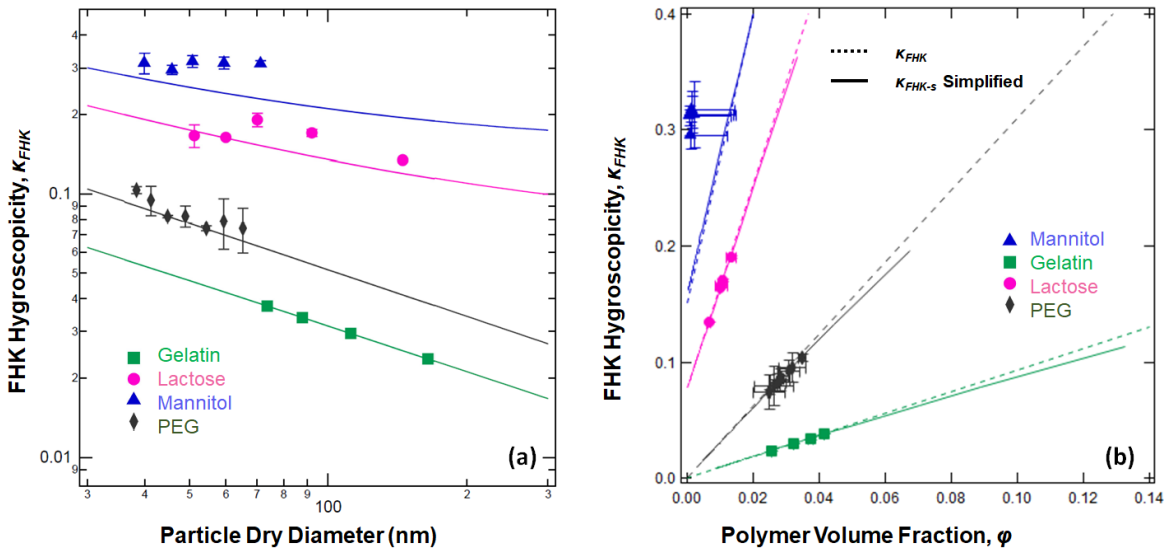

Figure 2-4: (a) Relationship between hygroscopicity and dry diameter. The hygroscopicity decreases with increasing dry diameters in both theory and experiment except for mannitol. (b) Comparison of κ-hygroscopicity FHK to simplified FHK theory. The dashed lines are the simplified Equation (2.7) while the solid lines are the theoretical FHK prediction using Equation (2.6).

For solutes such as lactose, gelatin and PEG, the FHK hygroscopicity decreases with the dry diameter (Figure 2-4a). The hygroscopicity for mannitol is almost a constant and does not decrease with the dry diameter and deviates from the prediction. Lactose, gelatin and PEG are larger compounds; the molecular weight and molar volume of mannitol is less than 200g mol^{-1} and 200×10^{-6} mol m^{-3}, respectively. Although the hygroscopicity is related to the dry diameter, for and non-polymer chemicals, the predicted hygroscopicity was underestimated, which means the entropy model for polymer is not applicable anymore. FHK hygroscopicity

should not be used to calculate the dry diameter for non-polymer, especially by Equation (2.8).

Figure 2-4b shows that the simplified FHK model ($\kappa_{FHK\text{-}s}$ and Equation (2.7)) works well for both experiment data and in theory. Equation (2.7) predicts nanoparticle hygroscopicity if the volume fraction is known. For a small polymer (<0.1 and as is the case for nanoparticle water droplet formation), the simplified $\kappa_{FHK\text{-}s}$ agrees well with FHK prediction. Furthermore, the simplified model works just as well as FHK for gelatin, lactose and PEG. Both models do not agree with mannitol experimental data. Mannitol has a constant hygroscopicity and constant volume fraction that is not related to the dry diameter

2.5 Summary and Future Work

Hygroscopicity is an important factor and estimates of particle hygroscopicity must also be determined at nano-scales. In this work, we showed the relationship between the hygroscopicity and the water-polymer interaction parameter for four common nanoparticle compounds employed in aerosol therapeutics. The final wet particle size of inhaled and exhaled particles can be predicted by estimated and actual hygroscopicity values. Thus, it is critical to measure and also define accurate models to describe the water up-take of hydrophilic, biodegradable polymers frequently used as drug delivery materials to define aerosol therapy efficiency.

The supersaturated CCN measurement technique can measure they hygroscopicity of mannitol, lactose, gelatin and PEG particles. For all four compounds, traditional Raoult-Köhler theory poorly predicts the behavior of the organic compounds. Flory-Huggins Köhler theory with a constant interaction parameter can improve predictions of droplet formation. Indeed, the addition of another parameter is necessary and the interaction parameter dominates the behavior of the hygroscopicity. The FHK model is less applicable for non-polymeric organics but can be applied to non-polymers with high molecular weights and molar volumes.

We studied the robustness of the FHK water uptake model for biodegradable nano particles and derived a simplified equation to be used if the RH and dry particle diameter is known. The application of the FHK model to hygroscopicity shows that for polymer material, entropy, the tendency of molecules mixing, the enthalpy and the interaction of the molecules must be considered. Under the good solvent assumption, the volume fraction is small and the hygroscopicity can be simply described as a function of dry diameter and interaction parameter. Our results show that for mannitol, a compound with molecular weight under 200 g mol^{-1}, the hygroscopicity is constant and does not depend on the dry diameter. An independence of hygroscopicity with dry diameter suggest that entropic mixing is not important. Hence, the final size of the nanoparticles inhaled can be predicted through hygroscopicity if the dry diameter of the particles were known.

Chapter 3: The Hygroscopicity of Water Insoluble Polymer

Access published article at:

Mao, Chun-Ning, Kanishk Gohil, and Akua A. Asa-Awuku. 2022. "A Single-Parameter Hygroscopicity Model for Functionalized Insoluble Aerosol Surfaces." *Atmospheric Chemistry and Physics* 22 (19): 13219–28. https://doi.org/10.5194/ACP-22-13219-2022.

3.1 Background

Heterogeneous water-vapor condensation occurs for both soluble (Rose et al. 2008) and insoluble (Kumar, Nenes, and Sokolik 2009; Koehler et al. 2009; Dalirian et al. 2018) particles. Traditionally, the cloud condensation nuclei (CCN) activation behavior is described by Köhler theory (Köhler 1936). In traditional Köhler (TK) theory, the droplet is assumed to be dilute, and the water activity follows Raoult's law; such that the water activity equals the water mole fraction, and the dilute droplet water activity coefficient is assumed to be unity. For water-soluble particles like inorganic ammonium sulfate (Rose et al. 2008) and sucrose (Dawson et al. 2020; Gohil and Asa-Awuku 2022), TK can predict their water uptake behavior. However, TK does not work so well for atmospherically relevant and abundant particles that are partially water soluble or water insoluble, less than a concentration of 5×10^{-4} (L/L) (Kumar, Nenes, and

Sokolik 2009; Tang, Cziczo, and Grassian 2016; M. D. Petters and Kreidenweis 2008). Thus, alternative droplet growth models for the partial and insoluble particles are needed.

Flory-Huggins Köhler (FHK)(M. D. Petters et al. 2009) is one example of a droplet growth model specifically applied to the water soluble polymers. FHK has been shown to work well for long-chained polymers such as gelatin, polyethylene glycol and polylactic acid (Markus D. Petters et al. 2006; M. D. Petters et al. 2009; C. N. Mao, Malek, and Asa-Awuku 2021). It uses a one fitting parameter that describes solvation and most recently was incorporated into a single-parameter hygroscopicity term that describes the water-uptake of water-soluble aerosol (C. N. Mao, Malek, and Asa-Awuku 2021).

The droplet formation of water-insoluble particles has been previously described with adsorption activation models (Lintis et al. 2021; Tang, Cziczo, and Grassian 2016; Kumar, Nenes, and Sokolik 2009; Hatch et al. 2012; Navea et al. 2017; Pajunoja et al. 2015; Malek et al. 2022). Brunauer, Emmett, and Teller adsorption isotherm models are typically applied for multilayer adsorption analysis of water uptake on clays (Hatch et al. 2012) and fly ash (Navea et al. 2017). Lintis et al., 2021 applied the Dubinin-Serpinsky model for soot and concluded that nucleation occurred at oxidized and hydrophilic surface sites on the soot. Pajunoja et al. measured the TK hygroscopicity for SOA and demonstrated that the droplet growth of organic compounds with low O:C ratio was an adsorption-dominated process for both sub – and super-saturated water vapor conditions. Kumar et al. 2009 showed that the droplet activation of

mineral dust could be described well using the Frenkel-Halsey-Hill adsorption theory (FHH-AT).

FHH-AT determines droplet growth with the help of 2 empirical parameters defined as A_{FHH} and B_{FHH} (Sorjamaa and Laaksonen 2007b). The parameter A_{FHH} is related to the interaction of the first layer of water and the particle surface, while the B_{FHH} represents the interaction between other layers of water molecules and the particles. Furthermore, it is postulated that A_{FHH} should range from 0.1 to 3.0, and B_{FHH} should be within range of 0.5 to 3.0 for mineral dust aerosols (Kumar et al., 2009). However, the reported and applied A_{FHH} and $B_{FHH,}$ parameters have varied significantly in literature. For example, Karydis et al. 2017 used the FHH-AT model to simulate the aerosol indirect effect of insoluble mineral dust CCN with an A_{FHH} and B_{FHH} of 2.25±0.75, and 1.20±0.10 respectively. Furthermore, Karydis et al., 2017 concluded that the global CCN number would decrease 10% for mineral dust with the use of those values. Hatch et al., 2014 measured montmorillonite dust and found that the A_{FHH} and B_{FHH} was 98 ± 22 and 1.79 ± 0.11 and the A_{FHH} and B_{FHH} was 75 ± 17 and 1.77 ± 0.11 for illite, respectively. Particles of intermediate polarity and high porosity may lead to a higher CCN activity (Koehler et al., 2009) and Hatch et al., 2012 attributed the high value of A_{FHH} to the surface chemistry and the porosity of the clays.

Specifically, porosity leads to a higher perceived hygroscopicity because water molecules fill the microporous structure. Thus, it should be noted that in the aforementioned

studies, the porosity of insoluble particles complicates the study of aerosol water-uptake and influences the role of aerosol chemistry that impacts the CCN activity. Moreover, the use of two parameters adds an additional degree of freedom that makes the direct comparison of different chemical species challenging; there may be multiple pairs A_{FHH} and B_{FHH} solutions for a single compound with or without porous structure. As a result, direct experimental measurement of the hygroscopicity of non-porous and spherical nuclei is important to understand the adsorption water uptake ability of atmospheric aerosol.

To better understand the activation behavior of insoluble particles, we study the CCN activity of spherical, non-porous polystyrene latex (PSL) particles using the Cloud Condensational Nuclei Counter (CCNC) (Roberts and Nenes 2005). PSL is a common material used for instrumentation calibration and model examination for aerosol optical properties. (S. Singh et al. 2014; Miles et al. 2011; Pettersson et al. 2004). They are spherical, uniform in size, and do not dissolve in water. The surfaces of PSL particles are hydrophobic, but can be manufactured to have a high density of hydrophilic sites (Ottewill and Vincent 1972). Different functional groups like carboxyl (-COOH) or amine ($-NH_2$) groups can be added to the PSL surface to create hydrophilic adsorption sites. Previous studies have shown that surface chemistry of the insoluble particles affect ice nucleation (Cziczo et al. 2009; R. C. Sullivan et al. 2010; Reitz et al. 2011; Koehler et al. 2009). But little is known about the influence of surface chemistry for liquid cloud droplet activation.

To our knowledge, few studies have explored the effects of molecular level particle surface changes for CCN and droplet formation. Mainly, water-soluble aerosol that contribute solute to the solution and modify droplet properties has been of great interest. Any changes at the surface of soluble aerosol are often overshadowed by the effects of solute dissolution if the solute is water-soluble. Additionally, to understand impacts of functionalized surfaces, the surface area or particle size of an aerosol must be well known. Given these constraints, spherical PSL aerosol with and without a functionalized surface provides an opportunity to advance the contributions of molecular surfaces to the discussion of water-uptake.

In the following sections, we examine the impact of surface chemistry to the CCN activity in both the Traditional Köhler (TK), Flory-Huggins Köhler (FHK) and the FHH-AT model. The first two models are generally applied to water-soluble compounds while the FHH-AT model is for water-insoluble particles. Furthermore, FHK is specifically designed for high-molecular weight polymers like PSL and therefore briefly considered. The following work also compares measurements to three hygroscopicity prediction models. Two single parameter hygroscopicity representations have been previously derived using TK (M. D. Petters and Kreidenweis 2007) and FHK (C. N. Mao, Malek, and Asa-Awuku 2021) assumptions. Additionally, we derive a third theoretical hygroscopicity parameter using the FHH-AT model and analyze the role of surface chemistry in the adsorption based hygroscopicity. Thus, the following data and analysis provide insight into the water-uptake of water-insoluble particles

and the impact of surface modified functional groups for the perceived aerosol hygroscopicity and droplet formation.

3.2 Experimental Methods

3.2.1 Polystyrene Latex (PSL) Composition and Size

Four different particle sizes, ~100 nm, 200 nm, 300 nm and 500 nm and three different PSL particles (plain, surface modified with amine functional group, $-NH_2$, and carboxyl functional group, -COOH) were purchased (Lab 261®). The sizes provided by the manufacturer are determined with dynamic light scattering (DLS) techniques. In this study, we verify the size and report the electrical mobility measured particle size (D_d) of the PSL particles with a Differential Mobility Analyzer, DMA and CPC operated in size scanning mode (Wang and Flagan 1990). The measured geometric mean size was within ~10% difference of the manufacturer's reported particle sizes (Table 3-1).

The PSL solution from Lab 261® contains Tween 20 as surfactant to prevent coagulation. The sizes of the surfactant particles are much smaller than the PSL particles, forming peaks at 20~100nm. Most of the surfactants particles would be excluded from the measurement if we only size selected the large PSL particles. The raw data (Appendix A.3) shows only one sigmoid curve, indicating a singular composition at the selected particle size.

Moreover, the hygroscopicity of surfactant particles, typically a hydrophilic polymer, will be much larger than an insoluble polymer like PSL. The measured TK hygroscopicity of the Tween 20 is around 0.28±0.05, while the measured TK hygroscopicity of the PSL particles are around 0.02~0.002. (see Figure 3-2) As a result, we believed that the influence of the surfactant is negligible in the measurements.

3.2.2 Aerosol Generation

0.4 mL of the PSL particle solution was diluted in 50 mL ultra-purified water (Millipore®, with conductivity < 18.8 MΩ cm). Wet particles were then generated with a constant output atomizer. Wet droplets were then passed through two silica gel diffusion dryers and the relative humidity was 5% after passing through the dryers. Poly-disperse particles are charged and sampled by an electrostatic size classifier, specifically a DMA. The DMA was set to select the size of the PSL particles. The PSL particles are then passed through a CPC with a flow rate of 0.3 L min^{-1} and a CCNC. The particle number concentration counted by the CPC is the condensation number concentration (CN) and is measured at rate of 1 Hz. The sheath and sample flow ratio are 10:1 in both the CPC and CCNC.

3.2.3 The Critical Supersaturation of PSL

The CCN activity for the selected particle size was measured with a continuous flow

stream-wise thermal gradient Cloud Condensation Nuclei Counter (DMT CCN100) (Roberts and Nenes 2005). A brief introduction is provided here and readers are directed to the (Roberts and Nenes 2005) for a more detailed discussion of the instrument. The CCNC is a column with a wet inner surface. Three thermal electrical controllers modify temperatures on the top, in the middle, and at the bottom of the CCNC column to establish a constant temperature gradient. A supersaturation is generated at the center of the column as air moves from the top to the bottom (Hoppel, Twomey, and Wojciechowski 1979). The sampled particles in the CCNC column provide surface for the occurrence of the heterogeneous condensation. An optical particle counter (OPC) at the bottom of the column, counts the particles that form droplets greater than 0.75 μm and provides the cloud condensation number concentration (CCN) every 1 Hz. Instrument supersaturations were achieved by modifying both inlet flowrate and the temperature gradient in the CCNC. Each supersaturation was calibrated using ammonium sulfate and Scanning Mobility CCN Analysis (SMCA) (Moore, Nenes, and Medina 2010).

CCN activity is the ratio of number droplets to total aerosol (CCNN/CN) measured at a given supersaturation and constant particle size (D_d). For each supersaturation, temperatures and flows are held constant for 10 minutes and CCN and CN data are measured every second. The CCN and CN concentration is then averaged in the 8th minute. The CCN activation for each sample is reported from 0.1 to 1.4% supersaturation. Critical supersaturation (s_c) for a given particle size (D_d) is defined at 50% efficiency growth of the CCN (i.e., CCNN/CN=0.5).

A smaller s_c for a constant D_d indicates that the particles are more hygroscopic. The s_c for all twelve PSL are listed in Table 3-1. The activation curves for all twelve PSL samples are provided in Supplemental Materials (Figure S-1). The measured s_c and D_d values are used to compute and compare subsequent particle CCN activation and hygroscopicity.

3.3 Theory and Calculations

The saturation ratio at the droplet surface can be generally described as follows.

$$S = a_w \exp\left(\frac{A}{D}\right) \quad \text{; and } A = \frac{4M_w\sigma_w}{RT\rho_w} \quad , \qquad (3.1)$$

where S is the saturation ratio; a_w is the water activity of the solution and D is the wet diameter of the droplet. The exponential term is known as the Kelvin term and describes the homogeneous nucleation of the droplet solvent. Thus, A is generally constant and is a function of the universal gas constant (R), the pure water droplet surface tension (σ_w), temperature (T), density (ρ_w) and molecular weight (M_w). Heterogeneous nucleation is considered in the water activity term. As aforementioned, for water-soluble inorganic salts and organics, (e.g., ammonium sulfate and sucrose) the water activity is approximated with Raoult's law and the water mole fraction, x_w.

Petters and Kreidenweis, 2007 employed Raoult's law to develop a single hygroscopicity parameter representation, κ, as follows,

$$\frac{1}{a_w} = 1 + \kappa \frac{v_s}{v_w}, \qquad (3.2)$$

Where v_s is the total volume of the dry particle and v_w is the total volume of the water in a droplet. The κ in Equation (3.2) is defined as the intrinsic hygroscopicity parameter of the compound, denoted by κ_{int}. If one assumes a dilute droplet, such that $a_w = 1$, κ_{int} can be solved from known solute and solvent properties such that $\kappa_{int} = v_s \frac{M_w \rho_s}{M_s \rho_w}$ (R. C. Sullivan et al. 2009). Where M_w is the molecular weight of water; M_s is the molecular weight of the dry particle; ρ_w is the density of water; ρ_s is the density of the dry particle; v_s is the Van't Hoff coefficient and is assumed to be one. If PSL is a polymer with ~100,000 g mol^{-1} molecular weight and a density of 1.06 g cm^{-3}, $\kappa_{int} \sim$ 0.0002, is a small number and approaches zero. One can also derive a hygroscopicity parameter based on TK, κ_{TK}, directly from measured experimental s_c and D_d data (M. D. Petters and Kreidenweis 2007)

$$\kappa_{TK} = \frac{4A^3}{27 D_d^3 ln^2 s_c}, \qquad (3.3)$$

$\kappa_{int} = \kappa_{TK} = 0.604$ for ammonium sulfate (Rose et al. 2008). The intrinsic and experimentally derived values also agree well for water-soluble compounds and partially soluble organics (Dawson et al. 2020; Peng et al. 2022; 2021).

Traditional Köhler theory calculations from theory and measurement tend to disagree for high molecular weight organics, such as polymers (Markus D. Petters et al. 2006; M. D. Petters et al. 2009). To calculate the water activity of high molecular weight compounds, Petters et al., 2006, 2009 combined the water activity of Flory-Huggins (Flory 1942) with the Köhler

theory for polymeric aerosols. Mao et al., 2021 derived a single parameter based hygroscopicity representation, κ_{FHK} as follows,

$$\kappa_{FHK} = \frac{1-\varphi}{\varphi}\left[-1 + \frac{1}{(1-\varphi)\,exp[(1-F)\varphi+\chi\varphi^2]}\right], \quad (3.4)$$

where φ is the volume fraction of the polymer. F is the reciprocal of the chain segments of the polymer equal to the ratio of the molecular volume of water and the solute and χ is the Flory-Huggins interaction parameter. Measured particle diameter, D_d, and s_c data are used to define empirical fits of χ and subsequently determine, κ_{FHK}.

Insoluble aerosol droplet activation is best described by an adsorption thermodynamic droplet growth model (Kumar, Nenes, and Sokolik 2009). Sorjamaa and Laaksonen, 2007a suggested the Frenkel-Halsey-Hill adsorption theory (FHH-AT) to define the a_w using the isotherm as follows,

$$a_w = \exp(-A_{FHH}\theta^{-B_{FHH}}) \quad \text{and} \quad \theta = \frac{D-D_d}{2D_w}, \qquad (3.5)$$

where θ is the surface coverage, and describes the layers of water molecules adsorbed on to the dry particle surface (Sorjamaa and Laaksonen 2007a). D_w is the diameter of a single water molecule and equals to 0.275 nm. A_{FHH} and B_{FHH} are compound specific empirical parameters. The FHH-AT parameters can be estimated by fitting the FHH-AT with s_c and D_d CCN measurement data (Kumar, Nenes, and Sokolik 2009; Herich et al. 2009).

To date, a single parameter hygroscopicity representation based on adsorption droplet growth does not exist in the current literature. In this work, we derive an experimental and

theoretical adsorption hygroscopicity, $\kappa_{FHH,exp}$ and $\kappa_{FHH,the}$ respectively. If the critical wet droplet diameter, $D_{p,c}$, is known, $\kappa_{FHH,exp}$, can then be expressed as a function of D_d and $D_{p,c}$ as follows

$$\kappa_{FHH,exp} = f\left(D_d, D_{p,c}\right) = \frac{6\theta D_w}{D_d}\left(\frac{1}{\exp\left(-A_{FHH}\theta^{-B_{FHH}}\right)} - 1\right), \quad (3.6)$$

Theoretically, droplet activation occurs when the derivative of the Köhler curve equals to zero $\left(\frac{dS}{dD_{p,c}} = 0\right)$. Hence the relation between critical surface coverage and the dry particle size is constrained with the following equation,

$$1 - \frac{2\theta_c D_w}{D_d} = \left(\frac{2AD_w}{A_{FHH}B_{FHH}D_d^2}\right)^{1/2} \theta_c^{\frac{B_{FHH}+1}{2}}, \quad (3.7)$$

The critical surface coverage, θ_c, is defined at the point where droplet activation occurs, and is obtained by solving Equation (3.7). As a result, the theoretical hygroscopicity of FHH-AT is derived,

$$\kappa_{FHH,the} = f(D_d) = \frac{6D_w}{D_d} A_{FHH}\theta_c^{-B_{FHH}+1}, \quad (3.8)$$

3.4 Results and Discussion

3.4.1 The CCN activity for different types of PSL.

Table 3-1 shows the mobility diameter of PSL and their corresponding critical supersaturation. Particle size matters most for water-uptake and thus larger particles (~500 nm) exposed to a constant supersaturation activate earlier than smaller aerosol (~100 nm) (Dusek

et al. 2006). For example, PSL-NH_2 particles with 85 nm diameters activate at 1.42% supersaturation while particles with 375 nm activate at 0.33% supersaturation. PSL-COOH and the plain PSL show a similar trend as well. The data suggests that PSL particles are wettable and hygroscopic, more so than particles with κ = 0. The parameters in Table 3-1 are used to predict CCN activation (s_c-D_d pairs) in Figure 3-1(a) and (b). The red dashed line in Figure 3-1 shows the traditional Köhler prediction for ammonium sulfate ($\kappa_{int} = 0.604$) for comparison purposes. All PSL particles are much less hygroscopic than ammonium sulfate ($\kappa_{int} = 0.604$) with larger hygroscopicity than theoretical values derived from known solute properties ($\kappa_{int} = 0.0002$). Traditional Köhler theory significantly underpredicts particle activation and droplet growth of PSL particles.

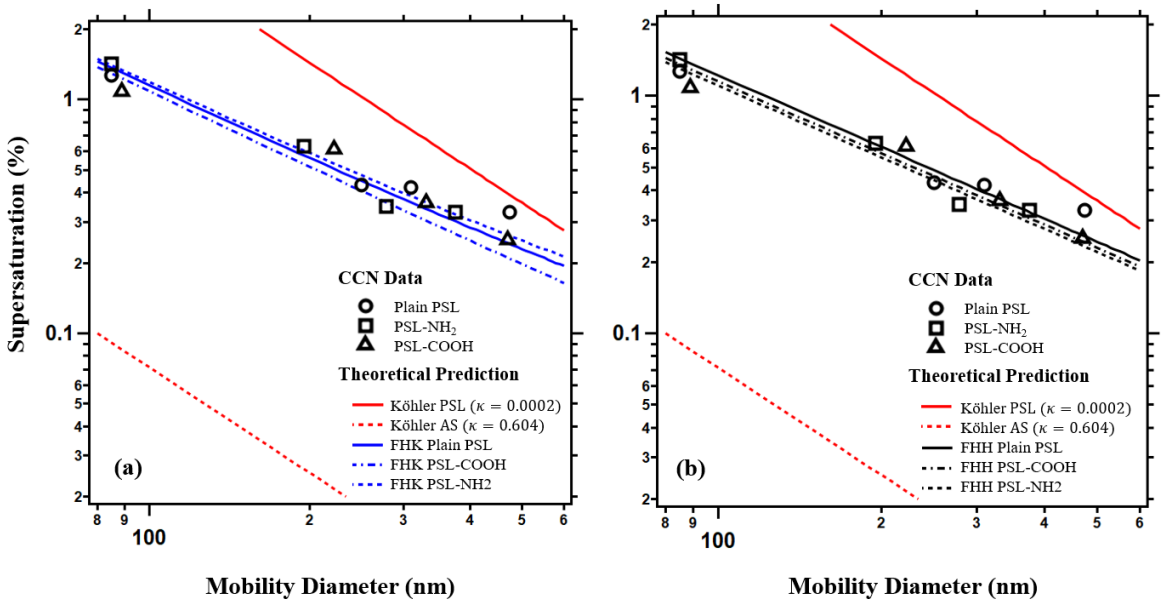

Figure 3-1: The s_c-D_d data for different types of PSL. The dashed red line is the tradition Köhler prediction for ammonium sulfate ($\kappa = 0.604$). All types of PSL particles are more hygroscopic than the traditional hygroscopicity prediction ($\kappa_{int} = 0.0002$, red solid line). (a) Blue lines show the prediction from FHK. (b) Black lines show the prediction from FHH-AT model, with B_{FHH} =1.

Table 3-1 also shows the fitted parameters for the FHK, and FHH-AT models required to subsequently calculate κ_{FHK} and $\kappa_{FHH,the}$. Both FHK and FHH-AT models have additional degrees of freedom compared to the traditional Köhler theory. In the FHK model, the molar volume becomes negligible and the water-polymer interaction parameter (χ), drives the droplet activation. χ describes the repulsive and attractive force between the solvent and the polymer. A χ smaller than 0.5 is an indication of miscibility and that water is a "*good solvent*" (Pethrick 2004). χ is the only empirical free parameter in this study and when fitted to all

three types of PSL, $\chi > 0.5$ and confirms the assumption that PSL particles are water insoluble. In Figure 3-1a, the FHK model with only one free fitting parameter more closely agrees with experimental data than the TK theory (red solid lines).

Two empirical parameters (A_{FHH} and B_{FHH}) for the FHH-AT model are reported for each type of the PSL. The FHH-AT model with two degrees of freedom agrees with the experimental data better than the traditional Köhler theory model (Figure 3-1b) with $R^2 > 0.9$. However, multiple solutions of A_{FHH} and B_{FHH} may exist. The fit results for plain type PSL estimate A_{FHH} = 0.17 and B_{FHH} = 0.99; A_{FHH} is 0.3 and B_{FHH} is 1.08 for carboxyl functional group modified PSL; A_{FHH} is 0.11 and B_{FHH} is 0.83 for amine functional group modified PSL. Differences in the A_{FHH} and B_{FHH} values confirm that the FHH-AT model is sensitive to molecular level chemistry and can distinguish changes in surface chemistry. PSL-COOH shows a higher attraction to water molecules than the plain PSL. However, PSL-NH_2 is the most hygroscopic among the three types of the PSL and the A_{FHH} =0.11 and the B_{FHH} = 0.83 of PSL-NH_2 are the lowest values among all three types. If A_{FHH} represents the interaction between the first layer water molecules and the surface of the PSL particles, a higher A_{FHH} value implies higher attractive forces. Thus, the unconstrained FHH-AT parameter solutions must be reassessed.

The only chemical difference between the three types of PSL is due to surface modification. The attraction force between the particle core and the layers of the water molecules should be the same. Thus, a second constrained best-fit solution exists if we restrict

B_{FHH} =1 (Table 3-1). The constrained and fitted A_{FHH} is 0.18 for plain PSL, 0.21 for PSL-COOH and 0.23 for PSL-NH_2 (Table 3-1, Figure 3-1b). With the constrained solution, the higher A_{FHH} is consistent with the most hygroscopic aerosol species. In Figure 3-1b, the FHH-AT model prediction agrees well with the experimentally measured s_c-D_d data more than traditional Köhler Theory. This agreement with data is true for both the best-fit constrained (B_{FHH} =1, Figure 3-1b) and unconstrained A_{FHH} and B_{FHH} values (not shown).

Table 3-1: Important aerosol physical properties and parameters used to derive droplet growth.

κ_{int} (-)	χ (-)	A_{FHH}(-)	B_{FHH}(-)	Surface Modification	D_d (nm)	s_c (%)
0.0002	0.56	0.18	1	Plain	85	1.27
					250	0.43
					310	0.42
					474	0.33
0.0002	0.54	0.21	1	-COOH Carboxyl	89	1.08
					223	0.61
					331	0.36
					472	0.25
0.0002	0.57	0.23	1	-NH_2 Amine	85	1.42
					195	0.63
					278	0.35
					375	0.33

3.4.2 The Impact of Surface Chemistry to Hygroscopicity of PSL

The perceived single parameter hygroscopicity, κ_{TK} and the κ_{FHH} can be derived

from traditional Köhler and FHH-AT models, respectively (Figure 3-2). In TK, the theoretical hygroscopicity is a constant value independent to the size of the particles. In Figure 3-2 (a), the red solid horizontal line shows $\kappa_{int} = 0.0002$. The red open symbols (circle, square and triangle) are the hygroscopicity from measured data (Equation (3.3)) of the respective PSL particles. The experimental κ_{TK} values from traditional Köhler theory range from 0.002 to 0.04. Additionally, κ_{TK} of the PSL are size dependant and are larger than κ_{int}. Thus, TK should not be applied to predict the droplet growth and single parameter hygroscopicity of insoluble PSL particles.

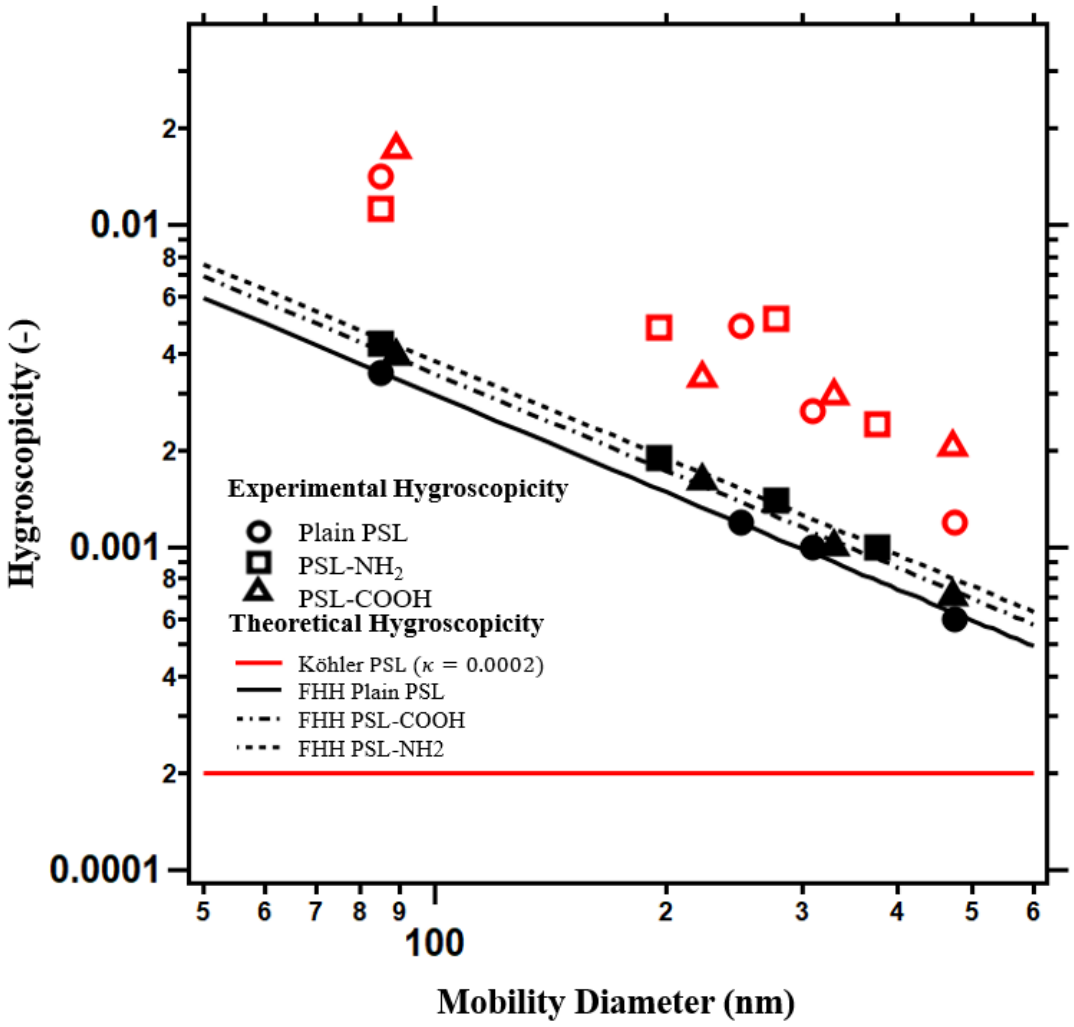

Figure 3-2: The single hygroscopicity parameter predicted from FHH-AT and traditional Köhler theory. Köhler theory from intrinsic properties (solid red line) predicts a constant hygroscopicity across particle sizes and hygroscopicity derived from experimental data (open symbols) shows size dependence. Hygroscopicity derived from FHH-AT model from theory (solid black lines) and from experimental data (black symbols) are size dependent and agree well. Hygroscopicity derived from FHH-AT model is also sensitive to surface chemistry functionality.

In addition, FHK should not be used to predict droplet growth of PSL. Although the

FHK model agrees well with s_c-D_d data (Figure 3-1a), the derived hygroscopicity is problematic and nonsensical (therefore not shown). FHK assumes that the hydrophilic polymer swells in the water droplet and the interaction parameter represents the molecular force between water and polymer. χ values larger than 0.5 derived from PSL-NH_2, PSL-COOH and plain PSL subsequently estimate negative and implausible κ_{FHK} values. The experimental data indicate that the PSL indeed grow into droplets and have a positive hygroscopicity. Thus, FHK should not be applied to water-insoluble polymers like PSL.

The hygroscopicity values derived from the FHH-AT model are plausible and show the best agreement between theory and experiment (Figure 3-2). Both theoretical ($\kappa_{FHH,the}$) and experimental ($\kappa_{FHH,exp}$) hygroscopicity values from FHH-AT model are less than the κ_{TK} (red open symbols), but higher than a constant κ_{int} value of 0.0002. $\kappa_{FHH,exp}$ and $\kappa_{FHH,the}$ for all twelve PSL are within 5% of each other. The small deviation between $\kappa_{FHH,the}$ and $\kappa_{FHH,exp}$ demonstrate that the adsorption model is best for PSL. For insoluble particles, the experimental single parameter hygroscopicity is size dependent and decreases with an increasing diameter (Figure 3-2). This is because the core does not dissolve, and the total volume of the dry particle (Equation (3.2)) does not fully participate in the water uptake. The particle surface of an insoluble particle is proportional to the square of the size and dominates the adsorption-based water activation behavior. However, the single parameter hygroscopicity is defined by the volume ratio of the solute and the solvent, which is proportional to the cube

of the size. In adsorption driven growth, the core inactive particle volume enlarges when the particle size increases and as a result the perceived size dependence in the experimental hygroscopicity is exhibited. The FHH-AT model accounts for the core volume contribution to the water activation in the B_{FHH} parameter. In the special case of PSL particles, B_{FHH} happens to be 1 (Table 3-1), hence the $\kappa_{FHH,the}$ is directly the reciprocal of the dry size (Equation (3.8)). $\kappa_{FHH,the}$ accurately describes the inactive core volume behavior, demonstrating a decrease of hygroscopicity with an increasing particle size. Larger particles still activate at lower supersaturation than smaller particles. For example, 500 nm particles activate earlier than 100 nm particles at 0.3% supersaturation due to a larger surface area which provides more active sites for adsorption. Moreover, FHH-AT hygroscopicity is also sensitive to the small differences in surface chemistry. The theoretical prediction for the CCN activation of PSL-NH_2 particles (the dashed line) is larger than PSL–COOH (dashed-dotted line), while the plain PSL is the lowest (solid line).

3.5 Summary and Future Work

PSL are spherical, insoluble, non-porous, mono-dispersed particles and their surface can be modified to be hydrophilic or hydrophobic. The performance of the adsorption model is better than the traditional Köhler for PSL particles; experimentally derived κ_{TK} predicts a

higher hygroscopicity and κ_{int} approaches zero. κ_{FHK} is negative for the insoluble particles and is inconsistent with the growing droplets. The single parameter hygroscopicity of the FHH-AT model replicates the small differences of the functionalized surface. $\kappa_{FHH,exp}$ and $\kappa_{FHH,the}$ are only within 5% differences. $\kappa_{FHH,the}$ decreases with an increasing particle size, demonstrating the inactivity of the inner core of larger particles.

Using a droplet growth model with additional degrees of freedom improves the droplet growth prediction of PSL. The FHH-AT model is typically applied to effectively water-insoluble particles and the adsorption model agrees well with the experimental droplet growth data for hydrophobic and hydrophilic functionalized surfaces. This finding is consistent with the current body of work that highlights the bulk aerosol composition as a critical factor in aerosol water uptake. However, the addition of polar functional groups to the surface of the water-insoluble particle exhibits discernible differences in activation and suggests that for atmospheric insoluble aerosol (e.g., soot, mineral dust) the modified surface chemistry should not be ignored.

We found from experiments that B_{FHH} was ≈ 1 for pure and coated PSL particles. This implied that for the samples studied in this work, B_{FHH} could be constrained to 1 to determine the A_{FHH} and postulate the contribution of surface chemistry on the CCN activation. The method of constraining B_{FHH} can distinguish both the surface modification and potential coatings when the B_{FHH} of the core is known. If B_{FHH} of the pure core is known, only A_{FHH}

needs to be measured and accounted for to estimate water uptake ability. Furthermore, it was found that if both A_{FHH} and B_{FHH} are left unconstrained, the values of A_{FHH} come out to be within 5% of the A_{FHH} when B_{FHH} is constrained. It is also important to note that the κ_{FHH} depends only on the surface properties of the compound (A_{FHH}) when B_{FHH} is constrained to unity. This can imply that the hygroscopic properties of the compound will only depend on the hydrophilic or hydrophobic properties of the functionalized surface regardless of the bulk properties if B_{FHH} is constrained to unity. In other words, extensions of this work could potentially apply A_{FHH} water-adsorption properties to similarly functionalized surfaces with different particle core compositions (i.e., varying B_{FHH}).

The findings presented here may be extended to atmospherically relevant insoluble particles that may be either coated or surface oxidized during different chemical processes. In ambient measurement, quite rarely is the composition of the surface and core simultaneously known; single particle measurements are required to discern the individual composition and morphology. Thus, the singular κ_{FHH} value provides an important utility. Regardless of whether the FHH-AT model is constrained, κ_{FHH} reduces the the degrees of freedom of the model and can discern changes in surface chemistry. It should be noted that the extent to which the adsorption-driven droplet growth can be applied to increasingly hydrophilic aerosol is uncertain but has been explored. Readers who are interested in the adsorption driven water uptake ability of partially soluble compounds are referred to a companion paper Gohil et

al(Gohil et al. 2022). In summary, water-insoluble aerosol can adsorb water and if their surfaces have been oxidized or functionalized with polar groups the aerosol can enhance their efficiency for water-uptake.

Chapter 4: Quantifying the Multiple Charging Errors in DMA

4.1 Background

Accurate measurements of aerosol optical properties are critical to minimize uncertainty in predictions of the aerosol effect on the Earth's energy balance. Current estimates suggest that aerosols adsorb and scatter light and have an overall negative radiative forcing that can cool down earth's surface temperatures (IPCC 2021); however these estimates are uncertain and range from -1.33 to 0.66 W m^{-2}. Zarzana et al. 2014 calculated the errors of radiative forcing from refractive indices and determined a 10% error in radiative forcing is generated if the real part (n) in refractive index is 1.50 instead of 1.53 for 200nm ammonium sulfate particles. Thus the refractive index (RI), when accurately measured in the laboratory, can decrease the overall uncertainty in radiative forcing.

A common method to retrieve the refractive index measures the extinction and the absorption cross section of a pure substance (Cotterell et al. 2020; 2015; Zarzana, Cappa, and Tolbert 2014; Miles et al. 2011; Mason et al. 2012; Radney and Zangmeister 2018; Lang-Yona et al. 2009). CRD (O'Keefe and Deacon 1988) is one of the common techniques used to measure the extinction cross section, C_{ext} (Moosmüller, Chakrabarty, and Arnott 2009), and efforts have been made to increase the accuracy of the measured C_{ext}. Several papers have

quantified the accuracy of measurement by characterizing pure scattering polystyrene (PSL) particles of known sizes (Pettersson et al. 2004; S. Singh et al. 2014; Miles et al. 2011). Since the size of the PSL is known and a constant, the measured C_{ext} from CRD is usually accurate. Pettersson et al. 2004 compared the measured C_{ext} from CRD with the C_{ext} calculated from Mie theory and found differences within 5% for PSL. Later, Miles et al. 2011 showed that the error of the real part (n) of the refractive index for polystyrene particles could be -0.5% to +0.3%. Singh et al. 2014 investigated the systematic errors for CRD and concluded that 10% to 11% of PSL C_{ext} is attributed to the particle number concentration counting efficiency. However, sizing errors are compounded with errors from particle number concentration counting efficiency for polydisperse aerosol compositions.

A particle size classifier is often connected before the CRD to measure non-uniform size scattering aerosols. Previous studies have used a variety of particle classifying instruments (e.g, but not limited to the Bessell Beam.(Cotterell et al. 2015)), Aerosol particle Mass analyzer (Radney and Zangmeister 2018),etc) to measure C_{ext}. The Differential Mobility Analyzer (DMA) is the most widely used with the CRD. The DMA selects aerosol by their electrical mobility and has multiple-charging artifacts.

Several groups have reported size selected optical properties with the CRD and in some cases have discussed sources of potential error in the measurement. Lang-Yona et al. 2009 used the DMA-CRD and reported the RI for polystyrene and ammonium sulfate. The reported RI,

m, is equal to the real (*n*) and imaginary parts (*k*). For polystyrene and ammonium sulfate *m=1.60+0.01i* and *m=1.52+0.01i* respectively (Lang-Yona et al. 2009). Although both of the substances were pure scattering, the imaginary parts were still non-zero. Bluvshtein et al. 2012 proposed new approaches for RI retrieval by measuring the C_{ext} of ammonium sulfate, Suwannee river fulvic acid, and nigrosine with different size ranges. For pure scattering ammonium sulfate, Bluvshtein et al. attributed the absorption errors (*k=0.030 and 0.054*) to the multiply charging from the DMA, although doubly charged particles were corrected. Mason et al. 2012 measured sodium nitrate particles using both DMA-CRD and optical tweezers and reported a precision of ±0.0012 for the optical tweezers and ±0.02 for the CRD technique. They also considered the doubly charged particles, but concluded that the number concentration of particles carrying three or more charges were too low to contribute to the C_{ext} errors. Toole et al. 2013 suggested a calibration method for CRD that decreased the C_{ext} errors from 11% to 2% for liquid squalane particles. However instead of the multiple charging, they pointed out that the particle's counting efficiency is a crucial factor affecting the CRD performance as also stated in Miles et al 2011.

Multiple charging issues are inevitable when using the DMA to classify and calculate the C_{ext}. Most researchers who apply multiply charge corrections typically consider only doubly charged particles; since the sum number concentration for triply or more charged particles are considerably lower (< 5%). Currently, the assumption of a negligible fraction of

the multiply charged particles is the result of the pre-charging size distribution and low predicted probability of particles carrying higher charges (Gunn 1955; Tigges et al. 2015). Tigges et al. 2015 proposed the charging probability using soft x-ray neutralizer as a charging source, and the probability of a 200nm carrying singly charged particles and doubly charged particles was 0.22 and 0.08 respectively. The Gunn's model calculated the probability for particles carrying charges more than 3, and for the 200nm particles the probability was 0.023. In other words, the likelihood of particles carrying three charges is very low. The low charging probability continues to justify ignoring the contribution of triply or more charged particles in C_{ext} measurement even though the initial charge across the size distribution is unknown and may be different in each independent sample.

Additionally, the multiply charged particles are larger in size than the singly charged particles. Overall, the Mie theory predicted C_{ext} is positively correlated to the particle size (outside the dangle plateau region according to the wavelength); larger particles typically have larger C_{ext}. Although the number concentration of the multiply charged particles are low, the size of the multiply charged particles could be sufficiently large enough to contribute to the C_{ext} errors. For 200nm size selected particles, the size of doubly and triply charged particles are 327nm and 441nm respectively. For example, the C_{ext} of a 441nm ammonium sulfate particle is 20 times that of the 200nm particles from Mie theory for wavelength 405nm. For 200nm ammonium sulfate particles, (Cotterell et al. 2020) recently considered particles carrying up to

6 charges, and concluded that the contribution of the 3, 4, 5, 6 charges-carried particles in C_{ext} measurement which could reach 27.2%, 10.9%, 5.4%,1% respectively. This more recent work suggests that triply and more charged particles may not be negligible.

There are multiple methods to acquire the fraction of the multiply charged particles; these methods include scanning the full size distribution of the aerosols and correcting the number concentration by the charging theory. Another method uses a second DMA to separate the multiply charged particles directly (the TDMA method). Radney et al. 2013 used the TDMA methods to retrieve the fraction of singly, doubly, triply and quadruply charged particles. Mamakos 2016 proposed a method to calculate the fraction of the doubly-doubly charged particles in both DMAs. The results of these TDMA studies can be applied to understand the fractions of multiple charged particles for C_{ext}.

The above TDMA methods are limited by the maximum size range that is controlled by the sample flow rate and time. All the singly charged particles that are larger than maximum measured size ranges are not counted. If the number concentration of the singly charged large particles is not measured, the number concentration will not be considered in both TDMA and full scan size distribution methods. Meanwhile such particles out of the measured size range could carry multiple charges and be included in the targeted, singly charged size particles. These particles may cause errors in C_{ext} that should not be ignored. A theoretical estimation for the fraction of the multiply charged particles that accounts for experimental size measurement

limitations is needed.

In this chapter, we demonstrate the impact of the multiply charged particles in the measurements with and without the installation of the impactor. The TDMA method that separates multiply charged particles is applied to investigate the existence of large particles. Since it is impossible to remove all the multiply charged particles with the electrical mobility current techniques, a predictive method is derived to quantitatively calculate the fraction of the multiply charged particles. We also estimate graphically the fraction of the multiply charged particles that cause a 5% difference in the extinction cross section measurement. The quantification of multiple charge errors for C_{ext} measurement improves the accuracy of values applied to understand particle direct effects on climate.

4.2 Experimental Methods

Figure 4-1 shows three experimental setups used to determine: a) C_{ext} for size and mass selected particles, b) C_{ext} for size selected particles. The arrangement is similar to that of Radney and Zangmeister (Radney and Zangmeister 2018). For all optical measurements, a 0.0457 cm impactor (Imp in Fig. 1) was utilized upstream of the DMA and operated at a flow of 0.55 L min^{-1} corresponding to a calculated cut-point diameter of 355 nm. Vacuum grease was applied on the impactor collection plate to minimize particle bounce.

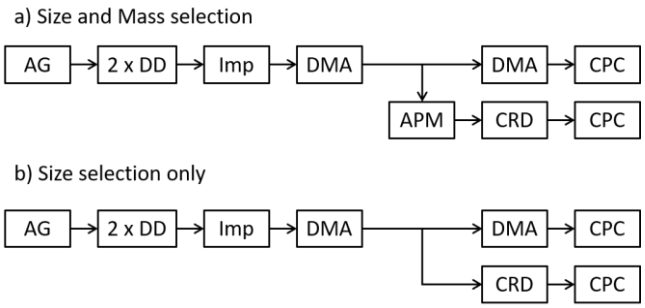

Figure 4-1: Experimental block diagram for a) size and mass selection and b) size selection only. Abbreviations: aerosol generator (AG), aerosol particle mass analyzer (APM), cavity ring-down spectrometer (CRD), condensation particle counter (CPC), differential mobility analyzer (DMA), diffusion dryer (DD) and impactor (Imp). See discussion in text for further details.

4.2.1 Aerosol generation and conditioning.

Polydisperse aerosols were generated using a constant output Collision-style atomizer at 25 psig and a 1 mg mL^{-1} solution of ammonium sulfate (AS, $(NH_4)_2SO_4$). 0.55 L min^{-1} or 0.85 L min^{-1} of the 2.2 L min^{-1} of aerosol-laden flow generated was sampled for the optical (Fig. 1a and 1b). The aerosol was dried by passing through a pair of silica gel diffusion dryers. Relative humidity (RH) was monitored in the sheath flow of the upstream DMA. When RH increased above 10 %, the desiccant was changed.

4.2.2 Cavity ring-down spectrometer

The CRD is similar to that in Radney and Zangmeister (Radney and Zangmeister 2018) and the wavelength, λ, was set at 405 nm. Only a brief description of cavity ring-down spectroscopy is provided here, and the reader is directed to Atkinson (Atkinson 2003) for a more complete description. A high finesse optical cavity consisting of a pair of plano-concave mirrors (λ = 405 nm, reflectivity ~ 99.975 %, transmission ~ 0.01 %) is pumped by a continuous wave diode laser to saturation. The light intensity is then quickly (< 10 ns) terminated using an acousto-optic modulator (AOM). The light intensity inside the cavity decays passively and exponentially and can be described by

$$\frac{I}{I_0} = e^{(-t/\tau)} \quad (4.1)$$

where I is the measured laser intensity at time t, I_0 is the initial intensity and τ is the ring-down time (the amount of time that it takes for the intensity of light to decrease by $1/e$). τ is the inverse of the decay constant ($\beta = \tau^{-1}$) that includes contributions from the absorption of light by gases ($\beta_{abs,gas}$) and aerosols ($\beta_{abs,aero}$), the scattering of light by aerosols ($\beta_{scat,aero}$) and mirror losses (β_{mirror})

$$\beta = \beta_{abs,gas} + \beta_{abs,aero} + \beta_{scat,aero} + \beta_{mirror} \quad (4.2)$$

Compared to other β contributions, Rayleigh scattering by gases ($\beta_{scat,gas}$) is negligible and has been omitted. Decay constants for the aerosol contributions can be determined from the difference between β for aerosol-laden and aerosol-free measurements.

Since the CRD measures both absorption and scattering by aerosols, it is convenient to refer

to the sum of these terms as extinction ($\beta_{ext} = \beta_{scat} + \beta_{abs}$). β can be related to the extinction coefficient (α_{ext}) through the speed of light (c)

$$\alpha_{ext} = \left(\frac{\beta_{ext}}{c}\right)\left(\frac{L_{cavity}}{L_{aero}}\right) \qquad (4.3)$$

The L_{cavity}/L_{aero} term is included to account for the fact that only a portion of the mirror separation distance contains aerosol; a HEPA-filtered backflush is delivered to both mirrors at 25 cm^3 min^{-1} to prevent particle deposition. For the spectrometer used here, L_{cavity}/L_{aero} = 73 cm/49 cm = 1.49.

The AOM was driven with a square wave pattern at 1 kHz with ring-down events and data acquisition being triggered on the falling edge. Ring-down data was collected at 125 MHz for 6.25×10^4 samples of which only the first 7τ were transferred to the computer for fitting using a corrected successive-integration routine (Everest and Atkinson 2008; Halmer et al. 2004). τ were converted to α_{ext} with both values retained and averaged to 1 s. All other data was discarded. The 1s τ typically represents the average of ~ 500 independent ring-down events; data collection rate is limited by the transfer speed of the Peripheral Component Interconnect express (PCIe) bus. At 1 s, the average aerosol-free τ, relative standard deviation and limit of detection (3C) are 7.03×10^{-6} s, 1 % and 1.5×10^{-5} m^{-1}, respectively.

4.2.3 Size and mass selection measurements

Distributions of α_{ext} and particle number concentration (N) as a function of mass (m) were

measured by scanning the voltage (V) of the aerosol particle mass analyzer (APM) at a constant rotation speed (ω) and a classification parameter $\lambda_c = 0.32$ (Ehara, Hagwood, and Coakley 1996; Tajima-Hatashita 2013). N, V and ω were sampled at 20 kHz and averaged to 1 s. The 1 s data were logged for further analysis.

Distributions of α_{ext} and N were collected for 10 min at each diameter, D_m, and the resulting data fit to a bi-Gaussian distribution(Buys and De Clerk n.d.).

$$f(m) = \begin{cases} f(m)_{max} \times \exp\left(\frac{-(m-m_p)^2}{2\sigma_1}\right) & m \leq m_p \\ f(m)_{max} \times \exp\left(\frac{-(m-m_p)^2}{2\sigma_2}\right) & m \geq m_p \end{cases} \quad (4.4)$$

where f(m), $f(m)_{max}$ m_p and C are the measured quantity (α_{ext} or N), the peak of the distribution, the average mass and the width of the distribution, respectively. The σ_1 and σ_2 denote that the distribution is not symmetric but exhibits a "tail" towards higher masses since $m \propto D_m^3$. Because of the high mass density of $(NH_4)_2SO_4$ (ρ = 1.77 g cm^{-3}), sufficient resolution existed between particles bearing charge, q = +1 and q > +1, so only the q = +1 peaks were fit(Radney and Zangmeister 2016).

Using the calculated fit parameters, the average extinction cross-section ($C_{ext,dist}$) of the distribution was calculated from the ratio of the integrals

$$C_{\text{ext,dist}} = \frac{\int \alpha_{\text{ext}} dm}{\int N dm} = \frac{\alpha_{\text{ext,max}}}{2N_{\text{max}}}\left(\frac{\sigma_{\alpha,1}}{\sigma_{N,1}} + \frac{\sigma_{\alpha,2}}{\sigma_{N,2}}\right) \quad (4.5)$$

Uncertainties in $C_{ext,dist}$ represent the propagated 1 σ uncertainties in all fit coefficients.

Measured $C_{ext,dist}$ were validated by comparing measured values for size and mass selected

polystyrene nano-spheres (PSL, physical diameters = 203 nm and 296 nm) to those calculated using Mie theory assuming a refractive index of 1.6255 +0i (X. Zhang et al. 2020). $C_{ext,dist}$ agreed with theory to better than 0.4 % at both sizes. Note, the CPC used in conjunction with the CRD was calibrated in this study by the manufacturer immediately prior to data collection.

4.2.4 Size selection only measurements

Immediately following the completion of a mass distribution scan, the ensemble extinction cross-section ($C_{ext,ens}$) was determined from

$$C_{\mathrm{ext,ens}} = \frac{\alpha_{\mathrm{ext}}}{N} \qquad (4.6)$$

by measuring α_{ext} and N at the selected D_m for 240 s; see Fig. 1b for experimental layout. α_{ext} and N were averaged and $C_{ext,ens}$ calculated and uncertainties in $C_{ext,ens}$ represent the propagated 1σ standard deviations in α_{ext} and N. The APM was left inline during measurement of $C_{ext,ens}$ to ensure direct comparability to $C_{ext,dist}$.

4.2.5 Size distribution measurements

Aerosol size distributions were measured by a scanning mobility particle sizer (SMPS, tandem scanning DMA and CPC) in parallel to the CRD-CPC. Size distribution measurements were 300 s long and spanned 15.1 nm $\leq D_m \leq$ 850.5 nm. To ensure comparability of the size distributions between $C_{ext,dist}$ and $C_{ext,ens}$ measurements, two size distributions were collected

during the mass distribution measurements while one size distribution was collected during the measurements of $C_{ext,ens}$.

4.3 Results

4.3.1 $C_{ext,ens}$ and $C_{ext,dist}$

Extinction cross sections for $(NH_4)_2SO_4$ were determined by measuring α_{ext} and N using a CRD and CPC, respectively. Particles were classified either using either a tandem DMA and APM for size and mass selection or only a DMA for size selection. We refer to the C_{ext} measured by these methods as the distribution C_{ext} and ensemble C_{ext} – $C_{ext,dist}$ and $C_{ext,ens}$, respectively – and are shown in Figure 4-2 as black circles and grey squares. An 0.0457 cm impactor was used upstream of the DMA for all measurements; at this flow rate, the cut point diameter was determined to be (354 ± 1) nm (see §3.3).

$C_{ext,ens}$ and $C_{ext,dist}$ were measured at 50 nm increments for 150 nm ≤ D_m ≤ 450 nm; see Figure 4-2. At small D_m, the $C_{ext,ens}$ is greater than $C_{ext,dist}$ by a factor ≈ 3 due to the presence of multiply charged particles which is confirmed by the corresponding size distribution shown in Figure 4-3. As D_m increases, $C_{ext,ens}$ and $C_{ext,dist}$ converge. For example, at D_m = 350 nm $C_{ext,dist}$ = $2.9^{+0.2}_{-0.1}$ × 10^{13} m^2 and $C_{ext,ens}$ = (3.1 ± 0.1) × 10^{-13} m^2 corresponding to a relative difference of 9 %; see Figure 4-2c . At D_m ≥ 400 nm, this difference has decreased to

within measurement uncertainty indicating that for all $D_m \leq D_{50}$, q > +1 are present.

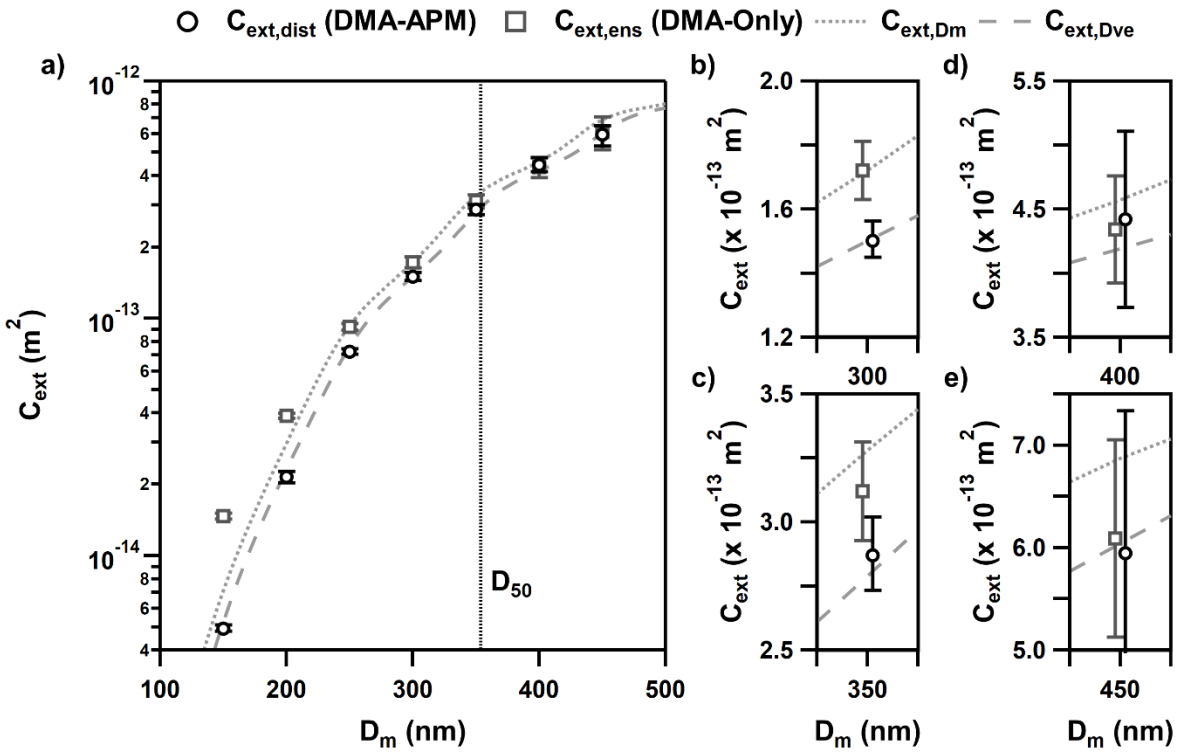

Figure 4-2. a) Extinction cross-section (C_{ext}) as a function of mobility diameter (D_m) determined from mass distribution measurements of size selected particles ($C_{ext,dist}$, black circles) *versus* ensemble values using size selection only ($C_{ext,ens}$, dark grey squares) and theoretical values calculated using Mie theory with the mobility diameter (D_m, dotted grey line) and the volume-equivalent diameter (D_{ve}, dashed grey line) assuming $RI = 1.53 + 0i$ at λ = 405 nm. Dotted black line corresponds to the cut-point diameter (D_{50}) of the impactor. Expanded view of comparisons for D_m = b) 300 nm, c) 350 nm, d) 400 nm and e) 450 nm; values have been horizontally offset ± 0.5 nm of D_m for clarity. Scale along the abscissa in b), c), d) and e) is ± 5 nm. See discussion in text for determination of values and the corresponding uncertainties.

The measured $C_{ext,ens}$ and $C_{ext,dist}$ can be compared to Mie theory assuming a refractive index of $1.53 + 0i$. For the measured data, two options of particle "size" are available from the DMA and APM measurements: D_m and the volume-equivalent diameter (D_{ve}) where

$$D_{ve} = \sqrt[3]{\frac{6m_p}{\pi\rho_p}} \qquad (4.7)$$

D_{ve} represents the diameter of a sphere with the same mass as the particles of interest. Excellent agreement between $C_{ext,dist}$ and $C_{ext,Mie}$ is realized at all D_m when C_{ext} is calculated using D_{ve}; see Fig. 2. For $C_{ext,ens}$, agreement with $C_{ext,Mie}$ when using D_{ve} is only realized at $D_m \geq 400$ nm. Interestingly, however, $C_{ext,ens}$ agrees with $C_{ext,Mie}$ when using D_m for $D_m \geq 250$ nm indicating that it is possible to obtain the "correct" C_{ext}, but for the wrong reasons. Instead, some metric of particle shape, whether as D_{ve} or the shape factor is necessary to determine C_{ext} as particle non-idealities could be offset by a few multiply charged particles.

4.3.2 Tandem DMA (TDMA) size distributions

In addition to measuring $C_{ext,dist}$ and $C_{ext,ens}$ size distributions of particles transmitted by the upstream DMA were re-neutralized and measured by an SMPS. This re-neutralization step redistributes particle charges back to the Boltzmann distribution allowing for identification of particles with $q > +1$ being transmitted by the upstream DMA; unfortunately, some fraction of the particles that initially have $q = +1$ get re-neutralized to have $q > +1$ and will appear smaller

than the initially selected D_m. Measured size distributions are shown in Figure 4-3 as a function of the selected D_m with the D_{50} shown by the dashed grey line. Solid black lines represent the average of 3 size distribution scans while shaded grey areas are the 1σ standard deviations. A total of three distributions were collected successively; two distributions during the measurement of $C_{ext,dist}$ and one distribution during $C_{ext,ens}$. Particles with $q > +1$ are clearly visible for $D_m \leq 350$ nm and are within measurement uncertainty or absent at $D_m \geq 400$ nm. These observations are in agreement with the observed deviations between $C_{ext,dist}$ and $C_{ext,ens}$.

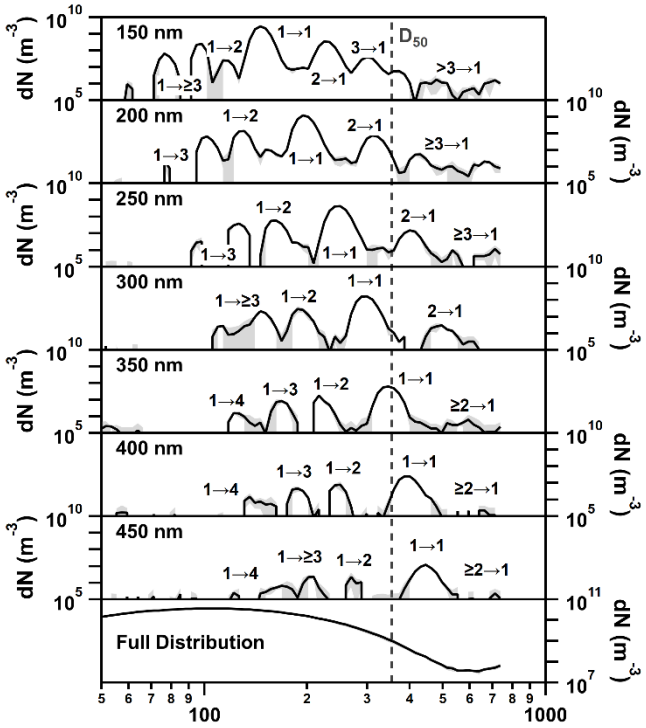

Figure 4-3: Measured tandem DMA size distributions with the upstream DMA set to the D_m shown in each panel. For the full distribution measurements, the flow bypassed the upstream DMA column. Solid black lines and grey shading represent the average and 1σ standard deviation of the three successively measured size distributions: two during $C_{ext,dist}$ measurements and one during $C_{ext,ens}$ measurements. Vertical dashed dark grey line corresponds to the measured D_{50}. Particle q in the upstream and downstream DMA are denoted as $q_1 \rightarrow q_2$ for each peak.

4.4 Discussion

The data presented required a number of instruments (3 CPCs, 2 DMAs, an APM and a

CRD) to demonstrate that particles bearing $q > +1$ and larger than the impactor D_{50} were being transmitted and biasing the optical measurements. Realistically, this collection of instruments is not available to every laboratory or, as is the case in field studies, each instrument is applied to different measurands. For the data presented above, the impactor size was purposefully chosen to guarantee that at least one D_m within the SMPS measurement window (14.1 nm ≤ $D_m \leq 736.5$ nm) would contain only $q = +1$ and facilitate a direct comparison between the C_{ext} measurements by the DMA-APM and DMA-only. Notably, this configuration severely reduced the number of available particles in this $q = +1$ window at $D_m > 355$ nm. As an example, particle number concentration was $> 10^{12}$ m^{-3} in the full distribution but only $(7.1 \pm 0.6) \times 10^7$ m^{-3} of particles were transmitted at $D_m = 450$ nm; a reduction $> 10^4$. Under more "normal" operations, it is unlikely that the D_{50} will be chosen in a way as to throw out more than half of the available measurement window by the SMPS. Additionally, these observations are likely to only apply to laboratory investigations or combustion plumes where particle concentrations are high. Below, we detail a mathematical algorithm to predict the presence of particles bearing multiple charges that are outside of the measurement range – *i.e.*, particles larger than D_{50} or the SMPS measurement window.

4.4.1 Derivation of a mathematical relationship for predicting the fraction of multiply charged particles.

Ideally, the use of an impactor would exclude all particles larger than D_{50} and for DMA measurements should effectively reduce the fraction or eliminates the presence of multiply charged particles. As demonstrated above, in practice, some fraction of particles larger than D_{50} is transmitted, and their contributions can only be quantified theoretically. Here, a linear equation is derived to predict the fraction of multiply charged particles that must be accounted for. The derived linear equation utilizes the following independent assumptions:

Assumption 1: The sum of all aerosol particles (N_{total}) with a specific Z_p bearing some charge q up to a maximum charge (s) is

$$N_{\text{total}} = N_1 + N_2 + \cdots + N_{s-1} + N_s = \sum_{q=1}^{s} N_q \quad (4.8)$$

and the total of all aerosol fractions (f) is one,

$$f_{\text{total}} = \frac{\sum_{q=1}^{s} N_q}{N_{\text{total}}} = \sum_{q=1}^{s} f_q = 1 \quad (4.9)$$

Only particles bearing $q \geq +1$ are considered since these are what are classified by the DMA and APM. Other instrumental configurations, such as a dual polarity DMA, could allow for determination of $q \leq 0$.

Assumption 2: the ratio of number densities of particles in the sample bearing any two specific charges x and y is equal to the ratio of the same fractions of those charges in the measured population

$$\frac{f_x}{f_y} = \frac{N_x}{N_y} \quad (4.10)$$

where N_x is the total number concentration of particles bearing x charges as measured by the

TDMA; i.e. integration of *dN* in Figure 4-3. By rearranging Equation (4.10), it follows that

$$f_x = f_y \frac{N_x}{N_y} \qquad (4.11)$$

Expanding Equation (4.9) to account for any number of terms between charges q and s

$$1 = \sum_{q=1}^{s} f_q = f_1 + f_2 + \cdots + f_{s-2} + f_{s-1} + f_s \qquad (4.12)$$

and utilizing Equation (4.10)

$$1 = f_1 + f_1 \frac{N_2}{N_1} + \cdots + f_1 \frac{N_{s-2}}{N_1} + f_{s-1} + f_s \qquad (4.13.1)$$

$$1 = \frac{f_1}{N_1}(N_1 + N_2 + \cdots + N_{s-2}) + f_{s-1} + f_s \qquad (4.13.2)$$

$$f_1 = \frac{N_1(1-f_{s-1}-f_s)}{N_1+N_2+\cdots+N_{i-2}} = \frac{N_1(1-f_{s-1}-f_s)}{\sum_{q=1}^{s-2} N_q} \qquad (4.13.3)$$

Equation (4.13.3) can be more generally written as

$$f_1 = \frac{N_1\left(1-\sum_{q=r+1}^{s} f_q\right)}{\sum_{q=1}^{r} N_q} \qquad (4.14)$$

where r is some intermediate number of charges such that $q \leq r \leq s$. From the measured data, $(s - r)$ is the number of charges that were measured by the TDMA while r is the number of charges that must be determined theoretically.

Assumption 3: $C_{\text{ext,ens}}$ equals the summation of f_q times corresponding cross section ($C_{\text{ext},q}$) and that a corresponding C_{ext} for each particle size can be calculated from Mie theory

$$C_{\text{ext,ens}} = \sum_{q=1}^{s} f_q C_{\text{ext},q} = \sum_{q=1}^{s} f_q C_{\text{ext,Mie},q} \qquad (4.15)$$

This relationship can be expanded

$$C_{\text{ext,ens}} = f_1 C_{\text{ext,Mie},1} + f_2 C_{\text{ext,Mie},2} + \cdots + f_{s-2} C_{\text{ext,Mie},s-2} + f_{s-1} C_{\text{ext,Mie},s-1} + f_s C_{\text{ext,Mie},s} \qquad (4.16)$$

Utilizing the relationship in Equation (4.13.3) allows Equation (4.16) to be factored

$$C_{\text{ext,ens}} = f_1\left(C_{\text{ext,Mie},1} + \frac{N_2}{N_1}C_{\text{ext,Mie},2} + \cdots + \frac{N_{s-2}}{N_1}C_{\text{ext,Mie},s-2}\right) + f_{s-1}C_{\text{ext,Mie,s}-1} +$$

$$f_s C_{\text{ext,Mie},s} \qquad (4.17)$$

Substituting for f_1 using Equation (4.15)

$$C_{\text{ext,ens}} = \frac{N_1\left(1-\sum_{q=r+1}^{s} f_q\right)}{\sum_{q=1}^{r} N_q}\left(C_{\text{ext,Mie},1} + \frac{N_2}{N_1}C_{\text{ext,Mie},2} + \cdots + \frac{N_{s-2}}{N_1}C_{\text{ext,Mie},s-2}\right)$$

$$+f_{s-1}C_{\text{ext,Mie},s-1} + f_s C_{\text{ext,Mie},s} \quad (4.18)$$

and distributing N_1 yields

$$C_{\text{ext,ens}} = \frac{\left(1-\sum_{q=r+1}^{s} f_q\right)}{\sum_{q=1}^{r} N_q}\left(N_1 C_{\text{ext,Mie},1} + N_2 C_{\text{ext,Mie},2} + \cdots + N_{s-2}C_{\text{ext,Mie},s-2}\right)$$

$$+f_{s-1}C_{\text{ext,Mie},s-1} + f_s C_{\text{ext,Mie},s} \quad (4.18)$$

Combining and rearranging

$$C_{\text{ext,ens}} = \frac{\left(1-\sum_{q=r+1}^{s} f_q\right)}{\sum_{q=1}^{r} N_q}\left(\sum_{q=1}^{r} N_q C_{\text{ext,Mie},q}\right) + \sum_{q=r+1}^{s} f_q C_{\text{ext,Mie},q} \qquad (4.19)$$

At this point, it is useful to define a "calculated C_{ext}" ($C_{\text{ext,calc}}$) that represents the theoretically calculated C_{ext} using Mie theory and only those particle sizes that could be identified in the TDMA data.

$$C_{\text{ext,calc}} = \frac{\sum_{q=1}^{r} N_q C_{\text{ext,Mie},q}}{\sum_{q=1}^{r} N_q} \qquad (4.20)$$

Substituting Equation (4.20) into Equation (4.19)

$$C_{\text{ext,ens}} = \left(1 - \sum_{q=r+1}^{s} f_q\right)C_{\text{ext,calc}} + \sum_{q=r+1}^{s} f_q C_{\text{ext,Mie},q} \quad (4.21)$$

Distributing and rearranging

$$C_{\text{ext,ens}} - C_{\text{ext,calc}} = \sum_{q=r+1}^{s} f_q\left(C_{\text{ext,Mie},q} - C_{\text{ext,calc}}\right) \qquad (4.22)$$

Equation (4.22) is fundamental to the analysis and will be applied to the measured data in the next section.

4.4.2 Predicting the Fraction of the Multiply Charged Particles

In Figure 4-4 we apply the Equation (4.22) to 150nm size selected particles. In this case, the singly, doubly and triply charged sizes are 150nm, 238nm and 316nm respectively. The black line shows that the $C_{ext,calc}$ equals to cross-section of a singly charged particle calculated from Mie theory, C_1. Hence in a two variable equation, the expected predicted multiply charged fraction now are the doubly charged (238nm) and triply charged (316nm) particles. If all the higher multiple charges are $q=3$ (x-axis → 0 for the black line) the multiply charged fraction approaches ~ 0.15. However, since the probability of carrying three charges is usually less than doubly charged from charging theory (Tigges et al. 2015; Gunn 1955), the fraction should also be less in most of the cases. Hence, it can be assumed that the fraction of $q=3$ should be less than $q=2$. The dashed line in Figure 4-table shows the limit where $f_q = f_{q-1}$. For example, if the fraction of $q=2$ and $q=3$ are about the same, then the where the solid black intersects the dashed black line indicate the fractions of $q=2$ and $q=3$. The summation of the fraction of the multiply charges $q=2$ and $q=3$ is thus 0.24. In summary, the black line in Figure 4-4 shows that 15~25% of the doubly and triply charged particles could cause the 80% relative error from single DMA measurement (Figure 4-2), when only singly charged particles are considered.

$C_{ext,calc}$ can also consist of C_1 and C_2, which is represented by the red line in Figure 4-4 The unknown fraction now is the fraction of *q3* and *q4*, and the expected multiply charged fractions range from 0.03~0.04. Again, according to the calculation, the doubly charged (red line) shows that a 31% error of the extinction cross section measurement was now caused by the a 3% to 4% amount of the q3 and q4 charged particles. The blue line tells the same story with now for the unknown f_4 and f_5, and $C_{ext,calc}$ consists of C_1, C_2 and C_3. This analysis can be applied for successively higher charged fractions. However, Figure 4-4 shows that higher charged fraction analysis approach the origin and hence the relative error of this higher charged particles approaches zero.

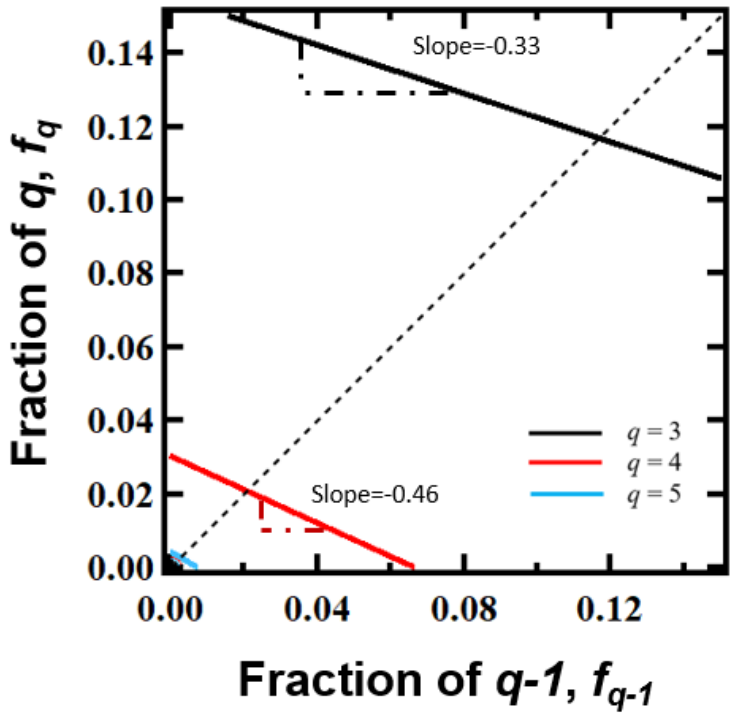

Figure 4-4: The application of Equation (4.22) to the 150 nm with k=2. The middle dashed line represents the fraction of q equals to the fraction of q-*1*. Usually the fraction of q-*1* is expected to be larger than q due to the charging theory. However, the fraction of the multiply charged particles also depends on the size distribution before charging. The fraction of the q could still be larger than q-*1* if the number concentration of q before charging is much more than q-*1*.

Table 4-1: The slope of the Equation (4.22) for diameter 150, 200, 250, and 300 nm. The slope approaches to zero implies the significance of the higher charges. When slope approaches to -1 or even smaller than -1, the compared diameters are both in the Dangle area of Mie spectrum. The sum of the predicted fraction of the two multiple charges will almost be a constant.

D_m (nm)	q=3, q-1=2	q=4, q-1=3	q=5, q-1=4
150	-0.33	-0.46	-0.57
200	-0.35	-0.58	-0.86
250	-0.44	-0.85	-1.13
300	-0.68	-1.07	-0.44

4.4.3 The Slope

The slope of the Equation (4.22) compares the cross section of q and q-1. Outside dangle area in the Mie spectrum, the cross section of the particles of q was typically greater than q-1; thus the slope in most situations would be larger than -1 (Table 4-1). As a result, as the slope approaches zero, the cross section of particles that carry q charges becomes more important, even though the number concentration of q may be small. Specifically, in this case, a small amount of particles carrying q charges could cause the ensemble cross section to increase. In Figure 4-4, the black line compares the contribution of a C_1 and C_2 for 150nm. The slope for black line(q=3) is -0.33 and shows that that C_2 is much larger than C_1, and is an important

contribution in the $C_{ext,meas}$.

If the compared charges are both in the size range of the dangle area (Mie theory plateau that does not monotonically increase) then the slope could be smaller than -1. Notice that the slope of 250nm for q=5 and 300nm for q=4 in Table 4-1. Both of the slope is now smaller than -1, which means the compared multiply charged diameters are now in the dangle area. If the slope of the line is -1, then the sum of the fraction of the q and $q-1$ would always be the same. The expected fraction of the multiply charged now becomes a constant. This suggests that including the fraction of qi is not effective. $q+1$ can be included if one wants to further enhance the accuracy from multiple charging. For example, although the slope of 300nm for q=4 is -1.07, the slope for q=5 increases to -0.44. In regards of the Mie theory, C_4 may not be important for 300nm, but C_5 may contribute to the C_{ens} although the f_5 could be small.

4.4.4 The contribution of multiple charges to relative error. The 5% Origin

In Figure 4-4, a positive intercept shows the $C_{ext,meas}$ is larger than $C_{ext,calc}$. This indicates the existence of multiply charged particles in the measurement. The distance of the line and the origin in Figure 4-4 shows the error in cross section measurement. When the line gets closer to the origin, the difference of the $C_{ext,meas}$ and $C_{ext,calc}$ is less. Thus we can set the limits of a tolerance level for measurement in relative error from multiply charged particles.

To do so, we can define a new origin, that allows a small fraction of the multiply charged

particles deviation. The radius of the origin can be derived from a mathematical plane-distance formula.

$$r = \frac{\varepsilon C_{ext,calc}}{\sqrt{\sum_{k=i-x+1}^{i}(C_k - C_{ext,calc})^2}} \qquad (4.23)$$

Where r is the radius of the new origin and ε is the tolerance of error. Thus, Equation (4.23) is adjustable and in this work we consider 5% acceptance from multiply charged particles($\varepsilon = 0.05$). If the lines in Figure 4-4 cross the circle defined by the radius in Equation (4.23), the error of the measured and the theoretical cross section would be within 5 percent.

The size of the new origin does not depend on the measured cross section, but only the cross section of the multiply charged particles and the $C_{ext,calc}$. For 250nm, the size of the origin increases due to the $C_{ext,calc}$ (Figure 4-5). Again, caution should be taken when approaching the dangle area; in this case the distance to the origin does not change and the radius of the origin shrinks as more charges are considered. For example, considering *q4* and *q5*(light blue area, Figure 4-5) for 250nm increases the radius size. This implies that measuring the number concentration of *q4* and *q5* for 250nm would increase the accuracy of C_{ext} measurement. However, for 300nm even when *q5* is being considered, the radius shrinks. A shrinking radius increases the distance between the line to the new origin, while the distance represents the relative errors between $C_{ext,meas}$,and $C_{ext,calc}$. Notice that the size of the origin is not related to

the $C_{ext,meas}$, but depends on the fraction of multiply charges and the Mie theory extinction cross section. The shrinking radius implies that *q4* and *q5* for 300nm was not effectively decreasing the relative errors. To further decrease the relative errors between $C_{ext,meas}$,and $C_{ext,calc}$, the fraction of *q4* should be measured and *q6* may need to be considered in the $C_{ext,calc}$.

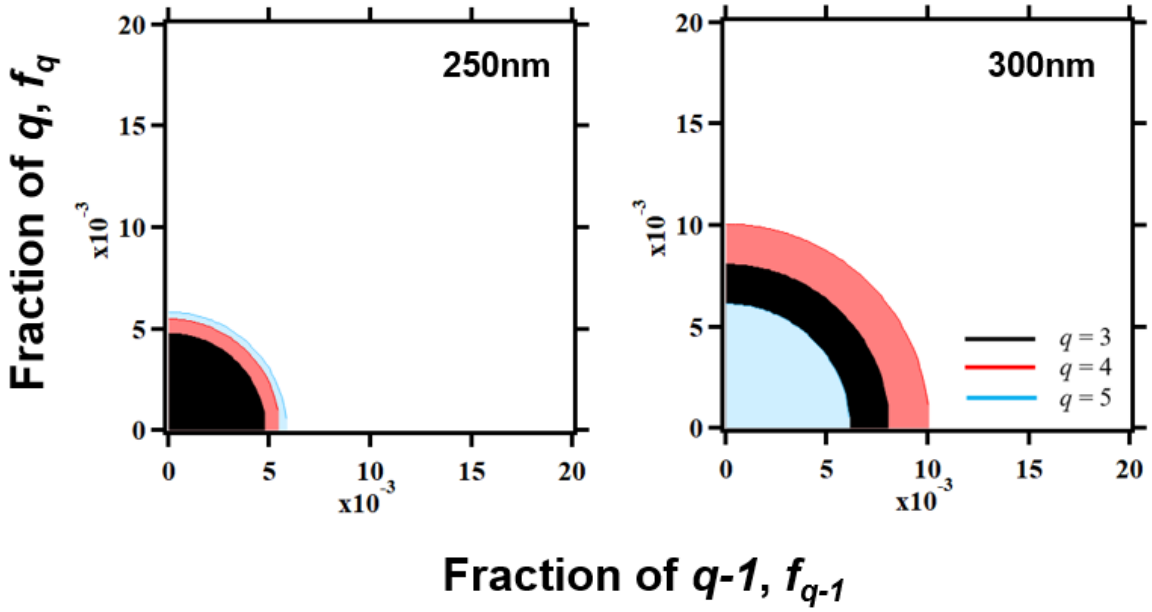

Figure 4-5: The circle shows the fraction combination where the 5% differences of the model cross section to the ensemble cross section is. Under most of the cases, radius of the circle is less than 2%, which also implies that the allowable fraction of the multiply charge particles is pretty small.

4.5 Summary and Future Work

The DMA-CRD is a common experimental set up for C_{ext} measurement and is inevitably affected by multiple charging problems. The number of multiple charges that should be considered can go beyond two; the number of multiple charges to be considered in C_{ext} measurements is determined by the Mie spectrum, which depends on the CRD wavelength, and particle refractive index. Generally, C_{ext} measurements are higher than C_{ext} values predicted with singly and doubly charged assumptions. Hence, one may consider including more multiply charged particles to decrease the underestimation in the C_{ext} prediction. However, the charging probability from Gunn's model predicted that the number concentration of these larger particles should be small. Currently, experimentally and practically, it is not possible to measure the entire number concentration and size of the particles in each different sample. The results from this paper suggest that the highest multiple charges that should be considered will be determined by the Mie theory Dangle area. In the Dangle area, C_{ext} does not increase monotonically with particle size. The contribution of higher (> +2) multiply charged particles in C_{ext} measurements gradually decrease when the size approaches to the dangle area (as seen by the slope of the lines in Figure 4-4 and Table 4-1). Installing an impactor can certainly decrease the error from the multiply charged particles. However, if the impactor cannot remove all the significant multiply charged particles, Equation (4.22) can predict a range of the fraction

of the multiply charged particles that cannot be measured. The equations presented here can quantify the extent (and relative error) to which the multiple charging assumption influences C_{ext}. In our analysis, we also show sensitivity of these errors in the form of a tolerance equation and tolerance figure (Figure 4-5.) It is noted that the tolerance also depends on the Mie spectrum, which is also a proof that considering higher charges in the dangle area is not an effective improvement when the radius of error shrinks. Understanding the sources of uncertainty, reducing multiple-charged errors, and improving the accuracy in C_{ext} measurement will help model contributions to the aerosol climatic effects.

Chapter 5: The Nano-plastics in Water

5.1 Background

The presence of plastic debris in environment is a rising concern (Andrady 2011; Koelmans, Besseling, and Shim 2015; da Costa et al. 2016a; Ter Halle et al. 2017; Allen et al. 2020). Plastic debris pose threats to marine animals and human health (Bilal et al. 2021; Haegerbaeumer et al. 2019). In a 2019 WHO technical report *"Microplastics in drinking-water"* , concentrations of micro-plastics, ranging up to 10^3 particles/L were detected in drinking water and natural waters.

Plastics found in the environment maybe derived from commonly used plastic sources. In 2019, the U.S. production volume of low density polyethylene (LDPE) and polyvinyl chloride (PVC) was 3.46 million metric tons and 7.2 million metric tons, respectively (Tiseo 2021). LDPE is commonly used in grocery bags, food wrap and bread bags (Raheem 2013) and PVC is used in cooking oil bottles, and for meat packaging. According to the PET Resin Association, the production volume of polyethylene terephthalate (PET) is 3.1 million metric tons annually in U.S. PET is used in beverage and mouthwash bottles and in boil bag pouches (Raheem 2013). Thus, these three plastics used in food and beverage packaging are often exposed to liquids at different temperatures. As a result, there is a potential for degraded micro

plastics and plastics of smaller sizes to shed from these materials.

It is widely believed that plastics may further degrade into nano-sizes (Koelmans, Besseling, and Shim 2015; da Costa et al. 2016a; Haegerbaeumer et al. 2019; Andrady 2011). However, people know little about the nano-plastics in the environment due to the limitation of identification techniques. Techniques that have detected the nano-plastic particles include Optical Traps (Gillibert et al. 2019), scanning electron microscopy (SEM) and transmission electron microscopy (TEM) (Gigault et al. 2016). The mass of the nano-plastics particles is small (around several μg) but their number concentration may be large. Nanoparticle tracking analysis (NTA) and Dynamic Light Scattering (DLS) has been used to count the number concentration of the nano-plastics (Filipe, Hawe, and Jiskoot 2010). These methods are usually combined with an additional instrument to identify the chemical composition, such as inductively coupled plasma mass spectrometry (Lai et al. 2021), Fourier Transform Infrared Spectroscopy (FTIR) (Zangmeister et al. 2022b) or gas chromatography−mass spectrometry (G. L. Sullivan et al. 2020).

Nano-plastics generated from commonly used products have been detected. Specifically, Yang et al. 2021 used NTA and SEM, TEM, scanning transmission X-ray micro-spectroscopy to study the generation of the nano-size fibers generated from the washing of clothes. Yang et al. 2021quantified nano-plastics with an average hydrodynamic diameter 173 nm –188 nm. Hernandez et al. 2017 found nano-plastic particles in facial scrubs that were ~ 24

± 6 nm to 52 ± 14 nm using SEM and FTIR techniques. Lambert and Wagner 2016 used NTA to measure the polystyrene coffee lid degradation and found nanoparticles (with average 224 nm diameter) increased their concentrations in water with time. Only recently, Zangmeister et al. 2022 used a Differential Mobility Analyzer (DMA) and Condensational Particle Counter (CPC) to measure nanoparticles generated from single-use food grade nylon bags and hot beverage cups lined with low density polyethylene. Nano-plastics particles from 30 nm to 80 nm were generated when hot water was poured in the LDPE liner cup. The aforementioned studies have tested and provided valuable information on the degradation of composite materials; the propensity of the pure plastic compounds to weather in the presence of water and generate nano-plastics is not well known.

In this study, we investigate the generation of nanoparticles from high purity materials to minimize contributions to nanoparticles from non-plastic sources. 5 common materials are selected and their nanoparticle generation at different temperatures, below the boiling point of water, is quantified. Three of the materials are widely used food packaging plastics- low density polyethylene (LDPE, powder form), polyvinyl chloride (PVC, powder form) and polyethylene terephthalate (PET, granular form). We compare nanoparticle generation from these materials to cellulose (representative of paper materials) and SiO_2 (glassware). The powders are mixed in water at different temperatures. Depending on the density of materials, large particles either float to the top (e.g. LDPE) or precipitate to the bottom (e.g. PVC and PET, cellulose, SiO_2).

The aqueous solution is then atomized and dried to produce nanoparticles (as described in Zangmeister et al. 2022). The nanoparticles are then imaged with electron microscopy techniques, and subsequently characterized for particle number and size concentration with *in situ* electrical mobility aerosol techniques. The *in situ* aerosol concentration maybe different than the particle concentration in solution. Thus, in addition we also develop a calibration method to estimate the particle number concentration of nanoparticles shed to the solution from the food packaging material. The method is applied to estimate the concentration of shed nanoparticles in solutions of varying temperature.

5.2 Experimental Methods

Dry nanoparticles were generated from atomized solutions of purified water and solid materials. 0.3g low density polyethylene (LDPE, Alfa Aesar), polyvinyl chloride (PVC, Sigma Aldrich, 99%+), SiO_2 (Sigma Aldrich, 99%+) and cellulose (Sigma Aldrich, 99%+) or 3 g of granular polyethylene terephthalate (PET, Sigma Aldrich, 99%+) were put into a 200mL of ultra-purified water (UPW) (Milipore® 18 MΩ cm) in separate Pyrex® glass bottles. Each bottle was placed in a hot water bath to control the heating temperature. The temperature was kept constant for one hour.

A Collison type atomizer was utilized to generate wet droplets (average diameter 300 nm)

from the UPW. The working of an atomizer was based on the Bernoulli principle. Compressed air with pressure difference ~10 psi to the atmosphere came through an orifice. A high velocity air jet was formed and liquid in turn was pulled through vertically from the bottle. Liquid was then atomized and become wet droplets. Large droplets were removed due to the impaction to the wall. Fine spray leaved from the top of the atomizer and were then dried via a silica gel dryer.

Aerosolized particles were deposited via a TEM precipitator on to a TEM grid. The grids were then analysed with a JEOL JEM 2100 Field Emission TEM/STEM at the University of Maryland, Nano Center. The TEM can image particles as small as 2 nm. For TEM measurements solutions in the atomizer were maintained at room temperature.

It should be noted that there is no consensus in the definition of “nano-plastics”. Plastic particles smaller than 1000 nano-meters are typically considered nano sized. (Yang, Luo, and Nowack 2021; Gigault et al. 2018). In this study, we use a DMA to identify the size of nanoparticles with less than 1000 nm electromobility diameters. Typically, an impactor is installed in front of the inlet of the DMA to remove larger particles. In this study, we use a 0.71 cm impactor with the cut-off diameter at 750 nm (Marple and Willeke 1976). As a result, the nanoparticles mentioned in this study are particles smaller than the limitation of the impactor cut-off diameter and well within the commonly defined nanoparticle range.

The particle number and size distribution between 14.6 nm to 661.2 nm was measured

by a DMA and a CPC in series. The DMA selected nanoparticles by their electrical mobility diameter (D_m). A Kr-85 neutralizer was used to charge the aerosols. A voltage difference was applied across the DMA rod and column. The charged particles were distributed across the column by electrical mobility. At the end of the column, there is a small slit to allow a small range of the mobility particles to pass through (Wang and Flagan 1990).

The number concentration of size selected particles is then counted with a condensation particle counter (CPC). In a butanol based CPC, nanoparticles are enlarged in a super-saturated butanol environment to be counted by the laser light scattering (Stolzenburg and McMurry 2007). The working principle of the CPC is similar to an optical particle counter. The enlarged droplets come into a laser viewing volume and scatter the light. A photodetector collects the light-pulses caused by the droplets. The light-pulse is then converted into electrical pulses and count the rate to calculate the number concentration. It is noted that the total particle concentration should be less than 5×10^5 particles/cm^3.

Details of Scanning Mobility Particle Sizer (SMPS) theory is described by Wang and Flagan 1990. Dry particles enter the DMA column and CPC counter with a flow rate of 5 cm^3 s^{-1}. The sheath to sample ratio is 10:1. The scanning time is 135 seconds for a single scan. This procedure was continuously operated for an hour.

5.3 Results and Discussion

5.3.1 Estimated Particles air concentration with the known PSL

Particles undergo dilution in air when nebulized and some may be lost in the instrumentation or measurement lines after particles are generated by nebulization. Thus, the measured *in-situ* aerosol number concentration of particles in air is likely less than the nanoparticle number concentration in solution. Therefore, it is necessary to calibrate this loss using inert nanoparticles of known concentration. Specifically, Lab 261® 250 nm and 223 nm polystyrene latex (PSL) particle solution of 10 mg solid content per ml (1.6×10^{12} PSL particles per mL) was diluted for calibration. 0.8 mL and 1.0 mL of the 250 nm PSL solution were diluted in 50 mL water. 223 nm PSL were used to make more diluted solution. 0.025 mL, 0.05 mL, 0.1 mL, 0.15 mL, 0.2 mL, 0.3 mL, 0.5 mL of the 223 nm PSL solution were diluted in 100 mL water. The number concentration was an average counted by CPC in 60 seconds. It should be noted that in this paper we did not measure the original number concentration of the 250 nm and 223 nm PSL particles in the solution. The original number concentration of 1.6×10^{12} PSL particles per mL is as estimate based on the known 1% mass concentration of solid content. We assume that all the solid content is mono-disperse spherical PSL. If the solution particle number concentration is known, the developed protocol can be applied as a calibration with $R^2 > 0.99$. Figure 5-1 shows an example of the estimation equation with R^2 coefficient > 0.99. The

estimation equation used here is a power law ($y = 3 \times 10^6 x^{1.114}$). The power-law fit does not have a negative y-intercept and avoids negative results when the air number concentration is close to zero. Each calibration is specific to the nebulization and aerosol measurement set-up. Any changes in tubing length, nebulization pressure may modify the calibration and thus daily calibrations were performed and applied to data sets to estimate particle concentrations in solution.

Figure 5-1 shows the loss of aerosolized particles is significant. The calibration is consistent with Zangemeister et al. 2022b. Zangmeister et al. 2022b also estimated the nano-plastics number concentration in the ultra-purified water. They measured the change of particle concentration by removing part of the experimental set-ups. Their highest nano-plastics concentration (food grade nylon @ 90 ºC) of estimation is 3.5 × 10^{13} L^{-1}, with the number concentration in air ~1.2 × 10^5 cm^{-3}. In Zangmeister et al. 2022b, the ratio between nano-plastics number concentration in water/in air is ~3 × 10^5 cm^3 mL^{-1}. In this work, our ratio is ~3×10^6 cm^3 mL^{-1} (Fig. 1). Since particle loss of DMA-CPC set up can range from 10^5~10^6 cm^3 mL^{-1}, a concentration process is necessary for the dilute solution.

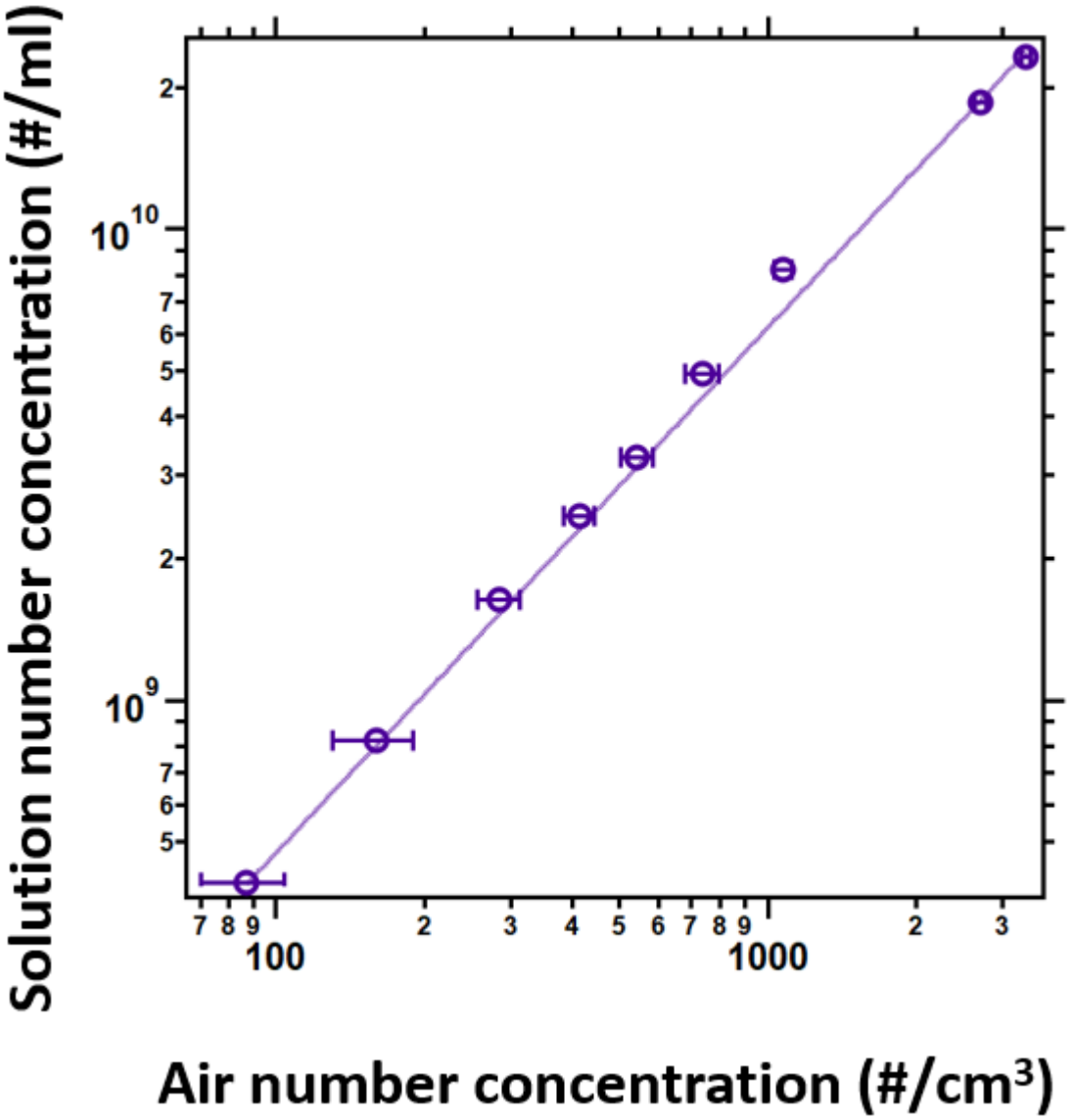

Figure 5-1: Exemplary estimation of PSL particles measured in air (particles/cm^3) and in the aqueous solution (particles/ml; open symbols). Error bars in the x-direction are the standard deviation of 1 minute measurements. The estimation equation (purple line) is: $y = 3 \times 10^6 x^{1.114}$ and the correlation coefficient, $R^2 > 0.99$.

5.3.2 Transmission electron microscopy (TEM) images of plastic particles

TEM images show and confirm that particles nebulized from solution generate in-situ particles in the air. Since we are working with known laboratory grade sources, the only source of measured particles are from the added compounds in solution. The particles generated from solution are distinctive of the solids in UPW.

Figure 5-2 shows the TEM images for nanoparticles generated by nebulizing solutions of LDPE, PVC and PET. The TEM images show particles increasing in size from left to right. Particles smaller than 50 nm appear compact and spherical. Larger particles (> 100 nm) form agglomerates and are irregular shaped.

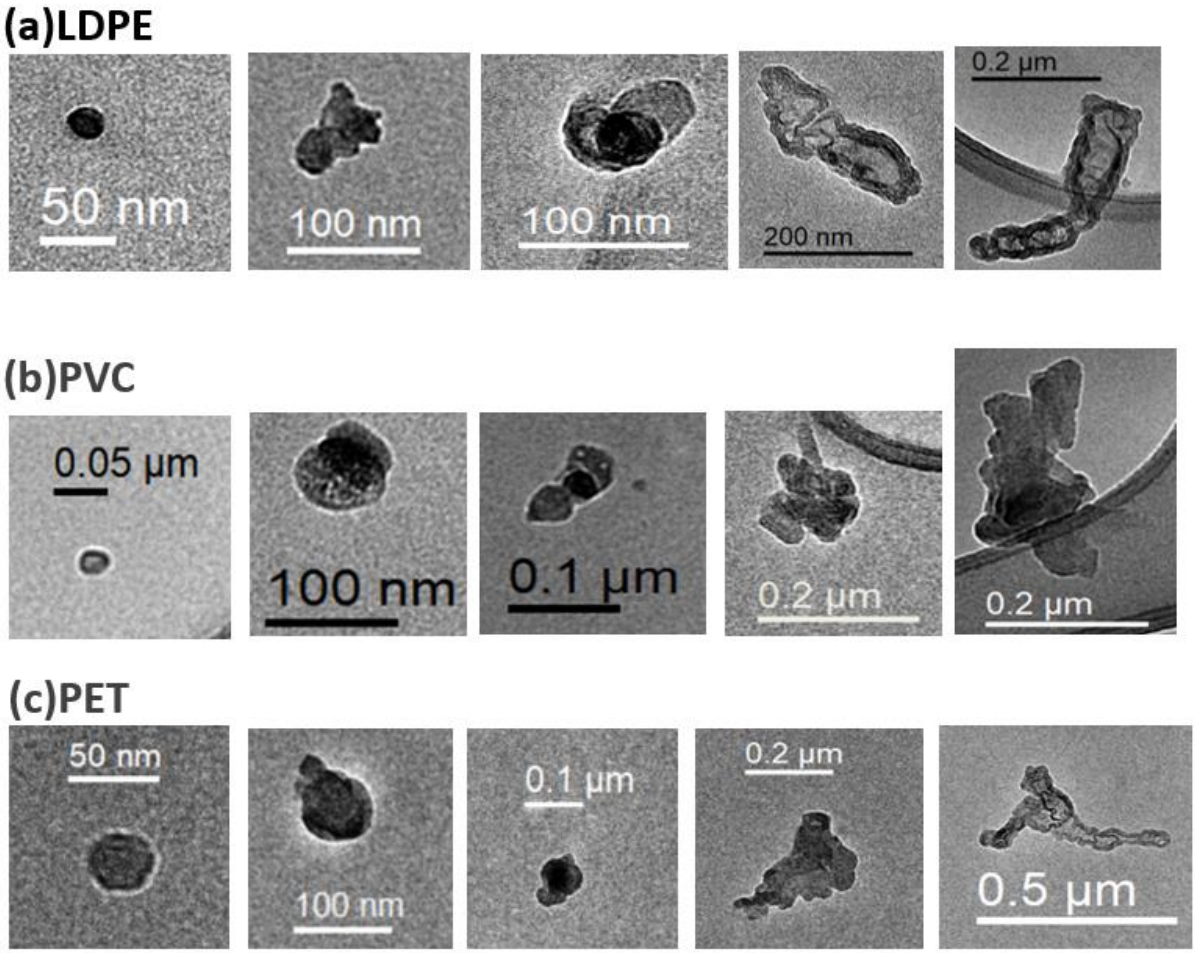

Figure 5-2: The TEM images of nano-plastics in the water. (a) LDPE (b) PVC (c) PET particles with different sizes were found. Particle aggregation occurs around 100 nm and 200 nm.

TEM results are consistent with published studies that show plastic degradation in the environment. Micro- and macro-plastic pieces in the environment can be physically weathered under shear stress, chemically oxidized, photo-oxidized, or bio-degraded and release smaller particles (Andrady 2011; Shah et al. 2008; Arp et al. 2021; Alimi et al. 2022; Gigault et al. 2016; Corcoran, Biesinger, and Grifi 2009; Julienne et al. 2022; Mohana et al. 2021). It should be noted that the source of the observed TEM nanoparticles may originate from either the

original manufacturing of solid powders or via the addition to UPW. The following sections will provide evidence that adding solids to UPW is a significant source.

5.3.3 Size distribution of plastics and the total number concentration in an hour

The electrical mobility size and number distribution of the nano-plastics before and after heating were measured with an SMPS. Figure 5-3 shows the size distribution of all five materials before and after 1 hour of heating at 60 ℃. Figure 5-3 is the raw data measured by DMA and CPC without background subtraction. It should be noted that the size distribution of particles shown in Figure 5-3 likely contains background nanoparticles from the ultrapure water system (Appendix Figure A.4.1). The sample of water is measured separately in a different bottle. As a result, we do not suggest comparing the size distribution directly. In Figure 5-3, since the solution is kept constant in the same bottle while heating, the additional particles generated from heating are from the added plastics in solution. In Figure 5-3 the size and the number concentration of LDPE increases significantly more after heating than PVC and PET. The peak mode of LDPE shifts from ~30 nm to 35 nm over an hour, which may indicate the occurrence of particle coagulation. In our controlled study, micro-plastics pieces were heated to temperatures less than the boiling point of water (100 ºC). The melting points of the plastics tested in this study are much greater than that of the boiling point of water; thus plastics are assumed to not easily degrade at moderately heated water temperatures. For example, the pyrolysis temperature of LDPE is 420-510°C (Seifali Abbas-Abadi et al. 2015). Hence an

increase in LDPE particle number after heating, corroborates that a possible mechanism of the nano-plastics generation is the shear stress caused by water when temperature increases (Mohana et al. 2021).

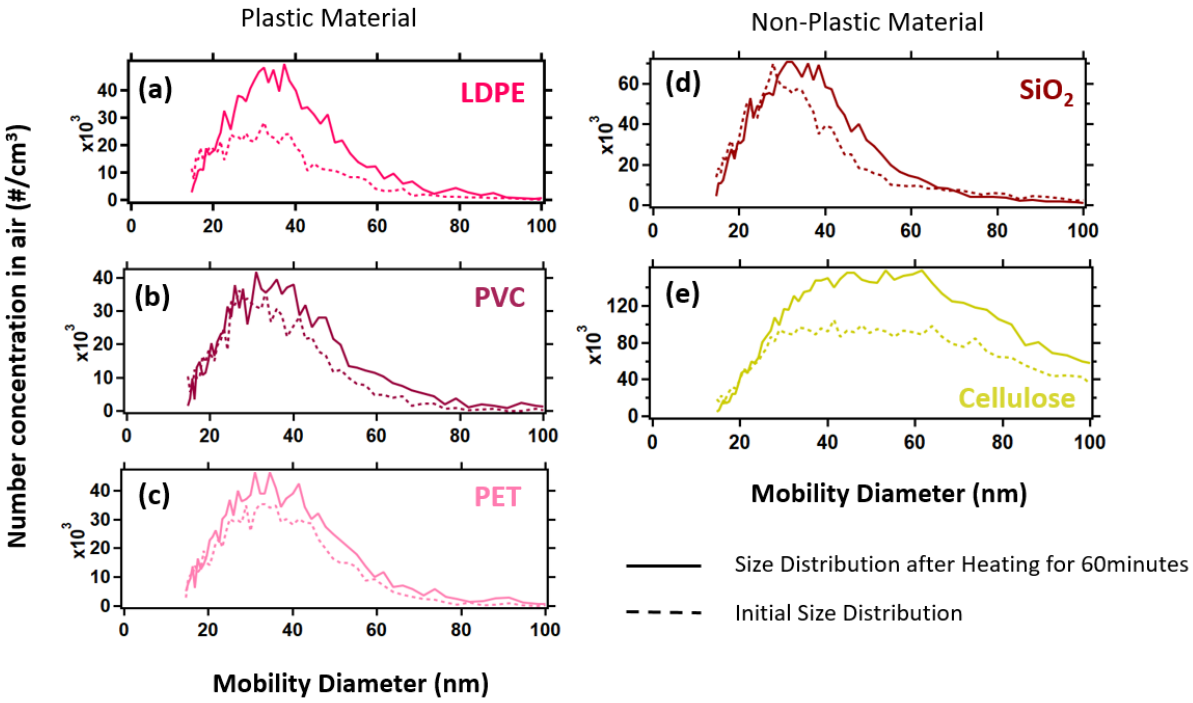

Figure 5-3: Size distribution comparison between the air number concentration before and after heating for 60 minutes at 60 ℃ of (a) LDPE (b) PVC (c) PET (d) SiO_2 and (e) cellulose. (a) The size and the total amount of LDPE increase after heating. (b) Although PVC is also powder, the size and the amount of the nanoparticles only slightly increase after heating. (c) In our study, granular PET were used. The size and the amount of nanoparticles also increase after heating for PET although the total surface area is not as much as the powder form materials. (d) The size and the amount of the SiO_2 (e) The total amount of cellulose increase the most among all five materials.

Figure 5-4 shows the particle number concentration in water heating as a function of time for 5 common materials. LDPE particle concentrations increase in the first 15 minutes. The total number concentration of PVC and PET also increase. For non-polymer material, the total number concentration of cellulose increase in the first 15 minutes and remain at high concentration (~ 6×10^{11} cm^{-3}). The number concentration of SiO_2 remains constant during heating.

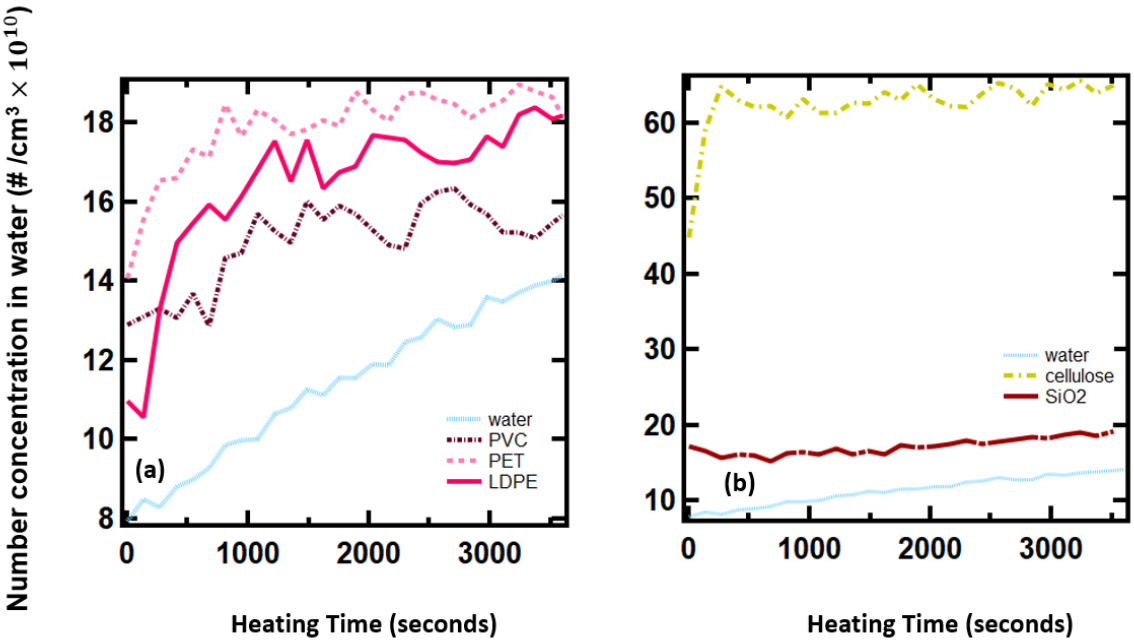

Figure 5-4: The total number concentration of (a) nano-plastics and (b) non-plastic materials heating at 60℃ for an hour.

The U.S Food and Drug Administration (FDA) regulates plastic emissions by mass and

not number. However, we can estimate the mass loss by integrating the number size density distribution. Table 5-1 shows both mass and number concentration of the nanoparticles before and after heating. Particles are assumed spherical with the measured electrical mobility diameters for this estimate. Mass concentration of the nanoparticles are small (on the order of ~ 10^{-6} g cm^{-3}) but the total number concentration reaches 3×10^{10} cm^{-3}~22×10^{10} cm^{-3}. In other words, the mass loss of the plastic nanoparticles will be difficult to measure and quantify. For LDPE that shed the most nanoparticles of the five materials, nanoparticles were only 0.07% by mass, a seemingly negligible amount. Consequently, it may more significant to quantify nanoparticles found in aquatic environments and drinking water by number rather than mass.

Table 5-1: Total mass and number concentration of nanoparticles before and after heating at 60 ℃ for an hour.

	LDPE	PVC	PET	Cellulose	SiO_2
Density (g cm^{-3})	0.92	1.38	1.38	1.5	2.65
Initial Number Concentration ($\times 10^{10}$ cm^{-3})	2.99	4.45	5.18	21.7	4.67
Number concentration after heated ($\times 10^{10}$ cm^{-3})	5.64	4.00	6.43	22.0	3.30
Initial Mass Concentration ($\times 10^{-6}$g cm^{-3})	0.55	1.27	1.52	27.6	2.43
Mass concentration after heated ($\times 10^{-6}$g cm^{-3})	1.07	1.48	2.52	28.1	2.64

5.3.4 Temperature Effects on Nanoparticle Generation

Figure 5-5 shows the total number concentration of nanoparticles generated at temperatures ranging from 25 ℃ to 90 ℃. The number concentration of the nanoparticles in the water increases with the temperature. The relation between nanoparticles and temperature is complicated. Increasing the temperature may also encourage the kinetics of nanoparticles aggregation, and cause the total number concentration of nanoparticles decrease. (see Figure

5-4 for LDPE and SiO_2 at 90℃)

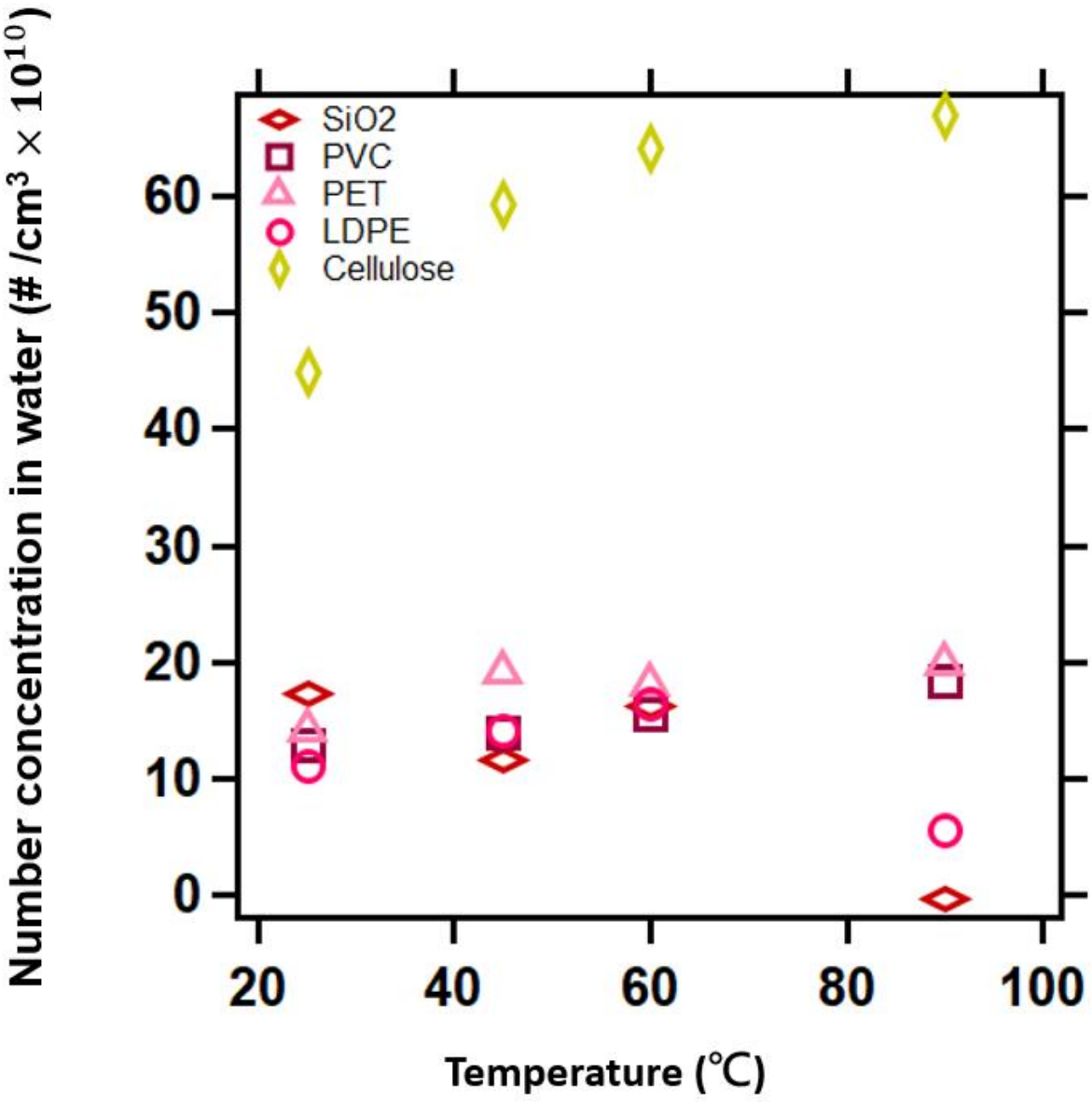

Figure 5-5: Total number concentration of the five materials heating for 30 minutes under different temperature. Nano particles for cellulose increase with the temperature. For plastics, the total amount concentration increase after 40 ℃. After 40 ℃ nanoparticles start to aggregate. As a result, the total number concentration may decrease as the temperature increase.

5.4 Summary and Future Work

In this study, we measured the nanoparticles size distribution of 5 materials that are used in daily food packaging. Three of the materials are plastics (LDPE, PVC and PET), while the other non-plastics materials, cellulose and SiO_2, are components of paper and glass materials. We aerosolized the nano-plastics in the ultra purified water solution and deposited the particles for TEM imaging. TEM images visualized the generation of nano-sized particles with distinct sizes and shapes, distinct for each plastic material. The images provided evidence that nano-material was present in the not heated ultra purified water solution. Nanoparticles were generated after heating the atomizer solution at 60 ℃ for 1 hour. Both the size and amount of LDPE and cellulose particles increased after heating. In Figure 5-2 and Figure 5-3, the number concentration of nano- PVC, PET and SiO_2 did not grow. Both LDPE and cellulose (paper) are common materials used in food packaging materials. For example, plastic straws are now banned in Seattle, California, and countries like United Kingdom and Taiwan. Paper straws have replaced the traditional plastic straw as cellulose is considered a bio-degradable and sustainable material. However, the results here indicate that cellulose could generate more nanoparticles than the plastics materials. Due to the durability of the plastics in the environment, new materials are created to be bio-degradable or easily break. However, materials that can easily degrade may generate more nanoparticles under mild temperatures. In the future, new

food related materials should be bio-degradable in the environment and should also be developed to shed fewer nanoparticles in the aqueous environment. The consideration of particle number versus particle mass for the toxicology of nano-plastics in the environments should further be considered in the use and development of new materials.

Chapter 6: The Hygroscopicity of Nano-plastics

6.1 Background

Micro-plastic particles identified in aquatic (Andrady 2011) and atmospheric systems (Prata 2018) have raised concerns. Recent work has explored the biological impacts of these anthropogenic particles on living things. Haegerbaeumer et al. reviewed the effects of plastic particles on small aquatic organisms. Micro- (and potentially smaller) plastics were found in benthic fauna digestive systems (Haegerbaeumer et al. 2019). Furthermore nano- and larger plastic debris can affect the food chain by impact creatures health via bioaccumulation (Ma et al. 2016; Sökmen et al. 2020). In 2018, Prata raised the concerns that small hydrophobic airborne nano- particles could cross the blood brain barrier (Prata 2018). In the same study, micro-plastics particles were found in the respiratory system of humans resulting in inflammation and cytotoxicity.

Micro-plastics in the atmosphere were found in road dust, waste water treatment plant and in door environments (Batool et al. 2022). While number concentration of micro- and nano-plastics depends on their location and human activity, micro- and nano-plastic particles also have been found in remote areas, such as the Antarctic (Munari et al. 2017), the Arctic (Cózar et al. 2017), New Zealand (Fan et al. 2022) and Pyrenees Mountains (Allen et al. 2019). This

suggesting that micro- and nano-plastics have a potential to travel in the atmosphere. Allen et al sampled air masses and found that micro plastic particles could travel as far as 95 km (Allen et al. 2019). It has been hypothesized that plastic particles entered the atmosphere from aerosolized sea spray (Lehmann et al. 2021; Allen et al. 2020), were subsequently transported to cold areas, and then precipitated as either droplets or snow to the earth's surface. Micro- and nano-plastics have been found in fresh snow (Bergmann et al. 2019), thus providing evidence to the theory of long range atmospheric transport. Plastic particles can act as both cloud and ice condensation nuclei (Aeschlimann et al. 2022b). As a result, wet deposition is a likely route for plastic removal in the atmosphere. However, the mechanisms by which plastics act as warm and cold cloud seeds are not well understood. Furthermore, the intrinsic ability to uptake water, hygroscopicity, of airborne plastic particles will help determine a particle's fate and transport in atmospheric and aquatic environments.

Micro- and nano-plastics can be difficult to characterize, especially when the sizes of plastics are in the nanometer size range. Techniques to study nano-plastic particles include Optical Traps (Gillibert et al. 2019), nanoparticle tracking analysis (NTA) (Filipe, Hawe, and Jiskoot 2010), and dynamic light scattering (DLS). The aforementioned particle methods can be combined with additional instrumentation to identify the chemical composition, such as inductively coupled plasma mass spectrometry (Lai et al. 2021), Fourier-transform infrared

spectroscopy (FTIR) (Zangmeister et al. 2022b) or gas chromatography−mass spectrometry. Gillibert et al. 2019 used Raman tweezers to analyze the size and the morphology of nylon small plastic particles and polypropylene small plastic particles in sea water. Ter Halle et al. 2017 found plastic debris smaller than 1000nm in North Atlantic subtropical gyre using DLS, but an accurate size distribution was hard to obtain. Notably, these techniques identified plastic particles in aqueous solutions. Additionally, plastic particles can also be aerosolized and counted in air (Zangmeister et al. 2022a). In 2022, Zangmeister et al. used a differential mobility analyzer (DMA) with a condensation particle counter (CPC) in series and show a full size distribution of the nano-plastics released into hot water from single-used consumer product. The combination of a DMA with a CPC can effectively detect the existence of the nanoparticles and measure the sizes of nanoparticles.

In the atmosphere, nano-plastics may provide a surface for water vapor to condense. Large (~10^{-6} m) particles can provide sufficient surface area but are prone to gravitational settling (Williams et al. 2002). Nano-scale particles have longer atmospheric lifetimes and their ability to form droplets, act as cloud condensation or ice nuclei is determined by both particle size and chemistry. To our knowledge, no other work has measured the droplet forming potential of commonly used plastic materials. In this work, we employ widely used aerosol measurement techniques to measure the size distribution and droplet forming ability of nano-

plastics. Specifically, a DMA and CPC is simultaneously connected to a cloud condensation nuclei counter (CCNC) and measures CCN activity of the nano-plastics exposed to constant relative humidity. The hygroscopicity of three plastics - low density polyethylene (LDPE), polyvinyl chloride (PVC), and polyethylene terephthalate (PET), are estimated. LDPE, PVC and PET contain polymeric carbon chains and all three are considered hydrophobic compounds (McCall et al. 1984; Karim et al. 2022; Maláč, Altmann, and Zelinger 1970). The hygroscopicity of cellulose, a main component of paper products, is also measured and reported for comparison. Subsequently, we test two hygroscopicity models, Flory-Huggins-Köhler (FHK) (C. N. Mao, Malek, and Asa-Awuku 2021) and Frenkel-Halsey-Hill adsorption theory (FHH-AT) (C.-N. Mao, Gohil, and Asa-Awuku 2022), to describe the water-uptake ability of the nano-plastics and cellulose. A single hygroscopicity value is reported for all compounds and the implications of these measurements are then briefly discussed.

FHK can be applied to water-soluble polymer and only requires a one fitting parameter. FHH-AT is an adsorption model that utilized two fitting parameters. The hygroscopicity of nano-plastics determine whether these plastics particles rain down to the surface or not.

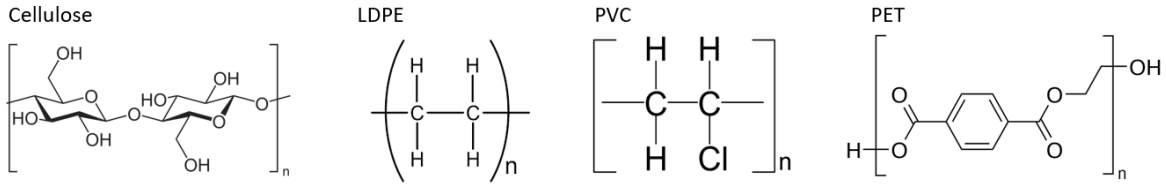

Figure 6-1: The chemical structure of nanoparticles cellulose, LDPE, PVC and PET.

6.2 Experimental Methods

Dry nanoparticles were generated from atomized suspensions. 0.3 g of low density polyethylene (LDPE, Alfa Aesar), polyvinyl chloride (PVC, Sigma Aldrich, 99%+), and cellulose (Sigma Aldrich, 99%+) or 3 g of granular polyethylene terephthalate (PET, Sigma Aldrich, 99%+) were placed into 200 mL of ultra-purified water (UPW) (Millipore® 18.2 MΩ cm) in separate Pyrex® glass bottles. A Collison type atomizer then generated wet droplets and the wet particles were dried via a silica dryer. The dry polydisperse ultrafine aerosols are then sampled at 0.8 liter per minute with a scanning mobility particle sizer (SMPS) (Wang and Flagan 1990). The SMPS consists of a neutralizer, DMA and CPC. The DMA size selects the polydispersed dry aerosols by electrical mobility and produces mono-dispersed aerosol. The monodisperse aerosol were then split into the CPC and Cloud Condensation Nuclei Counter (Roberts and Nenes 2005) with flowrate 0.5 liters per minute and the with flowrate 0.3 liters per minute to analyze the CCN activity. The total particle concentration (CN) is counted by the CPC and the concentration of particles that form droplets at a selected size and constant supersaturation (CCNN) is counted by the CCNC. The ratio of the CCNN to CN is computed with Scanning Mobility CCN Analysis Method (SMCA) (Moore, Nenes, and Medina 2010) and a critical diameter (D_c) is computed for a constant supersaturation. For a given constant supersaturation, s, and compound, the experiment was repeated four times. By measuring the

CCNN/CN ratio at several different supersaturations, supersaturation and activation dry diameter (s-D_c) data was obtained. The supersaturation was then varied from 0.3% to 1.5%. (s-D_c) measurements are then required to calculate nanoparticle hygroscopicity.

Aerosol hygroscopicity can be measured and reported via the representation of a single hygroscopicity parameter, κ. Briefly described here, the κ of aerosols found in the atmosphere can vary from 0 to 1.4. Inorganic salts, like ammonium sulfate, are known to be hygroscopic with measured and predicted κ=0.604. (Tang et al. 2019; M. D. Petters and Kreidenweis 2007; Kreidenweis and Asa-Awuku 2013) Wettable but hydrophobic species, such as graphitic soot and high molecular weight hydrophobic polymers, are assumed to have κ=0. Simple and ideal assumptions are known to reproduce the droplet growth hygroscopicity of water-soluble and inorganic compounds.

Recently, two models have been developed to calculate the hygroscopicity of polymeric and water-insoluble particles. The FHK-hygroscopicity is aptly applied to water-soluble polymer and FHH-AT-hygroscopicity has been applied to water-insoluble polymer (C. N. Mao, Malek, and Asa-Awuku 2021; C.-N. Mao, Gohil, and Asa-Awuku 2022). FHK uses one fitting parameter and was incorporated into a single-parameter hygroscopicity term that describes the water-uptake of water-soluble aerosol. FHK has been shown to aptly reproduce the hygroscopicity of biodegradable hydrophilic polymeric aerosol, like PEG, and gelatin (C. N. Mao, Malek, and Asa-Awuku 2021). The FHK-hygroscopicity (κ_{FHK}) was developed by Mao

et al. (C. N. Mao, Malek, and Asa-Awuku 2021) and is briefly described as follows:

$$\kappa_{FHK} = \frac{1-\varphi}{\varphi}\left[-1 + \frac{1}{(1-\varphi)\,exp[(1-F)\varphi+\chi\varphi^2]}\right] \quad (6.1)$$

where φ is the volume fraction of the polymer, F is the reciprocal of the chain segments of the polymer equal to the ratio of the molecular volume of water and the solute and χ is the Flory-Huggins interaction parameter. χ describes the water affinity of the polymer and is the fitted from the *s*-D_c data in Figure 6-2. In Flory-Huggins theory, the polymer dissolves in water and water is considered a good solvent if χ is smaller than 0.5. Theoretical hygroscopicity is developed by assuming the activation occurs at the maximum of Köhler curve. Hence the hygroscopicity is only a function of dry diameter. Additional details of the κ_{FHK} can be found in Mao et al (C. N. Mao, Malek, and Asa-Awuku 2021).

FHH-AT assumes the solute is water-insoluble. However, water may adsorb on the particle surface. FHH-AT determines droplet growth using 2 empirical parameters, A_{FHH} and B_{FHH} (Sorjamaa and Laaksonen 2007b). The parameter A_{FHH} is related to the interaction of the first layer of water and the particle surface. The B_{FHH} represents the interaction between other layers of water molecules and the particles (Sorjamaa and Laaksonen 2007b; Kumar, Nenes, and Sokolik 2009). The FHH-AT-hygroscopicity (κ_{FHH}) was developed by Mao et al (C.-N. Mao, Gohil, and Asa-Awuku 2022) and described as follow:

$$\kappa_{FHH,exp} = f\left(D_d, D_{p,c}\right) = \frac{6\theta D_w}{D_d}\left(\frac{1}{\exp\left(-A_{FHH}\theta^{-B_{FHH}}\right)} - 1\right) \quad (6.2)$$

$$\kappa_{FHH,the} = f(D_d) = \frac{6D_w}{D_d} A_{FHH}\theta_c{}^{-B_{FHH}+1} \quad (6.3)$$

Where $D_d, D_{p,c}$ are the dry and wet diameters respectively. θ is the surface coverage, and describes the layers of water molecules adsorbed on to the dry particle surface (Sorjamaa and Laaksonen 2007a). D_w is the diameter of a single water molecule and equals to 0.275 nm. A_{FHH} and B_{FHH} are compound specific empirical parameters. The two empirical parameters are fitted from the *s*-D_c data (Figure 6-2). $\kappa_{FHH,the}$ is size dependent and decreases with the increasing particle sizes.

Nano-plastics are considered hydrophobic polymers. We convert the *s*-D_c data into FHK-hygroscopicity (C. N. Mao, Malek, and Asa-Awuku 2021) and FHH-AT-hygroscopicity (C.-N. Mao, Gohil, and Asa-Awuku 2022) and compare calculations to experimental data so that future work may incorporate the best hygroscopicity model for wet deposition prediction.

6.3 Results and Discussion

6.3.1 The cloud condensation activity (*s*-D_c diagram)

Nano-plastics provide surfaces for water to condense and can act as cloud condensation nuclei under supersaturation condition. Figure 6-2 shows the *s*-D_c of LDPE, PVC, PET and cellulose. The lines in Figure 6-2 are prediction from traditional Köhler theory with different hygroscopicity. These lines in a *lnS*-*ln D* diagram will all have the same slope of -1.5 according to the traditional Köhler theory (Seinfeld, Pandis, and Noone 1998). The red line is

the prediction for ammonium sulfate. The black solid line is for polymer with molecular weight near 100,000 g mol^{-1} and unity density. The dashed black line is the traditional Köhler for $\kappa = 0.05$. In Figure 6-2, nano-plastic particles (LDPE, PET and PVC) smaller than 100 nm activate and grow into droplets when supersaturation is over 0.3%. The three plastics are less hygroscopic than ammonium sulfate (the solid red line) but more hygroscopic than the traditional prediction for polymers (the solid black line). They have similar CCN activity as a sparingly water-soluble organic with $\kappa = 0.05$ (The dashed black line). However, the activation dry diameter of cellulose particles is larger under the same supersaturation. Cellulose is a natural polymer that is found in the cell walls and is the most abundant organic polymer on Earth (Medronho et al. 2012). Airborne cellulose (100 nm to 400 nm) were also found in the environment, and an average number concentration was 7.9×10^{-8} g m^{-3} in winter season of Vienna (Puxbaum and Tenze-Kunit 2003). Cellulose is hydrophilic (see Figure 6-1), but does not dissolve in water. As aforementioned, LDPE, PVC and PET are all considered hydrophobic compounds (McCall et al. 1984; Karim et al. 2022; Maláč, Altmann, and Zelinger 1970). In Figure 6-2, cellulose activates at larger sizes comparing to the hydrophobically-classified plastics at the same constant supersaturation. However, the anthropogenic plastic nanoparticles are more hygroscopic than the natural polymer cellulose when exposed to water vapor.

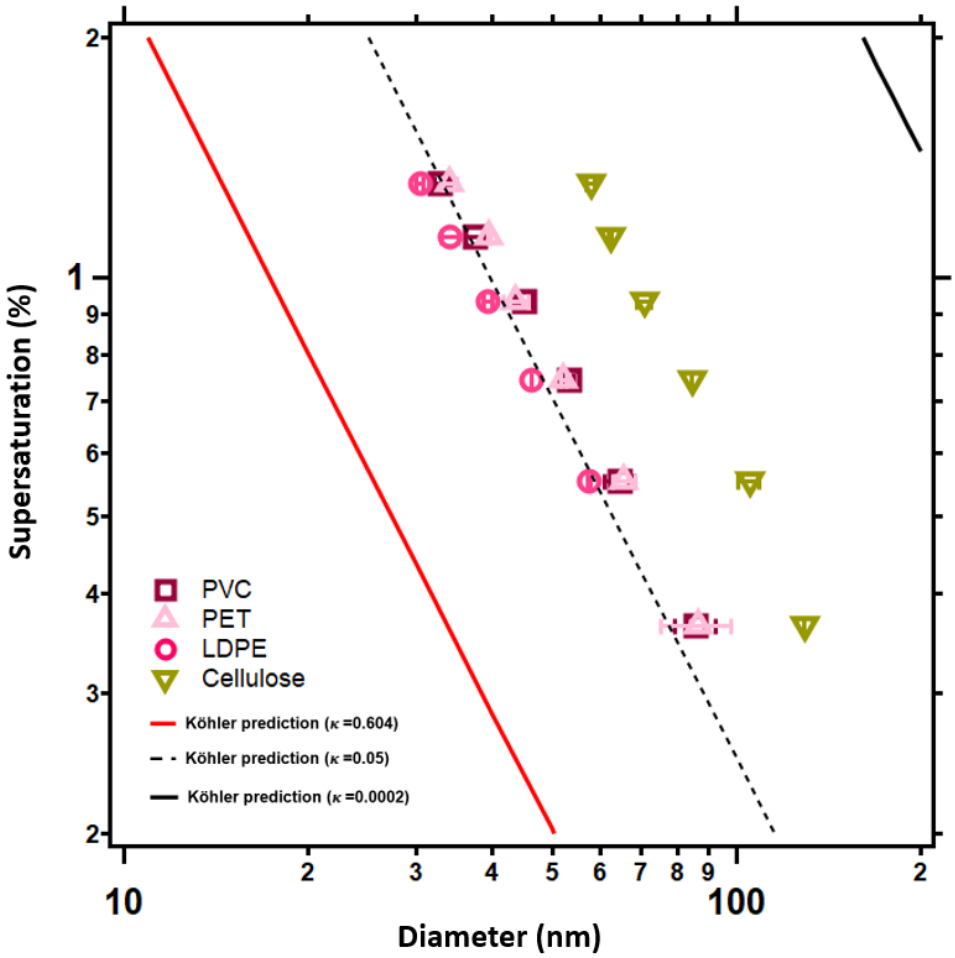

Figure 6-2: The CCN activation of PVC, PET, LDPE and cellulose. The solid lines are the traditional Köhler predictions. The solid red line is representative of inorganic ammonium sulfate with $\kappa = 0.604$ (M. D. Petters and Kreidenweis 2007; Kreidenweis and Asa-Awuku 2013). The solid black line ($\kappa = 0.0002$) is the CCN activity prediction of a polymer with molecular weight of 100,000 g mol^{-1}. The dashed line shows solute of constant hygroscopicity, $\kappa = 0.05$. The CCN activity of LDPE, PET and PVC is consistent with a wettable and slightly hygroscopic organic material with $\kappa \sim 0.05$ and noticeably more hygroscopic than measured cellulose particles or the predicted polymeric material (solid black line).

6.3.2 The hygroscopicity of nano-plastics

Two models of hygroscopicity are applied to the *s*-D_c data. Theoretically, the intrinsic hygroscopicity for polymers with an infinitely large molecular weight is zero. Traditional hygroscopicity assumes a thermodynamically ideal solution. The traditional hygroscopicity is the ratio of molecular volume of the solute and water molecules (see Equation 1.6) (R. C. Sullivan et al. 2009). Figure 6-2 shows that the experimental data do not agree with the hygroscopicity prediction of large-molecular weight polymers and thus the role of molecular weight can be considered insignificant for polymer hygroscopicity. The water affinity is more important and can be measured by experimental parametrization (Markus D. Petters et al. 2006).

Table 6-1 shows the empirical fitting χ of LDPE, PET, PVC and cellulose. In the Flory-Huggins theory, χ is the water-polymer interaction parameter. A χ lower than 0.5 indicates that the polymer attracts water molecules, and dissolves in water. If a polymer material has a χ below 0.5, it is considered soluble in bulk phase (Flory 1942). Plastics are assumed to be hydrophobic and effectively water insoluble. If the behavior of nano-plastics is the same as their bulk property, then they should not dissolve in water. We show the fitting parameter χ of the nano-plastics to demonstrate their water affinity. In Table 6-1, all the χ of the nano-plastics are negative and smaller than 0.5. Here the negative χ for all three plastics shows they can be moderately hygroscopic and act as cloud condensation nuclei under supersaturated conditions. The fitted χ for cellulose is 0.14. Consequently, the κ_{FHK} of

LDPE, PET and PVC are higher than cellulose. Cellulose is also effectively water-insoluble (Medronho et al. 2012). Cellulose is relatively less hygroscopic and the fitted χ is larger than 0 (see Table 6-1).

Figure 6-3 (b) shows the FHK-hygroscopicity of LDPE, PET, PVC and cellulose. Empirical hygroscopicities are calculated from *s*-D_c data, and hence are a function of both wet and dry diameters. κ_{FHK} is a model that developed for water soluble polymer. However, the κ_{FHK} for LDPE, PVC, PET, and cellulose can still be parametrized. The κ_{FHK} value of LDPE, PVC and PET are larger than 0.1 in Figure 6-3 (b). Among all three plastics, LDPE is the more hygroscopic than PVC and PET.

Figure 6-3 (a) shows the FHH-AT-hygroscopicity of LDPE, PET, PVC and cellulose. Table 6-1 shows the empirical fitting A_{FHH} and B_{FHH} of LDPE, PET, PVC and cellulose. In this work, LDPE, PET, PVC and cellulose are all completely insoluble in water (McCall et al. 1984; Karim et al. 2022; Maláč, Altmann, and Zelinger 1970; Medronho et al. 2012) but have the ability for water to condense. FHK is a model with only one degree of freedom, while FHH-AT is a model with two degree of freedom. Comparing Figure 6-3 (a) and (b), κ_{FHK} of plastics are a little bit larger than κ_{FHH}. κ_{FHK} of LDPE, PVC and PET are range from 0.1~0.4. κ_{FHH} of LDPE, PVC and PET ranges from 0.04 to 0.1. However the fitting of κ_{FHH} is better than κ_{FHK}. In Figure 6-3 (a), the R^2 of κ_{FHH} are all > 0.99 for LDPE, PVC, PET and cellulose. In Figure 6-3 (b), the R^2 of κ_{FHK} are 0.95, 0.91, 0.85 and 0.76 for LDPE, PVC, PET and cellulose

respectively.

In Table 6-1, we also show the density of the LDPE, PVC, PET and cellulose. Considering a spherical particle with the same volume, a plastic particle like LDPE, PVC and PET can potentially travel to further places than a cellulose particle since they have a smaller density. Interestingly, the hygroscopicity of LDPE, PVC and PET are higher than cellulose. This is an evidence of plastic particles can transfer to area far from human activity, and then deposit when the environment temperature drops or relative humidity increases.

Table 6-1: The fitting parameters of LDPE, PET, PET and cellulose

	cellulose	PET	PVC	LDPE
Density ($g\ cm^{-3}$)	1.5	1.38	1.38	0.92
χ	0.14	-11	-10	-34
A_{FHH}	0.13	0.44	0.58	0.53
B_{FHH}	0.6	0.78	0.84	0.8

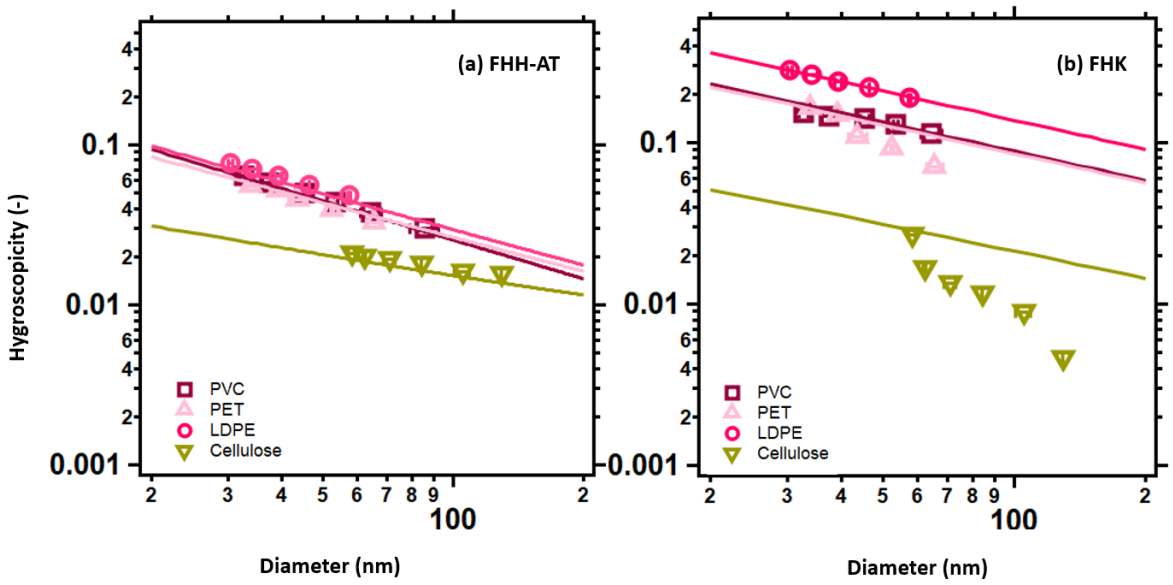

Figure 6-3: The κ_{FHH} and κ_{FHK} of LDPE, PET, PVC and cellulose.

6.4 Summary and Future Work

In this work we measure the CCN activity and estimate the hygroscopicity of three anthropogenic nanoparticles – LDPE, PVC and PET. The CCN activity and the hygroscopicity are compared with a natural polymer, cellulose. Cellulose is the main materials of paper. Traditional Köhler theory predicts a zero hygroscopicity for both polymer and insoluble particles. However, in this study we show that water-insoluble nano-plastic particles are more hygroscopic than if estimated using traditional droplet activation theory. The plastics are also more hygroscopic than cellulose. Plastics are more hygroscopic than paper materials, hence they potentially travel to the remote cold areas like Antarctic (Munari et al. 2017) and Arctic (Cózar et al. 2017). This work shows that nano-plastics have the propensity to act as cloud

condensation nuclei. Furthermore, FHH-AT theory suggests that water may adsorb on these particles in supersaturated phases. Adsorbed water on particle surfaces will likely provide a route for ice particles immersion freezing mechanisms. In this work, two models, the FHK and FHH-AT, are used to predict the hygroscopicity of nano-plastics. It should be noted that FHK is usually applied to soluble polymer. Plastics are considered hydrophobic, but can be very hygroscopic when they are in nano-sizes. In this work we used the fitting parameter χ in FHK models to demonstrate how hygroscopic plastics are. FHH-AT can be applied to the insoluble polymers. Although the two models should be applied to particles with different solubility, both theories predict a non-zero hygroscopicity of the anthropogenic particles. The hygroscopic behavior is evidence that wet deposition is a plausible and significant route of nano-plastics to the earth surface. In the future study, the developed hygroscopicity model can also be used to estimate the lifetime and transport of nano-plastics in the atmosphere, and be applied to the climate model to reduced the uncertainties from indirect effect as well.

Chapter 7: Summary and Future Work

There are increasing concerns about the environmental impacts of plastics. Plastics are relatively modern materials compared to clays, glasses and papers. The history of plastics dates back to the 19th century, when the first synthetic plastic was created (Geyer, Jambeck, and Law 2017). Nowadays plastics have been mass produced and are almost inevitable in the human daily life. Plastics pieces in the environment may degrade into micro- or nano-particles through physical, chemical or biological process (Andrady 2011). They interact with water, and potentially affect both of human health and environment. Field studies show that plastic particles are found in the areas far from human activity (Kelly et al. 2020; Cózar et al. 2017; Allen et al. 2019), but we do not know how plastics travel and deposit. There is little known research of plastic particle properties such as hygroscopicity. In this thesis work, we measured the hygroscopicity of nano-plastics using aerosol instrumentation. Hygroscopicity models were developed to understand particle-water interaction behavior in the aquatic, atmospheric and even human respiratory systems. The developed hygroscopicity models can be applied to other substances as well that have similar properties to the plastics, and thus may contribute to field of drug delivery and atmospheric science.

In Chapter 2 and 3, we developed hygroscopicity models for polymers and insoluble particles. We showed that water affinity dominates the droplet formation for both polymer and

insoluble particles as CCN. The water affinity has been found to be crucial and can only be parametrized by doing lab experiments. Traditional hygroscopicity model provided an estimation of their water affinity, but was not accurate (C. N. Mao, Malek, and Asa-Awuku 2021; C.-N. Mao, Gohil, and Asa-Awuku 2022). When applying the traditional hygroscopicity model to polymers or insoluble particles, experimental data and theoretical prediction did not agree with each other. The theoretical traditional hygroscopicity predicted a non-hygroscopic behavior for polymeric compounds, but in reality the particles still took up water and grew into droplets. However, droplet growth models usually have fitting parameters acquired via experimental data. As a result, accurate lab scale measurement is important, and mitigating the instrumentation errors helps us better understanding the water interaction of the CCN.

The DMA and CPC are commonly used instruments in aerosols studies, both in lab and field. In Chapter 4, we demonstrated that the multiple charging error in the DMA can cause large deviation in extinction cross section measurements. A small fraction of multiply charged, large particles can cause over 5% deviation from the theoretical prediction. It should be noted that multiple charging error deviates the results from the theoretical value when the particle property positively increases with the particle sizes. In this thesis, the nano-plastics measured in our experiments are smaller than 50nm (see Figure 5-3). Particles smaller than 50nm typically bring 0 or only one charge (Wiedensohler 1988). As a result, the multiple charging

errors were negligible for nano-plastics in this thesis. The techniques and knowledge developed in Chapters 2, 3, and 4 were then applied to the nano-plastics studies. We demonstrated the applications of models in Chapter 5 and 6.

In Chapter 5, we measured the size distribution of nano-plastics using DMA and CPC. Nano-plastics in the water can be aerosolized, and detected by the aerosol instrumentation. Nano-plastics were diluted when aerosolized. Concentrated number concentration of nano-plastics in water was necessary when using the aerosol instrumentation measurements. We used PSL as an example compound and convert concentrations measured by aerosolization to concentration in liquid solution. It should be noted that the nano-plastics concentration in aquatic environments may be lower than the solution sample made in the lab. Furthermore, environmental samples are complex and could contain other solid non-plastic materials in solution. As a result, future studies should develop a pre-concentration process for measuring nanoparticles in environmental samples to exploit the nebulization technique. The work in this thesis is a first step as we only focus on pure, lab based samples. Instrumentation to identify the particle chemical composition like FTIR or GC-MS may also be necessary for environmental samples.

In Chapter 6, we measured the hygroscopicity of nano-plastics, and compared them to a natural polymer, cellulose. The hygroscopicity models developed in Chapter 2 and 3 are applied in Chapter 6. Plastics (LDPE, PET and PVC) are found to be more hygroscopic than cellulose.

Nano-plastics can also act as CCN under supersaturated environment. The plastics used in Chapter 6 are water-insoluble, but as particles they have the ability to interact with water and form droplets. Our main findings provided explanations and evidences as to why nano-plastics can be found in cold and remote places far from human activity. The size distribution and hygroscopicity models can help us estimate the lifetime and simulate the nano-plastics' transport in the atmosphere, and be applied in climate models to reduce the uncertainties from indirect effect. The low density particles as those measured in Chapter 6 can enter the atmosphere, travel to cold and high relative humidity places, form larger droplets and then deposit to the ground.

To summarize, this thesis employed laboratory-scale measurements to develop models and techniques to analyze plastics; a contaminant in the environment. Since nano-plastics are small, they can be studied by the aerosols theory and instrumentation. In future work, techniques in different fields can be synthesized to advance our understanding of nano-plastics. Different scientific and engineering perspectives will be necessary to understand the impact of nano-plastics to both human health and environment.

Appendix A: Supplemental Materials

A.1 Calibration of instruments

The instrumentation used in this thesis included electrostatic classifiers (TSI 3080), condensation particle counters (TSI 3776) cloud condensation nuclei counters (DMT CCNC100). The flow calibration of all three instruments followed the instructions in the manual. The flow of instruments was calibrated before the experiments using flow meters (CalDry Defender 520).

The DMAs in the electrostatic classifiers were wiped and cleaned by alcohol every six months.

After the flow of the CCNC was calibrated, the supersaturation of the CCNC was also calibrated before each experiment. Supersaturation calibrations were follow the instruction in the manual. Supersaturation was calibrated using ammonium sulfate with $\kappa = 0.604$. Five different supersaturations in the CCNC were set (0.2%, 0.4%, 0.6% 0.8% and 1.2%) and these supersaturation were called the instrumental supersaturation. Ammonium sulfate solution was made, and run through the SMCA process using the CCNC. The supersaturations calculated from ammonium sulfate using $\kappa = 0.604$ were called the measured supersaturation. Each supersaturation was measured three times. The calibration line between measured and supersaturation line was established ($R^2 > 0.99$). Figure A.1 shows an example of the calibration line between the instrumental and measured supersaturation.

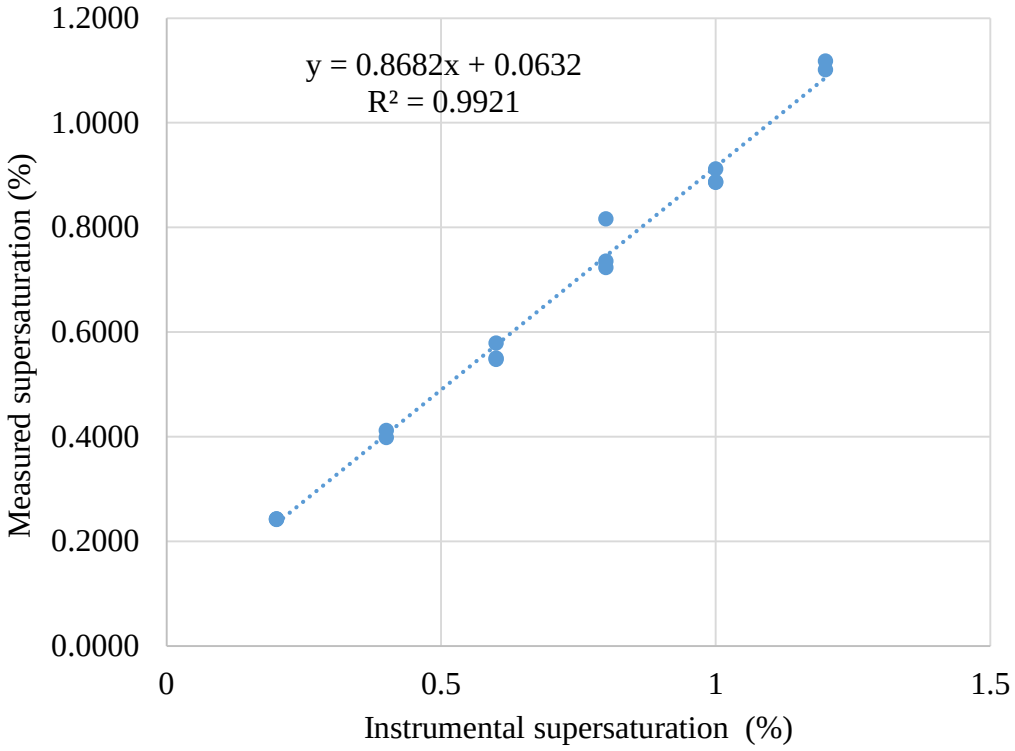

Figure A.1: An example of CCN supersaturation calibration (0.2% ~ 1.4 % supersaturation) on March 20, 2019.

A.2 Activation curves of mannitol, lactose, gelatin and PEG

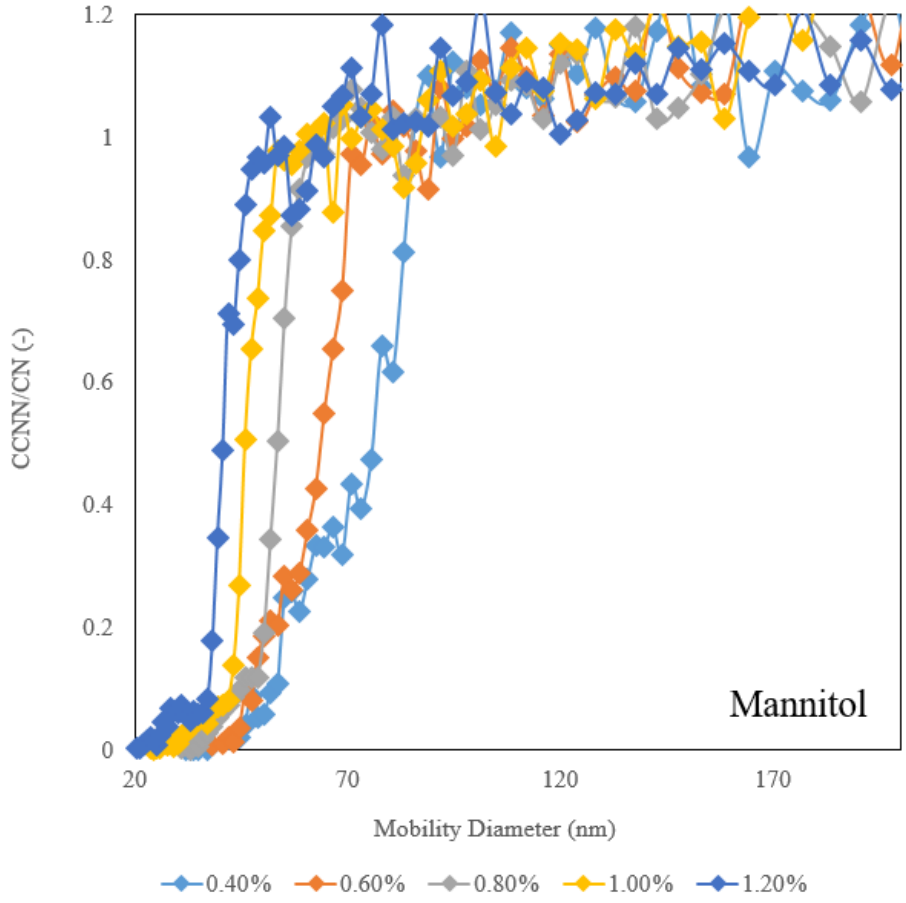

Figure A.2.1: The activation curves of mannitol under different supersaturation.

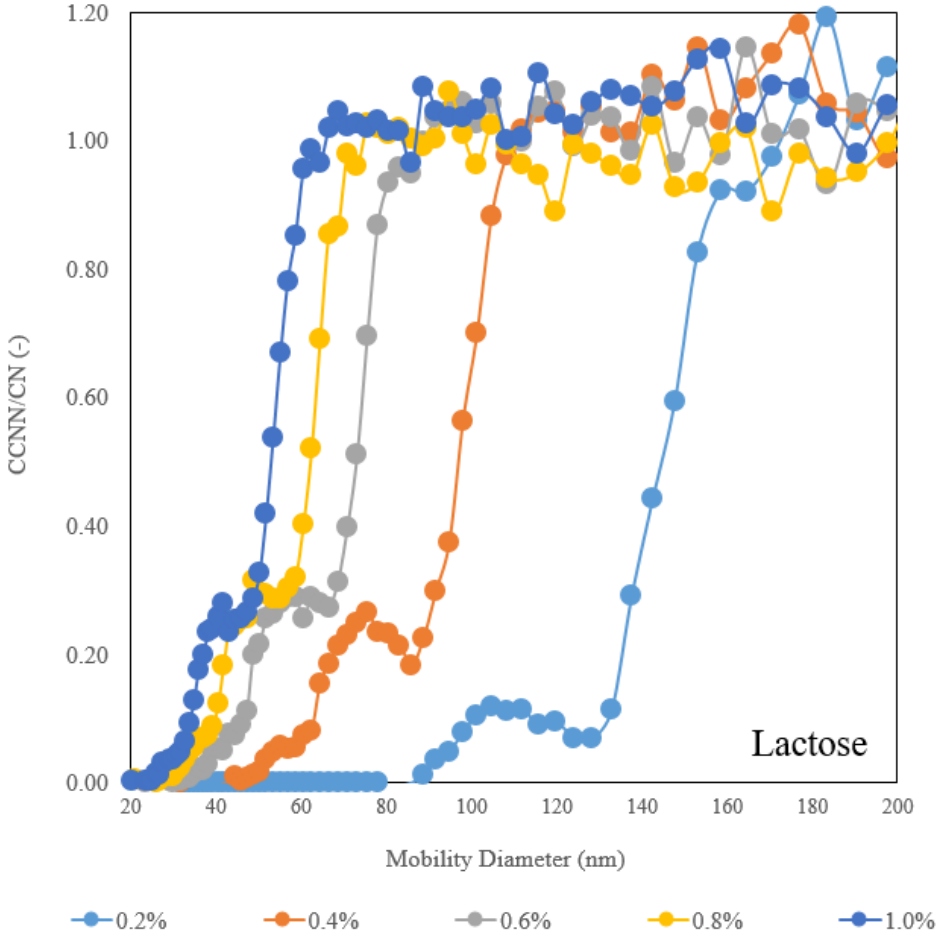

Figure A.2.2: The activation curves of lactose under different supersaturation.

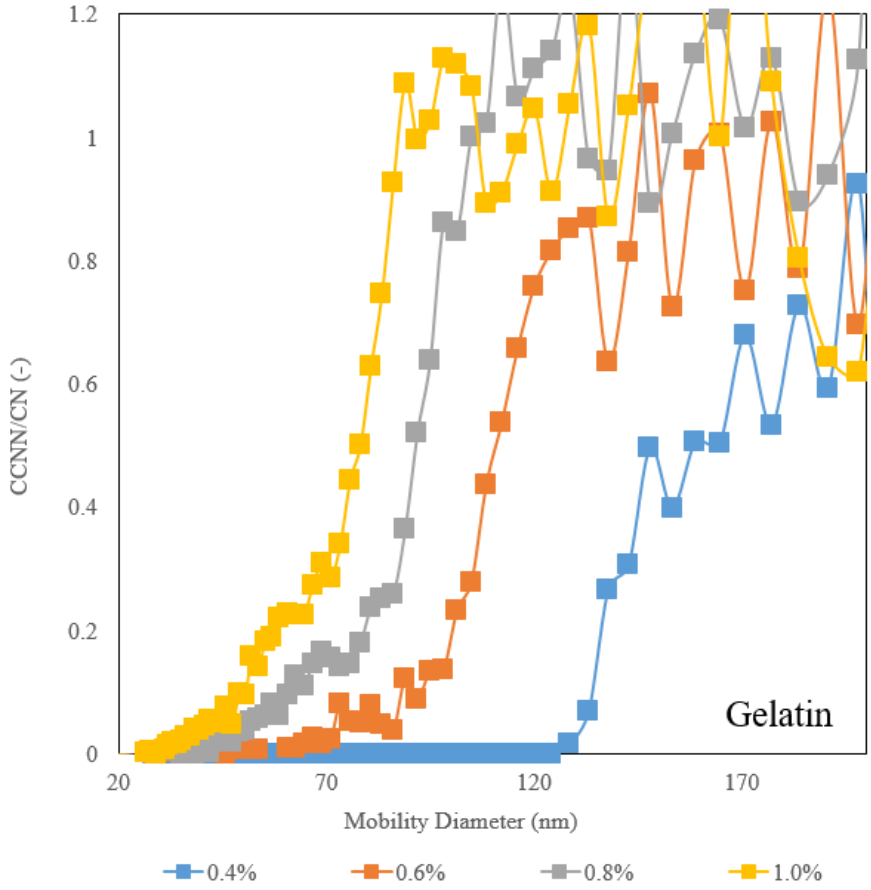

Figure A.2.3: The activation curves of gelatin under different supersaturation.

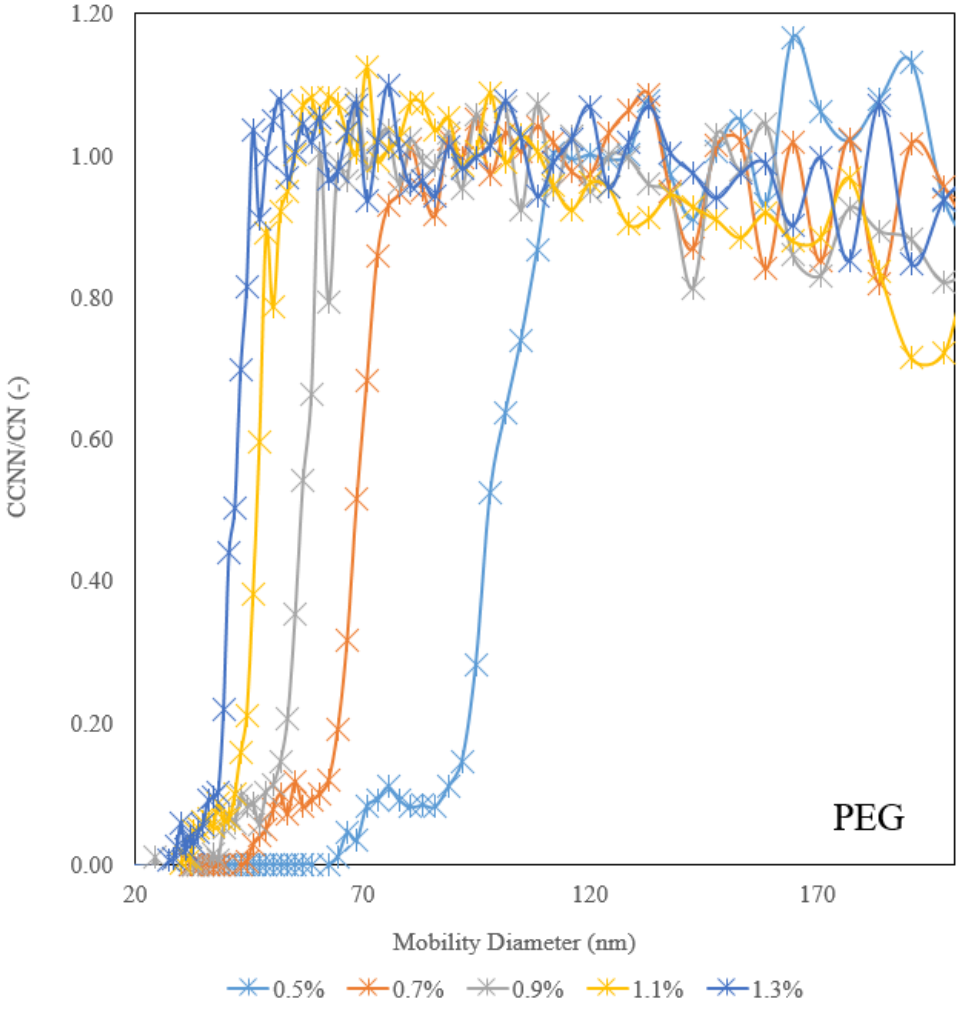

Figure A.2.4: The activation curves of PEG under different supersaturation.

A.3 The activation curve for PSL particles

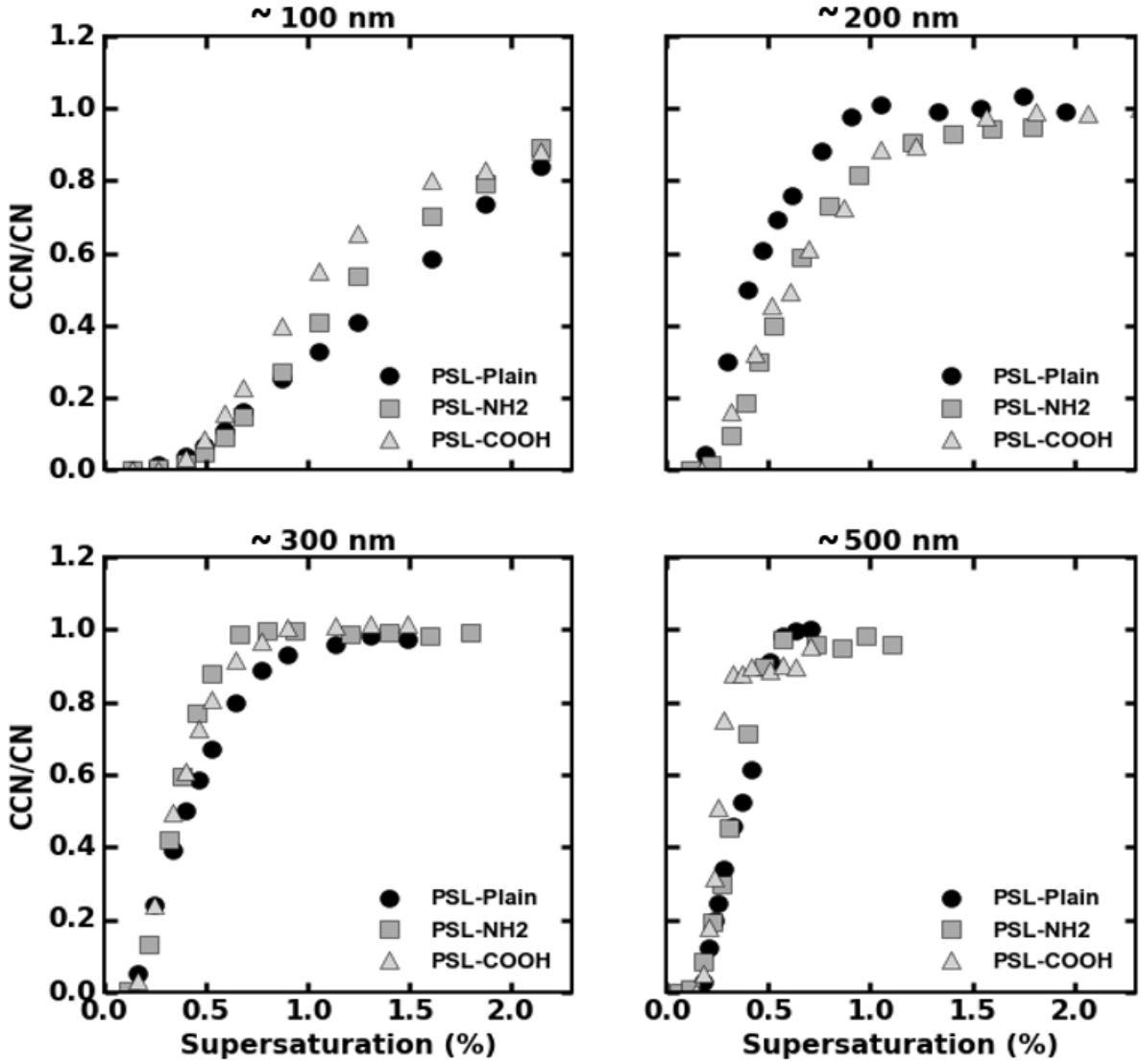

Figure A.3: The activation curve for PSL particles with amine group modification, carboxyl group modification and non-modification. Although the size of for different types of PSL is similar, but they are still not the same. Larger particles will activate earlier. As a result, it is hard to conclude the impact of surface chemistry to the CCN activity for similar size particles.

A.4 The size distribution of pure water

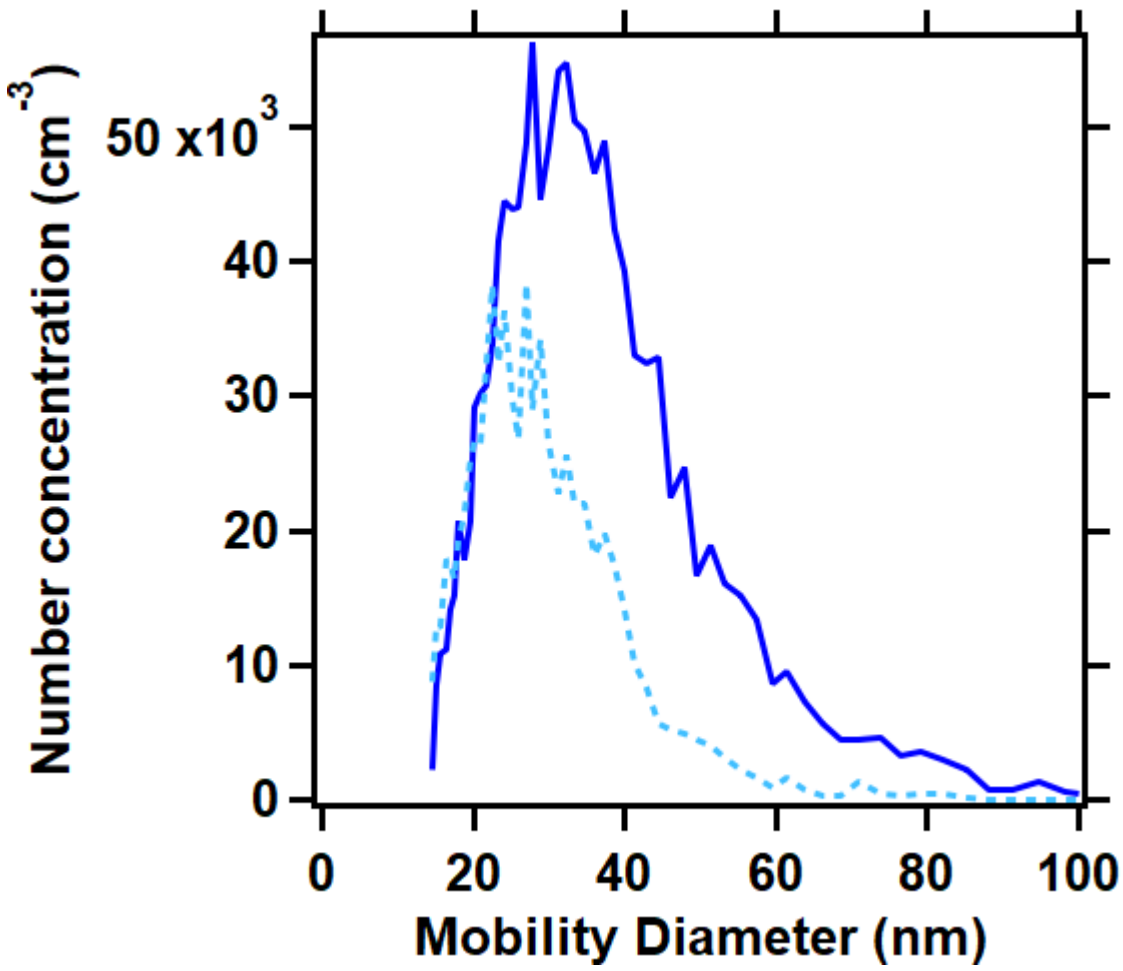

Figure A.4.1: A sample of the size distribution of ultrafine pure water before and after heating for one hour at 60 ℃.

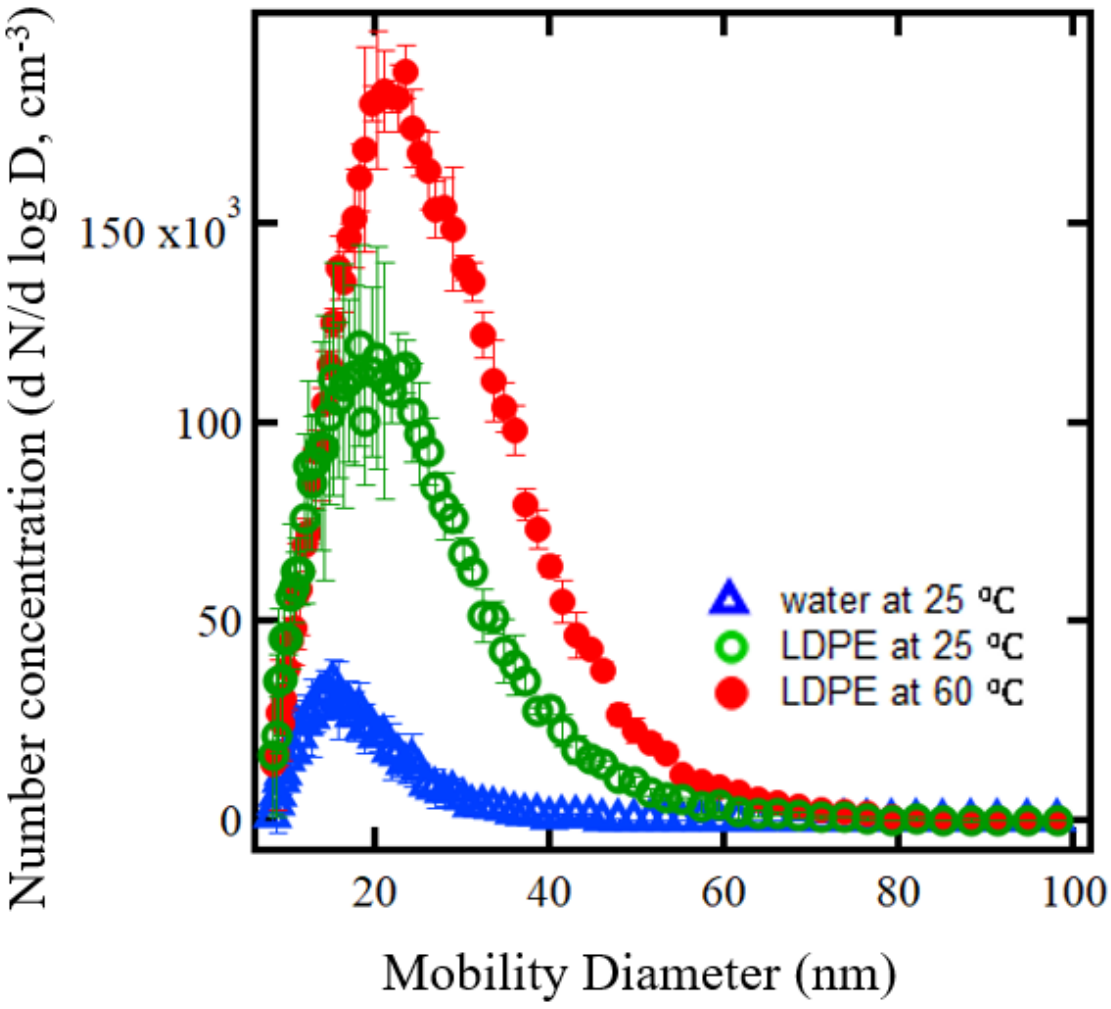

Figure A.4.2: The size distribution of water (before adding LDPE powders), LDPE at 25 ℃ (before heating) and LDPE at 60 ℃ (after heating).

Appendix B: Curriculum Vitae

Chun-Ning Mao

1811 Metzerott Rd. Apt 604 Adelphi 20783☎ 2405842765 ✉ cnmao@umd.edu

LinkedIn:Chun-Ning Mao

RESEARCH INTERESTS

- Chemical Engineering, Aerosol, and Atmospheric Science
- Scientific analyzing, experiments designing, criteria establishing and decision making
- Cloud condensation nuclei study, hygroscopicity, nano particles adsorption

ACADEMIC BACKGROUND

University of Maryland (UMD), A. James Clark School of Engineering

PhD Candidate , Chemical and Biomolecular Engineering *Graduation March 2023*

Thesis: The Hygroscopicity of Plastic Aerosols

Advanced courses grades (Cumulative GPA:3.804/4.0)

National Taiwan University (NTU), College of Engineering June 2017 Graduated

Bachelor of Science in Chemical Engineering (ChE) (GPA: 3.67/4.0)

RESEARCH EXPERIENCE

UMD Environmental Aerosol Research Lab (EARL)

Graduate Assistant Maryland,09/2018 – 03/2023

Project: Improving the droplet growth models for nano-scale biodegradable hydrophilic substances

- Developed models for water-uptake of nano-scale polymer drug carrying substances
- Simplified the single-parameter hygroscopicity for polymer and explained the thermodynamic meaning of each term

- Analyzed the growth of the nanoparticles in the respiratory system to enhance the efficiency of drug delivery

Project: Characterizing droplet growth model of functionalized insoluble aerosol surface

- Investigated the impact of different functionalized insoluble particles surface to the particle water-uptake ability and the Frenkel-Halsey-Hill adsorption theory hygroscopicity
- Assisted the derivation of Frenkel-Halsey-Hill adsorption theory hygroscopicity for the insoluble particles

Project: Identifying nano-plastics generation under different temperature using aerosols instrumentation

- Examined the existence of nano-plastics in water under different temperature utilizing aerosol instrumentation
- Analyzed the hygroscopicity model for the insoluble nano-plastics particles

NIST Material Measurement Laboratory

Student Internship Maryland,10/2019 – 06/2023

Project: The impact of low number concentration multiply-charged particles in extinction cross section measurement

- Established criteria for the number of charge corrections required in particle cross section measurement and analysis
- Collaborated with NIST and employed sophisticated aerosol optical measurements including Aerosol Particle Mass analyzer(APM), Cavity Ringdown Spectroscopy (CRD), and Photoacoustic Spectroscopy (PAS)

NTU Computational Molecular Engineering Laboratory

Research Assistant Taiwan,09/2016–06/2017

Project: Molecular Simulation: Verification of Water Heat Capacity Determined with 2 Phase

Theory

- Calculated theoretical heat capacity value of water emended by Quantum mechanics (2PT); verified values calculated by Gromacs
- Found the minimal simulation time using the block average method

INDUSTRIAL & WORK EXPERIENCE

Taiwan DuPont at Hsin-Chu EKC Department

Research Assistant Taiwan,07/2017 – 05/2018

- Characterized and improved the efficiency detergents by testing the metal loss of the wafer in PCMP (post chemical mechanical planarization) formulation
- Optimized testing process for the SiO_2 digestion of PCMP formulation
- Assisted Research and Development to solve the inhibitor filtration problem

Graduate Teaching Assistant at UMD

Maryland,09/2019 – 03/2020

- Guided students to succesfuly submit and understand course work in chemical reaction engineering; assisted in lectures and content delivery with recitations and office hours.

REFERREED PUBLICATIONS

Published Papers

1. Chun-Ning Mao, Kotiba A. Malek & Akua Asa-Awuku **(2021)** Hygroscopicity and the water-polymer interaction parameter of nano-sized biodegradable hydrophilic substances, Aerosol Science and Technology, 55:10, 1115-1124, DOI: 10.1080/02786826.2021.1931012

2. Gohil, K., Mao, Chun-Ning, Rastogi, D., Peng, C., Tang, M., and Asa-Awuku, A. **(2022)** Hybrid Water Adsorption and Solubility Partitioning for Aerosol Hygroscopicity and Droplet Growth, Atmos. Chem. Phys. Discuss. https://doi.org/10.5194/acp-2022-346.

3. Chun-Ning Mao, Gohil, K., and Asa-Awuku, A. **(2022)** A Single Parameter Hygroscopicity Model for Functionalized and Insoluble Aerosol Surfaces, Atmos. Chem. Phys. Discuss. https://doi.org/10.5194/acp-2022-339.

Papers in Progress

1. Impactor Collection Efficiencies Can Modify the Uncertainty of Multiply Charged Particles in Optical Extinction Measurements, Chun-Ning Mao, Akua Asa-Awuku, Christopher D. Zangmeister, Jamie L. Weaver and James G. Radney, 2023 *(under review)*

2. From Air to Water: Identifying the Nano-Plastic in Water Using Aerosol Techniques, *Chun-Ning Mao*, Dewansh Rastogi, Akua Asa-Awukua, Christopher D. Zangmeister, and James G. Radney, 2023

3. Wet Deposition is a Route for Plastics in Air to Earth Surface: The Hygroscopicity of Nano-Plastics, *Chun-Ning Mao*, Kanishk Gohil, Akua Asa-Awukua, Christopher D. Zangmeister, and James G. Radney, 2023

CONFERENCE PRESENTATIONS

1. A Single Parameter Hygroscopicity Model for Functionalized and Insoluble Aerosol Surfaces, Chun-Ning Mao, Kanishk Gohil, and Akua Asa-Awuku. American Association for Aerosol Research (AAAR) 40th Annual Conference, October 03-07, 2022
2. Differences in Droplet Growth Model of Functionalized Insoluble Aerosol Surfaces, Chun-Ning Mao, Kanishk Gohil, and Akua Asa-Awuku. iCACGP-IGAC Joint International Atmospheric Chemistry Conference, September 10-15, 2022, in Manchester (Virtual

Poster)

3. The particles we don't count can significantly bias optical measurements, Chun-Ning Mao, Akua Asa-Awuku, James Radney, Christopher Zangmeister. American Association for Aerosol Research (AAAR) 39th Annual Conference, October 18-22, 2021, Virtual- Albuquerque, New Mexico
4. The single parameter hygroscopicity of biodegradable polymers, Chun-Ning Mao, Kotiba Malek, Akua Asa-Awuku. American Institute of Chemical Engineering (AIChe) 2021 Annual Meeting, November 18, 2021 – Boston, MA2021
5. Ammonium Sulfate: Good for Optical Diagnostics but Not Quite Good Enough for Calibration. James Radney, Christopher Zangmeister, Chun-Ning Mao, Akua Asa-Awuku, American Association for Aerosol Research (AAAR) 39th Annual Conference, October 18-22, 2021, Virtual- Albuquerque, New Mexic
6. Determination of the Water-polymer Interaction Parameter and Hygroscopicity of Particles. Chun-Ning Mao, Akua Asa-Awuku. American Association for Aerosol Research (AAAR) 38th Annual Conference, October 5-9, 2020. Virtual- Raleigh, NC

ADDITIONAL SKILLS

- Aerosol measurement instrumentation (CPC, DMA, CCNC)
- Software: Matlab, Igor, Microsoft software (Excel, PowerPoint, Word)
- ICP-MS operation
- Fluent in Mandarin

Appendix C: List of Publications and Presentations

Published Papers

1. Chun-Ning Mao, Kotiba A. Malek & Akua Asa-Awuku **(2021)** Hygroscopicity and the water-polymer interaction parameter of nano-sized biodegradable hydrophilic substances, Aerosol Science and Technology, 55:10, 1115-1124, DOI: 10.1080/02786826.2021.1931012

2. Gohil, K., Mao, Chun-Ning, Rastogi, D., Peng, C., Tang, M., and Asa-Awuku, A. **(2022)** Hybrid Water Adsorption and Solubility Partitioning for Aerosol Hygroscopicity and Droplet Growth, Atmos. Chem. Phys. Discuss. https://doi.org/10.5194/acp-2022-346.

3. Chun-Ning Mao, Gohil, K., and Asa-Awuku, A. **(2022)** A Single Parameter Hygroscopicity Model for Functionalized and Insoluble Aerosol Surfaces, Atmos. Chem. Phys. Discuss. https://doi.org/10.5194/acp-2022-339.

Papers in Progress

4. Impactor Collection Efficiencies Can Modify the Uncertainty of Multiply Charged Particles in Optical Extinction Measurements, Chun-Ning Mao, Akua Asa-Awuku, Christopher D. Zangmeister, Jamie L. Weaver and James G. Radney, 2023 *(under review)*

5. From Air to Water: Identifying the Nano-Plastic in Water Using Aerosol Techniques, *Chun-Ning Mao*, Dewansh Rastogi, Akua Asa-Awuku, Christopher D. Zangmeister, and James G. Radney, 2023

6. Wet Deposition is a Route for Plastics in Air to Earth Surface: The Hygroscopicity of

Nano-Plastics, *Chun-Ning Mao*, Kanishk Gohil, Akua Asa-Awuku, Christopher D. Zangmeister, and James G. Radney, 2023

List of Presentation

1. A Single Parameter Hygroscopicity Model for Functionalized and Insoluble Aerosol Surfaces, Chun-Ning Mao, Kanishk Gohil, and Akua Asa-Awuku. American Association for Aerosol Research (AAAR) 40th Annual Conference, October 03-07, 2022
2. Differences in Droplet Growth Model of Functionalized Insoluble Aerosol Surfaces, Chun-Ning Mao, Kanishk Gohil, and Akua Asa-Awuku. iCACGP-IGAC Joint International Atmospheric Chemistry Conference, September 10-15, 2022, in Manchester (Virtual Poster)
3. The particles we don't count can significantly bias optical measurements, Chun-Ning Mao, Akua Asa-Awuku, James Radney, Christopher Zangmeister. American Association for Aerosol Research (AAAR) 39th Annual Conference, October 18-22, 2021, Virtual- Albuquerque, New Mexico
4. The single parameter hygroscopicity of biodegradable polymers, Chun-Ning Mao, Kotiba Malek, Akua Asa-Awuku. American Institute of Chemical Engineering (AIChe) 2021 Annual Meeting, November 18, 2021 – Boston, MA2021
5. Ammonium Sulfate: Good for Optical Diagnostics but Not Quite Good Enough for Calibration. James Radney, Christopher Zangmeister, Chun-Ning Mao, Akua Asa-Awuku, American Association for Aerosol Research (AAAR) 39th Annual Conference, October 18-22, 2021, Virtual- Albuquerque, New Mexico
6. Determination of the Water-polymer Interaction Parameter and Hygroscopicity of Particles. Chun-Ning Mao, Akua Asa-Awuku. American Association for Aerosol Research (AAAR)

Appendix D: Sources of Funding

I, Chun-Ning Mao, would like to acknowledge the following awards below that have funded the research presented in this thesis: National Science Foundation Grant AGS-1708337 and AGS- 1151893

Bibliography

Aeschlimann, Mischa, Guangyu Li, Zamin A. Kanji, and Denise M. Mitrano. 2022a. "Potential Impacts of Atmospheric Microplastics and Nanoplastics on Cloud Formation Processes." *Nature Geoscience 2022 15:12* 15 (12): 967–75. https://doi.org/10.1038/s41561-022-01051-9.

———. 2022b. "Potential Impacts of Atmospheric Microplastics and Nanoplastics on Cloud Formation Processes." *Nature Geoscience 2022 15:12* 15 (12): 967–75. https://doi.org/10.1038/s41561-022-01051-9.

Agnihotri, Sunil A., Nadagouda N. Mallikarjuna, and Tejraj M. Aminabhavi. 2004. "Recent Advances on Chitosan-Based Micro- and Nanoparticles in Drug Delivery." *Journal of Controlled Release*. Elsevier. https://doi.org/10.1016/j.jconrel.2004.08.010.

Alimi, Olubukola S., Dominique Claveau-Mallet, Rafael S. Kurusu, Mathieu Lapointe, Stéphane Bayen, and Nathalie Tufenkji. 2022. "Weathering Pathways and Protocols for Environmentally Relevant Microplastics and Nanoplastics: What Are We Missing?" *Journal of Hazardous Materials* 423 (February): 126955. https://doi.org/10.1016/J.JHAZMAT.2021.126955.

Allen, Steve, Deonie Allen, Kerry Moss, Gaël Le Roux, Vernon R. Phoenix, and Jeroen E. Sonke. 2020. "Examination of the Ocean as a Source for Atmospheric Microplastics." *PLOS ONE* 15 (5): e0232746. https://doi.org/10.1371/JOURNAL.PONE.0232746.

Allen, Steve, Deonie Allen, Vernon R Phoenix, Gaël Le Roux, Pilar Durántez Jiménez, Anaëlle Simonneau, Stéphane Binet, and Didier Galop. 2019. “Atmospheric Transport and Deposition of Microplastics in a Remote Mountain Catchment.” *Nature Geoscience* 12 (5): 339–44. https://doi.org/10.1038/s41561-019-0335-5.

Anbarasan, Arigo, Jawahar Nataraj, Nikhitha Shanmukhan, and Arun Radhakrishnan. 2018. “Effect of Hygroscopicity on Pharmaceutical Ingredients, Methods to Determine and Overcome: An Overview.” *Available Online Www.Jocpr.Com Journal of Chemical and Pharmaceutical Research* 10 (3): 61–67. www.jocpr.com.

Andrady, Anthony L. 2011. “Microplastics in the Marine Environment.” *Marine Pollution Bulletin*. Pergamon. https://doi.org/10.1016/j.marpolbul.2011.05.030.

Arp, Hans Peter H., Dana Kühnel, Christoph Rummel, Matthew MacLeod, Annegret Potthoff, Sophia Reichelt, Elisa Rojo-Nieto, et al. 2021. “Weathering Plastics as a Planetary Boundary Threat: Exposure, Fate, and Hazards.” *Environmental Science & Technology* 55 (11): 7246–55. https://doi.org/10.1021/acs.est.1c01512.

Atkinson, Dean B. 2003. “Solving Chemical Problems of Environmental Importance Using Cavity Ring-down Spectroscopy.” *Analyst*. Royal Society of Chemistry. https://doi.org/10.1039/b206699h.

Azarmi, Shirzad, Wilson H. Roa, and Raimar Löbenberg. 2008. “Targeted Delivery of Nanoparticles for the Treatment of Lung Diseases.” *Advanced Drug Delivery Reviews*.

Elsevier. https://doi.org/10.1016/j.addr.2007.11.006.

Batool, Iffat, Abdul Qadir, Joseph M. Levermore, and Frank J. Kelly. 2022. “Dynamics of Airborne Microplastics, Appraisal and Distributional Behaviour in Atmosphere; a Review.” *Science of The Total Environment* 806 (February): 150745. https://doi.org/10.1016/J.SCITOTENV.2021.150745.

Bergmann, Melanie, Sophia Mützel, Sebastian Primpke, Mine B. Tekman, Jürg Trachsel, and Gunnar Gerdts. 2019. “White and Wonderful? Microplastics Prevail in Snow from the Alps to the Arctic.” *Science Advances* 5 (8). https://doi.org/10.1126/sciadv.aax1157.

Bilal, Muhammad, Rehan Ullah, Hazrat Ali, Ibrar Hussain, and Basit Ali Khan. 2021. “Overview of Microplastics Threat in Aquatic.” *International Journal of Research and Analytical Reviews*. www.ijrar.org.

Bluvshtein, N., J. M. Flores, A. Abo Riziq, and Y. Rudich. 2012. “An Approach for Faster Retrieval of Aerosols’ Complex Refractive Index Using Cavity Ring-down Spectroscopy.” *Aerosol Science and Technology* 46 (10): 1140–50. https://doi.org/10.1080/02786826.2012.700141.

Borchard, W., W. Bremer, and A. Keese. 1980. “The State Diagram of the Water-Gelatin System.” *Colloid and Polymer Science Kolloid-Zeitschrift & Zeitschrift Für Polymere* 258 (5): 516–26. https://doi.org/10.1007/BF01404159.

Broday, David M., and Panos G. Georgopoulos. 2001. “Growth and Deposition of

Hygroscopic Particulate Matter in the Human Lungs." *Aerosol Science and Technology* 34 (1): 144–59. https://doi.org/10.1080/02786820118725.

Buys, T S, and K De Clerk. n.d. "Bi-Gaussian Fitting of Skewed Peaks." Accessed August 5, 2021. https://pubs.acs.org/sharingguidelines.

Corcoran, Patricia L., Mark C. Biesinger, and Meriem Grifi. 2009. "Plastics and Beaches: A Degrading Relationship." *Marine Pollution Bulletin* 58 (1): 80–84. https://doi.org/10.1016/J.MARPOLBUL.2008.08.022.

Costa, João Pinto da, Patrícia S.M. Santos, Armando C. Duarte, and Teresa Rocha-Santos. 2016a. "(Nano)Plastics in the Environment - Sources, Fates and Effects." *Science of the Total Environment*. Elsevier B.V. https://doi.org/10.1016/j.scitotenv.2016.05.041.

———. 2016b. "(Nano)Plastics in the Environment – Sources, Fates and Effects." *Science of The Total Environment* 566–567 (October): 15–26. https://doi.org/10.1016/J.SCITOTENV.2016.05.041.

Cotterell, Michael I., Thomas C. Preston, Bernard J. Mason, Andrew J. Orr-Ewing, and Jonathan P. Reid. 2015. "Extinction Cross Section Measurements for a Single Optically Trapped Particle." In *Optical Trapping and Optical Micromanipulation XII*, 9548:95480C. SPIE. https://doi.org/10.1117/12.2189174.

Cotterell, Michael I., Kate Szpek, Jim M. Haywood, and Justin M. Langridge. 2020. "Sensitivity and Accuracy of Refractive Index Retrievals from Measured Extinction and

Absorption Cross Sections for Mobility-Selected Internally Mixed Light Absorbing Aerosols." *Aerosol Science and Technology*, May, 1–24. https://doi.org/10.1080/02786826.2020.1757034.

Cózar, Andrés, Elisa Martí, Carlos M. Duarte, Juan García-de-Lomas, Erik Van Sebille, Thomas J. Ballatore, Victor M. Eguíluz, et al. 2017. "The Arctic Ocean as a Dead End for Floating Plastics in the North Atlantic Branch of the Thermohaline Circulation." *Science Advances* 3 (4): e1600582. https://doi.org/10.1126/sciadv.1600582.

Crosby, Alfred J., and Jong-Young Lee. 2007. "Polymer Nanocomposites: The 'Nano' Effect on Mechanical Properties." *Polymer Reviews* 47 (2): 217–29. https://doi.org/10.1080/15583720701271278.

Cziczo, Daniel J., Karl D. Froyd, Stephane J. Gallavardin, Ottmar Moehler, Stefan Benz, Harald Saathoff, and Daniel M. Murphy. 2009. "Deactivation of Ice Nuclei Due to Atmospherically Relevant Surface Coatings." *Environmental Research Letters* 4 (4): 044013. https://doi.org/10.1088/1748-9326/4/4/044013.

d'Almeida, Guillaume A. 1986. "A Model for Saharan Dust Transport." *Journal of Climate and Applied Meteorology* 25 (7): 903–16. https://doi.org/10.1175/1520-0450(1986)025<0903:AMFSDT>2.0.CO;2.

Dalirian, Maryam, Arttu Ylisirniö, Angela Buchholz, Daniel Schlesinger, Johan Ström, Annele Virtanen, and Ilona Riipinen. 2018. "Cloud Droplet Activation of Black Carbon

Particles Coated with Organic Compounds of Varying Solubility." *Atmospheric Chemistry and Physics* 18 (16): 12477–89. https://doi.org/10.5194/ACP-18-12477-2018.

Dawson, Joseph Nelson, Kotiba A. Malek, Patricia N. Razafindrambinina, Timothy M. Raymond, Dabrina D. Dutcher, Akua A. Asa-Awuku, and Miriam Arak Freedman. 2020. "Direct Comparison of the Submicron Aerosol Hygroscopicity of Water-Soluble Sugars." *ACS Earth and Space Chemistry* 4 (12): 2215–26. https://doi.org/10.1021/acsearthspacechem.0c00159.

Dinar, E., T. Anttila, and Y. Rudich. 2008. "CCN Activity and Hygroscopic Growth of Organic Aerosols Following Reactive Uptake of Ammonia." *Environmental Science and Technology* 42 (3): 793–99. https://doi.org/10.1021/es071874p.

Dormidontova, Elena E. 2002. "Role of Competitive PEO-Water and Water-Water Hydrogen Bonding in Aqueous Solution PEO Behavior." *Macromolecules* 35 (3): 987–1001. https://doi.org/10.1021/ma010804e.

Dusek, U., G. P. Frank, L. Hildebrandt, J. Curtius, J. Schneider, S. Walter, D. Chand, et al. 2006. "Size Matters More Than Chemistry for Cloud-Nucleating Ability of Aerosol Particles." *Science* 312 (5778): 1375–78. https://doi.org/10.1126/science.1125261.

Ehara, Kensei, Charles Hagwood, and Kevin J. Coakley. 1996. "Novel Method to Classify Aerosol Particles According to Their Mass-to-Charge Ratio—Aerosol Particle Mass Analyser." *Journal of Aerosol Science* 27 (2): 217–34. https://doi.org/10.1016/0021-

8502(95)00562-5.

Eldridge, Ralph G. 1957. “MEASUREMENTS OF CLOUD DROP-SIZE DISTRIBUTIONS.” *Journal of the Atmospheric Sciences* 14 (1): 55–59. https://doi.org/10.1175/0095-9634-14.1.55.

Everest, Michael A., and Dean B. Atkinson. 2008. “Discrete Sums for the Rapid Determination of Exponential Decay Constants.” *Review of Scientific Instruments* 79 (2): 023108. https://doi.org/10.1063/1.2839918.

Fan, Wenxia, Jennifer A. Salmond, Kim N. Dirks, Patricia Cabedo Sanz, Gordon M. Miskelly, and Joel D. Rindelaub. 2022. “Evidence and Mass Quantification of Atmospheric Microplastics in a Coastal New Zealand City.” *Environmental Science & Technology*, December. https://doi.org/10.1021/ACS.EST.2C05850.

Filipe, Vasco, Andrea Hawe, and Wim Jiskoot. 2010. “Critical Evaluation of Nanoparticle Tracking Analysis (NTA) by NanoSight for the Measurement of Nanoparticles and Protein Aggregates.” *Pharmaceutical Research* 27 (5): 796–810. https://doi.org/10.1007/s11095-010-0073-2.

Flory, Paul J. 1942. “The Thermodynamics of High Polymer Solutions. V. Phase Equilibria in the Ternary System: Polymer 1-Polymer 2-Solvent The.” *Statistical Mechanics of Cross-Linked Polymer Networks II. Swelling The Journal of Chemical Physics* 10: 279. https://doi.org/10.1063/1.1723621.

Fuchs, N. A. 1963. “On the Stationary Charge Distribution on Aerosol Particles in a Bipolar Ionic Atmosphere.” *Geofisica Pura e Applicata* 56 (1): 185–93. https://doi.org/10.1007/BF01993343.

Geyer, Roland, Jenna R. Jambeck, and Kara Lavender Law. 2017. “Production, Use, and Fate of All Plastics Ever Made.” *Science Advances* 3 (7). https://doi.org/10.1126/sciadv.1700782.

Gigault, Julien, Alexandra ter Halle, Magalie Baudrimont, Pierre Yves Pascal, Fabienne Gauffre, Thuy Linh Phi, Hind El Hadri, Bruno Grassl, and Stéphanie Reynaud. 2018. “Current Opinion: What Is a Nanoplastic?” *Environmental Pollution*. Elsevier Ltd. https://doi.org/10.1016/j.envpol.2018.01.024.

Gigault, Julien, Boris Pedrono, Benoît Maxit, and Alexandra Ter Halle. 2016. “Marine Plastic Litter: The Unanalyzed Nano-Fraction.” *Environmental Science: Nano* 3 (2): 346–50. https://doi.org/10.1039/C6EN00008H.

Gill, Simardeep, Raimar Löbenberg, Tabitha Ku, Shirzad Azarmi, Wilson Roa, and Elmar J. Prenner. 2007. “Nanoparticles: Characteristics, Mechanisms of Action, and Toxicity in Pulmonary Drug Delivery - A Review.” *Journal of Biomedical Nanotechnology*. https://doi.org/10.1166/jbn.2007.015.

Gillibert, Raymond, Gireeshkumar Balakrishnan, Quentin Deshoules, Morgan Tardivel, Alessandro Magazzù, Maria Grazia Donato, Onofrio M. Maragò, et al. 2019. “Raman

Tweezers for Small Microplastics and Nanoplastics Identification in Seawater." *Environmental Science & Technology* 53 (15): 9003–13. https://doi.org/10.1021/acs.est.9b03105.

Gohil, Kanishk, and Akua A. Asa-Awuku. 2022. "Cloud Condensation Nuclei (CCN) Activity Analysis of Low-Hygroscopicity Aerosols Using the Aerodynamic Aerosol Classifier (AAC)." *Atmospheric Measurement Techniques* 15 (4): 1007–19. https://doi.org/10.5194/AMT-15-1007-2022.

Gohil, Kanishk, Chun-Ning Mao, Dewansh Rastogi, Chao Peng, Mingjin Tang, and Akua Asa-Awuku. 2022. "Hybrid Water Adsorption and Solubility Partitioning for Aerosol Hygroscopicity and Droplet Growth." *Atmospheric Chemistry and Physics* 22 (19): 12769–87. https://doi.org/10.5194/ACP-22-12769-2022.

Gunn, Ross. 1955. "The Statistical Electrification of Aerosols by Ionic Diffusion." *Journal of Colloid Science* 10 (1): 107–19. https://doi.org/10.1016/0095-8522(55)90081-7.

Haegerbaeumer, Arne, Marie Theres Mueller, Hendrik Fueser, and Walter Traunspurger. 2019. "Impacts of Micro- and Nano-Sized Plastic Particles on Benthic Invertebrates: A Literature Review and Gap Analysis." *Frontiers in Environmental Science*. Frontiers Media S.A. https://doi.org/10.3389/fenvs.2019.00017.

Hahm, Jong In. 2014. "Fundamentals of Nanoscale Polymer-Protein Interactions and Potential Contributions to Solid-State Nanobioarrays." *Langmuir* 30 (33): 9891–9904.

https://doi.org/10.1021/la404481t.

Halle, Alexandra Ter, Laurent Jeanneau, Marion Martignac, Emilie Jardé, Boris Pedrono, Laurent Brach, and Julien Gigault. 2017. “Nanoplastic in the North Atlantic Subtropical Gyre.” *Environmental Science & Technology* 51 (23): 13689–97. https://doi.org/10.1021/acs.est.7b03667.

Halmer, Daniel, Golo von Basum, Peter Hering, and Manfred Mürtz. 2004. “Fast Exponential Fitting Algorithm for Real-Time Instrumental Use.” *Review of Scientific Instruments* 75 (6): 2187. https://doi.org/10.1063/1.1711189.

Hartmann, NB, T Nolte, … MA Sørensen - ASLO Aquatic Sciences, and undefined 2015. 2017. “Aquatic Ecotoxicity Testing of Nanoplastics: Lessons Learned from Nanoecotoxicology.” *Core.Ac.Uk*, 43–44. https://core.ac.uk/download/pdf/84002496.pdf.

Hatch, Courtney D., Ann L. Greenaway, Matthew J. Christie, and Jonas Baltrusaitis. 2014. “Water Adsorption Constrained Frenkel–Halsey–Hill Adsorption Activation Theory: Montmorillonite and Illite.” *Atmospheric Environment* 87 (April): 26–33. https://doi.org/10.1016/J.ATMOSENV.2013.12.040.

Hatch, Courtney D., Jadon S. Wiese, Cameron C. Crane, Kenneth J. Harris, Hannah G. Kloss, and Jonas Baltrusaitis. 2012. “Water Adsorption on Clay Minerals As a Function of Relative Humidity: Application of BET and Freundlich Adsorption Models.” *Langmuir*

28 (3): 1790–1803. https://doi.org/10.1021/LA2042873.

Herich, Hanna, Torsten Tritscher, Aldona Wiacek, Martin Gysel, Ernest Weingartner, Lohmann Ulrike, Baltensperger Urs, and Cziczo Daniel J. 2009. “Water Uptake of Clay and Desert Dust Aerosol Particles at Sub- and Supersaturated Water Vapor Conditions.” *Physical Chemistry Chemical Physics* 11 (36): 7804–9. https://doi.org/10.1039/B901585J.

Hernandez, Laura M., Nariman Yousefi, and Nathalie Tufenkji. 2017. “Are There Nanoplastics in Your Personal Care Products?” *Environmental Science and Technology Letters* 4 (7): 280–85. https://doi.org/10.1021/acs.estlett.7b00187.

Hindle, Michael, and P. Worth Longest. 2010. “Evaluation of Enhanced Condensational Growth (ECG) for Controlled Respiratory Drug Delivery in a Mouth-Throat and Upper Tracheobronchial Model.” *Pharmaceutical Research* 27 (9): 1800–1811. https://doi.org/10.1007/s11095-010-0165-z.

Hoppel, W. A., S. Twomey, and T. A. Wojciechowski. 1979. “A Segmented Thermal Diffusion Chamber for Continuous Measurements of CN.” *Journal of Aerosol Science* 10 (4): 369–73. https://doi.org/10.1016/0021-8502(79)90031-4.

IPCC. 2021. “The Physical Science Basis. Contribution of Working Group I of the IPCC (Summary for Policymakers).”

Johnson, Tyler J., Robert T. Nishida, Martin Irwin, Jonathan P.R. Symonds, Jason S. Olfert,

and Adam M. Boies. 2020. “Measuring the Bipolar Charge Distribution of Nanoparticles: Review of Methodologies and Development Using the Aerodynamic Aerosol Classifier.” *Journal of Aerosol Science* 143 (May): 105526. https://doi.org/10.1016/j.jaerosci.2020.105526.

Julienne, Fanon, Fabienne Lagarde, Jean François Bardeau, and Nicolas Delorme. 2022. “Thin Polyethylene (LDPE) Films with Controlled Crystalline Morphology for Studying Plastic Weathering and Microplastic Generation.” *Polymer Degradation and Stability* 195 (January): 109791. https://doi.org/10.1016/J.POLYMDEGRADSTAB.2021.109791.

Kalberer, M., D. Paulsen, M. Sax, M. Steinbacher, J. Dommen, A. S.H. Prevot, R. Fisseha, et al. 2004. “Identification of Polymers as Major Components of Atmospheric Organic Aerosols.” *Science* 303 (5664): 1659–62. https://doi.org/10.1126/science.1092185.

Kallos, George, Anastasios Papadopoulos, Petros Katsafados, and Slobodan Nickovic. 2006. “Transatlantic Saharan Dust Transport: Model Simulation and Results.” *Journal of Geophysical Research Atmospheres* 111 (9). https://doi.org/10.1029/2005JD006207.

Karim, Syed Shujaat, Sarah Farrukh, Takeshi Matsuura, Muhammad Ahsan, Arshad Hussain, Sehar Shakir, Lai Fatt Chuah, Mudassir Hasan, and Awais Bokhari. 2022. “Model Analysis on Effect of Temperature on the Solubility of Recycling of Polyethylene Terephthalate (PET) Plastic.” *Chemosphere* 307 (November): 136050.

https://doi.org/10.1016/J.CHEMOSPHERE.2022.136050.

Karimi, M., W. Albrecht, M. Heuchel, M. H. Kish, J. Frahn, Th Weigel, D. Hofmann, H. Modarress, and A. Lendlein. 2005. “Determination of Water/Polymer Interaction Parameter for Membrane-Forming Systems by Sorption Measurement and a Fitting Technique.” *Journal of Membrane Science* 265 (1–2): 1–12. https://doi.org/10.1016/j.memsci.2005.04.030.

Karydis, Vlassis A., Alexandra P. Tsimpidi, Sara Bacer, Andrea Pozzer, Athanasios Nenes, and Jos Lelieveld. 2017. “Global Impact of Mineral Dust on Cloud Droplet Number Concentration.” *Atmospheric Chemistry and Physics* 17 (9): 5601–21. https://doi.org/10.5194/ACP-17-5601-2017.

Kelly, A., D. Lannuzel, T. Rodemann, K. M. Meiners, and H. J. Auman. 2020. “Microplastic Contamination in East Antarctic Sea Ice.” *Marine Pollution Bulletin* 154 (May). https://doi.org/10.1016/j.marpolbul.2020.111130.

Kim, Jong Won, Jinxiang Xi, and Xiuhua A. Si. 2013. “Dynamic Growth and Deposition of Hygroscopic Aerosols in the Nasal Airway of a 5-Year-Old Child.” *International Journal for Numerical Methods in Biomedical Engineering* 29 (1): 17–39. https://doi.org/10.1002/cnm.2490.

Klaine, Stephen J, Albert A Koelmans, Nina Horne, Stephen Carley, Richard D Handy, Larry Kapustka, Bernd Nowack, and Frank Von Der Kammer. 2012. “Paradigms to Assess the

Environmental Impact of Manufactured Nanomaterials." *Citeseer*. https://doi.org/10.1002/etc.733.

Knutson, E. O., and K. T. Whitby. 1975. "Aerosol Classification by Electric Mobility: Apparatus, Theory, and Applications." *Journal of Aerosol Science* 6 (6): 443–51. https://doi.org/10.1016/0021-8502(75)90060-9.

Koehler, Kirsten A., Paul J. Demott, Sonia M. Kreidenweis, Olga B. Popovicheva, Markus D. Petters, Christian M. Carrico, Elena D. Kireeva, Tatiana D. Khokhlova, and Natalia K. Shonija. 2009. "Cloud Condensation Nuclei and Ice Nucleation Activity of Hydrophobic and Hydrophilic Soot Particles." *Physical Chemistry Chemical Physics* 11 (36): 7906–20. https://doi.org/10.1039/B905334B.

Koelmans, Albert A., Ellen Besseling, and Won J. Shim. 2015. "Nanoplastics in the Aquatic Environment. Critical Review." In *Marine Anthropogenic Litter*, 325–40. Springer International Publishing. https://doi.org/10.1007/978-3-319-16510-3_12.

Köhler, Hilding. 1936. "The Nucleus in and the Growth of Hygroscopic Droplets." *Transactions of the Faraday Society* 32 (0): 1152–61. https://doi.org/10.1039/TF9363201152.

Kreidenweis, S. M., and A. Asa-Awuku. 2013. "Aerosol Hygroscopicity: Particle Water Content and Its Role in Atmospheric Processes." *Treatise on Geochemistry: Second Edition* 5: 331–61. https://doi.org/10.1016/B978-0-08-095975-7.00418-6.

Kumar, Prashant, Athanasios Nenes, and Irina N. Sokolik. 2009. “Importance of Adsorption for CCN Activity and Hygroscopic Properties of Mineral Dust Aerosol.” *Geophysical Research Letters* 36 (24): L24804. https://doi.org/10.1029/2009GL040827.

Lai, Yujian, Lijie Dong, Qingcun Li, Peng Li, Zhineng Hao, Sujuan Yu, and Jingfu Liu. 2021. “Counting Nanoplastics in Environmental Waters by Single Particle Inductively Coupled Plasma Mass Spectroscopy after Cloud-Point Extraction and in Situ Labeling of Gold Nanoparticles.” *Environmental Science and Technology* 55 (8): 4783–91. https://doi.org/10.1021/ACS.EST.0C06839/SUPPL_FILE/ES0C06839_SI_001.PDF.

Lambert, Scott, and Martin Wagner. 2016. “Characterisation of Nanoplastics during the Degradation of Polystyrene.” *Chemosphere* 145 (February): 265–68. https://doi.org/10.1016/J.CHEMOSPHERE.2015.11.078.

Lang-Yona, N., Y. Rudich, E. Segre, E. Dinar, and A. Abo-Riziq. 2009. “Complex Refractive Indices of Aerosols Retrieved by Continuous Wave-Cavity Ring down Aerosol Spectrometer.” *Analytical Chemistry* 81 (5): 1762–69. https://doi.org/10.1021/ac8017789.

Lehmann, Moritz, Lisa Marie Oehlschlägel, Fabian P. Häusl, Andreas Held, and Stephan Gekle. 2021. “Ejection of Marine Microplastics by Raindrops: A Computational and Experimental Study.” *Microplastics and Nanoplastics 2021 1:1* 1 (1): 1–19. https://doi.org/10.1186/S43591-021-00018-8.

Li, Zhigang, and Hai Wang. 2003. “Drag Force, Diffusion Coefficient, and Electric Mobility of Small Particles. I. Theory Applicable to the Free-Molecule Regime.” *Physical Review E* 68 (6): 061206. https://doi.org/10.1103/PhysRevE.68.061206.

Lintis, Laura, François Xavier Ouf, Philippe Parent, Daniel Ferry, Carine Laffon, and Cécile Vallières. 2021. “Quantification and Prediction of Water Uptake by Soot Deposited on Ventilation Filters during Fire Events.” *Journal of Hazardous Materials* 403 (February): 123916. https://doi.org/10.1016/J.JHAZMAT.2020.123916.

Liu, Kai, Tianning Wu, Xiaohui Wang, Zhangyu Song, Changxing Zong, Nian Wei, and Daoji Li. 2019. “Consistent Transport of Terrestrial Microplastics to the Ocean through Atmosphere.” *Environmental Science and Technology* 53 (18): 10612–19. https://doi.org/10.1021/ACS.EST.9B03427/SUPPL_FILE/ES9B03427_SI_002.PDF.

Longest, P. Worth, and Michael Hindle. 2012. “Condensational Growth of Combination Drug-Excipient Submicrometer Particles for Targeted High Efficiency Pulmonary Delivery: Comparison of CFD Predictions with Experimental Results.” *Pharmaceutical Research* 29 (3): 707–21. https://doi.org/10.1007/s11095-011-0596-1.

Longest, P. Worth, Geng Tian, and Michael Hindle. 2011. “Improving the Lung Delivery of Nasally Administered Aerosols during Noninvasive Ventilation-An Application of Enhanced Condensational Growth (ECG).” *Journal of Aerosol Medicine and Pulmonary Drug Delivery* 24 (2): 103–18. https://doi.org/10.1089/jamp.2010.0849.

Ma, Yini, Anna Huang, Siqi Cao, Feifei Sun, Lianhong Wang, Hongyan Guo, and Rong Ji. 2016. “Effects of Nanoplastics and Microplastics on Toxicity, Bioaccumulation, and Environmental Fate of Phenanthrene in Fresh Water.” *Environmental Pollution* 219 (December): 166–73. https://doi.org/10.1016/j.envpol.2016.10.061.

Maláč, J., V. Altmann, and J. Zelinger. 1970. “Properties of PVC. II. Properties of PVC Compounds with Solvents.” *Journal of Applied Polymer Science* 14 (1): 161–73. https://doi.org/10.1002/APP.1970.070140116.

Malcolmson, Richard J., and Jonathan K. Embleton. 1998. “Dry Powder Formulations for Pulmonary Delivery.” *Pharmaceutical Science and Technology Today*. Elsevier Current Trends. https://doi.org/10.1016/S1461-5347(98)00099-6.

Malek, Kotiba A., Kanishk Gohil, Hind A. Al-Abadleh, and Akua A. Asa-Awuku. 2022. “Hygroscopicity of Polycatechol and Polyguaiacol Secondary Organic Aerosol in Sub- and Supersaturated Water Vapor Environments.” *Environmental Science: Atmospheres* 2 (1): 24–33. https://doi.org/10.1039/D1EA00063B.

Mamakos, Athanasios. 2016. “Methodology to Quantify the Ratio of Multiple-to Single-Charged Fractions Acquired in Aerosol Neutralizers.” *Aerosol Science and Technology* 50 (4): 363–72. https://doi.org/10.1080/02786826.2016.1153034.

Man, Nin Chan, Sonia M. Kreidenweis, and Chak K. Chan. 2008. “Measurements of the Hygroscopic and Deliquescence Properties of Organic Compounds of Different

Solubilities in Water and Their Relationship with Cloud Condensation Nuclei Activities." *Environmental Science and Technology* 42 (10): 3602–8. https://doi.org/10.1021/es7023252.

Mao, Chun-Ning, Kanishk Gohil, and Akua A. Asa-Awuku. 2022. "A Single-Parameter Hygroscopicity Model for Functionalized Insoluble Aerosol Surfaces." *Atmospheric Chemistry and Physics* 22 (19): 13219–28. https://doi.org/10.5194/ACP-22-13219-2022.

Mao, Chun Ning, Kotiba A. Malek, and Akua Asa-Awuku. 2021. "Hygroscopicity and the Water-Polymer Interaction Parameter of Nano-Sized Biodegradable Hydrophilic Substances." *Aerosol Science and Technology* 55 (10): 1115–24. https://doi.org/10.1080/02786826.2021.1931012.

Marple, Virgil A., and Klaus Willeke. 1976. "Impactor Design." *Atmospheric Environment (1967)* 10 (10): 891–96. https://doi.org/10.1016/0004-6981(76)90144-X.

Mason, Bernard J., Simon John King, Rachael E.H. Miles, Katherine M. Manfred, Andrew M.J. Rickards, Jin Kim, Jonathan P. Reid, and Andrew J. Orr-Ewing. 2012. "Comparison of the Accuracy of Aerosol Refractive Index Measurements from Single Particle and Ensemble Techniques." *Journal of Physical Chemistry A* 116 (33): 8547–56. https://doi.org/10.1021/jp3049668.

Massling, A., M. Stock, and A. Wiedensohler. 2005. "Diurnal, Weekly, and Seasonal Variation of Hygroscopic Properties of Submicrometer Urban Aerosol Particles."

Atmospheric Environment 39 (21): 3911–22. https://doi.org/10.1016/J.ATMOSENV.2005.03.020.

McCall, David W., Dean C. Douglass, Lee L. Blyler, G. Edward Johnson, Lynn W. Jelinski, and Harvey E. Bair. 1984. "Solubility and Diffusion of Water in Low-Density Polyethylene." *Macromolecules* 17 (9): 1644–49. https://doi.org/10.1021/ma00139a001.

Medronho, Bruno, Anabela Romano, Maria Graça Miguel, Lars Stigsson, and Björn Lindman. 2012. "Rationalizing Cellulose (in)Solubility: Reviewing Basic Physicochemical Aspects and Role of Hydrophobic Interactions." *Cellulose* 19 (3): 581–87. https://doi.org/10.1007/s10570-011-9644-6.

"Microplastics in Drinking-Water." n.d., 101.

Miles, Rachael E. H., Svemir Rudić, Andrew J. Orr-Ewing, and Jonathan P. Reid. 2011. "Sources of Error and Uncertainty in the Use of Cavity Ring Down Spectroscopy to Measure Aerosol Optical Properties." *Aerosol Science and Technology* 45 (11): 1360–75. https://doi.org/10.1080/02786826.2011.596170.

Mohana, Anika Amir, S. M. Farhad, Nawshad Haque, and Biplob Kumar Pramanik. 2021. "Understanding the Fate of Nano-Plastics in Wastewater Treatment Plants and Their Removal Using Membrane Processes." *Chemosphere* 284 (December): 131430. https://doi.org/10.1016/J.CHEMOSPHERE.2021.131430.

Moore, Richard H., Athanasios Nenes, and Jeessy Medina. 2010. "Scanning Mobility CCN

Analysis—A Method for Fast Measurements of Size-Resolved CCN Distributions and Activation Kinetics." *Aerosol Science and Technology* 44 (10): 861–71. https://doi.org/10.1080/02786826.2010.498715.

Moosmüller, H., R. K. Chakrabarty, and W. P. Arnott. 2009. "Aerosol Light Absorption and Its Measurement: A Review." *Journal of Quantitative Spectroscopy and Radiative Transfer*. Pergamon. https://doi.org/10.1016/j.jqsrt.2009.02.035.

Munari, Cristina, Vanessa Infantini, Marco Scoponi, Eugenio Rastelli, Cinzia Corinaldesi, and Michele Mistri. 2017. "Microplastics in the Sediments of Terra Nova Bay (Ross Sea, Antarctica)." *Marine Pollution Bulletin* 122 (1–2): 161–65. https://doi.org/10.1016/j.marpolbul.2017.06.039.

Muralidharan, Priya, Monica Malapit, Evan Mallory, Don Hayes, and Heidi M. Mansour. 2015. "Inhalable Nanoparticulate Powders for Respiratory Delivery." *Nanomedicine: Nanotechnology, Biology, and Medicine*. Elsevier Inc. https://doi.org/10.1016/j.nano.2015.01.007.

Napolitano, Simone, and Michael Wübbenhorst. 2011. "The Lifetime of the Deviations from Bulk Behaviour in Polymers Confined at the Nanoscale." *Nature Communications* 2 (1): 1–7. https://doi.org/10.1038/ncomms1259.

Navea, Juan G., Emily Richmond, Talia Stortini, and Jillian Greenspan. 2017. "Water Adsorption Isotherms on Fly Ash from Several Sources." *Langmuir* 33 (39): 10161–71.

https://doi.org/10.1021/acs.langmuir.7b02028.

O'Keefe, Anthony, and David A.G. Deacon. 1988. "Cavity Ring-down Optical Spectrometer for Absorption Measurements Using Pulsed Laser Sources." *Review of Scientific Instruments* 59 (12): 2544–51. https://doi.org/10.1063/1.1139895.

Ottewill, R. H., and B. Vincent. 1972. "Colloid and Surface Chemistry of Polymer Latices. Part 1.—Adsorption and Wetting Behaviour of n-Alkanols." *Journal of the Chemical Society, Faraday Transactions 1: Physical Chemistry in Condensed Phases* 68 (0): 1533–43. https://doi.org/10.1039/F19726801533.

Pajunoja, Aki, Andrew T. Lambe, Jani Hakala, Narges Rastak, Molly J. Cummings, James F. Brogan, Liqing Hao, et al. 2015. "Adsorptive Uptake of Water by Semisolid Secondary Organic Aerosols." *Geophysical Research Letters* 42 (8): 3063–68. https://doi.org/10.1002/2015GL063142.

Peng, Chao, Kotiba A. Malek, Dewansh Rastogi, Yuqing Zhang, Weigang Wang, Xiang Ding, Akua A. Asa-Awuku, Xinming Wang, and Mingjin Tang. 2022. "Hygroscopicity and Cloud Condensation Nucleation Activities of Hydroxyalkylsulfonates." *Science of The Total Environment* 830 (July): 154767. https://doi.org/10.1016/J.SCITOTENV.2022.154767.

Peng, Chao, Patricia N. Razafindrambinina, Kotiba A. Malek, Lanxiadi Chen, Weigang Wang, Ru Jin Huang, Yuqing Zhang, et al. 2021. "Interactions of Organosulfates with

Water Vapor under Sub- And Supersaturated Conditions." *Atmospheric Chemistry and Physics* 21 (9): 7135–48. https://doi.org/10.5194/ACP-21-7135-2021.

Pethrick, RA. 2004. *Polymer Physics. Edited by Michael Rubinstein and Ralph H Colby Oxford University Press, Oxford, 2003. ISBN 019852059X. Pp 440*. *Polymer International*. Vol. 53. Wiley. https://doi.org/10.1002/PI.1472.

Petters, M. D., and S. M. Kreidenweis. 2007. "A Single Parameter Representation of Hygroscopic Growth and Cloud Condensation Nucleus Activity." *Atmospheric Chemistry and Physics* 7 (8): 1961–71. https://doi.org/10.5194/acp-7-1961-2007.

———. 2008. "A Single Parameter Representation of Hygroscopic Growth and Cloud Condensation Nucleus Activity - Part 2: Including Solubility." *Atmospheric Chemistry and Physics* 8 (20): 6273–79. https://doi.org/10.5194/ACP-8-6273-2008.

Petters, M. D., S. M. Kreidenweis, A. J. Prenni, R. C. Sullivan, C. M. Carrico, K. A. Koehler, and P. J. Ziemann. 2009. "Role of Molecular Size in Cloud Droplet Activation." *Geophysical Research Letters* 36 (22): L22801. https://doi.org/10.1029/2009GL040131.

Petters, Markus D., Sonia M. Kreidenweis, Jefferson R. Snider, Kirsten A. Koehler, Qiang Wang, Anthony J. Prenni, and Paul J. Demott. 2006. "Cloud Droplet Activation of Polymerized Organic Aerosol." *Tellus B: Chemical and Physical Meteorology* 58 (3): 196–205. https://doi.org/10.1111/j.1600-0889.2006.00181.x.

Pettersson, Anders, Edward R. Lovejoy, Charles A. Brock, Steven S. Brown, and A. R.

Ravishankara. 2004. “Measurement of Aerosol Optical Extinction at 532 Nm with Pulsed Cavity Ring down Spectroscopy.” *Journal of Aerosol Science* 35 (8): 995–1011. https://doi.org/10.1016/j.jaerosci.2004.02.008.

Pöschl, Ulrich. 2005. “Atmospheric Aerosols: Composition, Transformation, Climate and Health Effects.” *Angewandte Chemie International Edition* 44 (46): 7520–40. https://doi.org/10.1002/ANIE.200501122.

Prata, Joana Correia. 2018. “Airborne Microplastics: Consequences to Human Health?” *Environmental Pollution*. Elsevier Ltd. https://doi.org/10.1016/j.envpol.2017.11.043.

Puxbaum, Hans, and Monika Tenze-Kunit. 2003. “Size Distribution and Seasonal Variation of Atmospheric Cellulose.” *Atmospheric Environment* 37 (26): 3693–99. https://doi.org/10.1016/S1352-2310(03)00451-5.

Radney, James G., Xiaofei Ma, Keith A. Gillis, Michael R. Zachariah, Joseph T. Hodges, and Christopher D. Zangmeister. 2013. “Direct Measurements of Mass-Specific Optical Cross Sections of Single-Component Aerosol Mixtures.” *Analytical Chemistry* 85 (17): 8319–25. https://doi.org/10.1021/ac401645y.

Radney, James G., and Christopher D. Zangmeister. 2016. “Practical Limitations of Aerosol Separation by a Tandem Differential Mobility Analyzer-Aerosol Particle Mass Analyzer.” *Aerosol Science and Technology* 50 (2): 160–72. https://doi.org/10.1080/02786826.2015.1136733.

———. 2018. “Comparing Aerosol Refractive Indices Retrieved from Full Distribution and Size- and Mass-Selected Measurements.” *Journal of Quantitative Spectroscopy and Radiative Transfer* 220 (November): 52–66. https://doi.org/10.1016/j.jqsrt.2018.08.021.

Raheem, Dele. 2013. “APPLICATION OF PLASTICS AND PAPER AS FOOD PACKAGING MATERIALS - AN OVERVIEW.” *Emirates Journal of Food and Agriculture* 25 (3): 177–88. https://doi.org/10.9755/EJFA.V25I3.11509.

Reitz, P., C. Spindler, T. F. Mentel, L. Poulain, H. Wex, K. Mildenberger, D. Niedermeier, et al. 2011. “Surface Modification of Mineral Dust Particles by Sulphuric Acid Processing: Implications for Ice Nucleation Abilities.” *Atmospheric Chemistry and Physics* 11 (15): 7839–58. https://doi.org/10.5194/ACP-11-7839-2011.

Roberts, G. C., and A. Nenes. 2005. “A Continuous-Flow Streamwise Thermal-Gradient CCN Chamber for Atmospheric Measurements.” *Aerosol Science and Technology* 39 (3): 206–21. https://doi.org/10.1080/027868290913988.

Rose, D., S. S. Gunthe, E. Mikhailov, G. P. Frank, U. Dusek, M. O. Andreae, and U. Pöschl. 2008. “Calibration and Measurement Uncertainties of a Continuous-Flow Cloud Condensation Nuclei Counter (DMT-CCNC): CCN Activation of Ammonium Sulfate and Sodium Chloride Aerosol Particles in Theory and Experiment.” *Atmospheric Chemistry and Physics* 8 (5): 1153–79. https://doi.org/10.5194/ACP-8-1153-2008.

Seifali Abbas-Abadi, Mehrdad, Mehdi Nekoomanesh Haghighi, Armando G. McDonald, and

Hamid Yeganeh. 2015. “Estimation of Pyrolysis Product of LDPE Degradation Using Different Process Parameters in a Stirred Reactor.” *Polyolefins Journal* 2 (1): 39–47. https://doi.org/10.22063/POJ.2015.1102.

Seinfeld, John H., Spyros N. Pandis, and Kevin Noone. 1998. “Atmospheric Chemistry and Physics: From Air Pollution to Climate Change.” *Physics Today* 51 (10): 88–90. https://doi.org/10.1063/1.882420.

Shah, Aamer Ali, Fariha Hasan, Abdul Hameed, and Safia Ahmed. 2008. “Biological Degradation of Plastics: A Comprehensive Review.” *Biotechnology Advances* 26 (3): 246–65. https://doi.org/10.1016/J.BIOTECHADV.2007.12.005.

Shelly, M. P., G. M. Lloyd, and G. R. Park. 1988. “A Review of the Mechanisms and Methods of Humidification of Inspired Gases.” *Intensive Care Medicine*. Springer-Verlag. https://doi.org/10.1007/BF00254114.

Singh, D P, Marie-Hélène Zérah, Ram B Bhagat, Gavin W Jones, Navtej Nainan, Leela Fernandes, F O R Official, et al. 2007. “Employment Situation in Mumbai : An Analysis.” *Economic and Political Weekly* 42 (2): 758–75. http://www.sciencedirect.com:5070/referencework/9780122274107/encyclopedia-of-physical-science-and-technology.

Singh, Sujeeta, Marc N. Fiddler, Damon Smith, and Solomon Bililign. 2014. “Error Analysis and Uncertainty in the Determination of Aerosol Optical Properties Using Cavity Ring-

down Spectroscopy, Integrating Nephelometry, and the Extinction-Minus-Scattering Method." *Aerosol Science and Technology* 48 (12): 1345–59. https://doi.org/10.1080/02786826.2014.984062.

Sökmen, Teoman Özgür, Ekrem Sulukan, Medine Türkoğlu, Alper Baran, Mustafa Özkaraca, and Saltuk Buğrahan Ceyhun. 2020. "Polystyrene Nanoplastics (20 Nm) Are Able to Bioaccumulate and Cause Oxidative DNA Damages in the Brain Tissue of Zebrafish Embryo (Danio Rerio)." *NeuroToxicology* 77 (March): 51–59. https://doi.org/10.1016/j.neuro.2019.12.010.

Sorjamaa, R., and A. Laaksonen. 2007a. "The Effect of H2O Adsorption on Cloud Drop Activation of Insoluble Particles: A Theoretical Framework." *Atmospheric Chemistry and Physics* 7 (24): 6175–80. https://doi.org/10.5194/ACP-7-6175-2007.

Sorjamaa, R, and A Laaksonen. 2007b. "The Effect of H 2 O Adsorption on Cloud Drop Activation of Insoluble Particles: A Theoretical Framework." *Atmos. Chem. Phys.* Vol. 7. www.atmos-chem-phys.net/7/6175/2007/.

Stolzenburg, Mark R., and Peter H. McMurry. 2007. "An Ultrafine Aerosol Condensation Nucleus Counter." *Http://Dx.Doi.Org/10.1080/02786829108959470* 14 (1): 48–65. https://doi.org/10.1080/02786829108959470.

Sullivan, G. L., J. Delgado Gallardo, E. W. Jones, P. J. Hollliman, T. M. Watson, and S. Sarp. 2020. "Detection of Trace Sub-Micron (Nano) Plastics in Water Samples Using

Pyrolysis-Gas Chromatography Time of Flight Mass Spectrometry (PY-GCToF)." *Chemosphere* 249 (June): 126179. https://doi.org/10.1016/J.CHEMOSPHERE.2020.126179.

Sullivan, R. C., M. D. Petters, P. J. Demott, S. M. Kreidenweis, H. Wex, D. Niedermeier, S. Hartmann, et al. 2010. "Irreversible Loss of Ice Nucleation Active Sites in Mineral Dust Particles Caused by Sulphuric Acid Condensation." *Atmospheric Chemistry and Physics* 10 (23): 11471–87. https://doi.org/10.5194/ACP-10-11471-2010.

Sullivan, R C, M J K Moore, M D Petters, S M Kreidenweis, G C Roberts, and K A Prather. 2009. "Atmospheric Chemistry and Physics Effect of Chemical Mixing State on the Hygroscopicity and Cloud Nucleation Properties of Calcium Mineral Dust Particles." *Atmos. Chem. Phys.* Vol. 9. www.atmos-chem-phys.net/9/3303/2009/.

Tajima-Hatashita, Naoko. 2013. "DEVELOPMENT AND PERFORMANCE EVALUATION OF AEROSOL PARTICLE MASS ANALYZER(APM)." https://ci.nii.ac.jp/naid/500000730433.

Tang, Mingjin, Chak K. Chan, Yong Jie Li, Hang Su, Qingxin Ma, Zhijun Wu, Guohua Zhang, et al. 2019. "A Review of Experimental Techniques for Aerosol Hygroscopicity Studies." *Atmospheric Chemistry and Physics* 19 (19): 12631–86. https://doi.org/10.5194/acp-19-12631-2019.

Tang, Mingjin, Daniel J. Cziczo, and Vicki H. Grassian. 2016. "Interactions of Water with

Mineral Dust Aerosol: Water Adsorption, Hygroscopicity, Cloud Condensation, and Ice Nucleation." *Chemical Reviews* 116 (7): 4205–59. https://doi.org/10.1021/ACS.CHEMREV.5B00529.

Tigges, L., A. Wiedensohler, K. Weinhold, J. Gandhi, and H. J. Schmid. 2015. "Bipolar Charge Distribution of a Soft X-Ray Diffusion Charger." *Journal of Aerosol Science* 90 (December): 77–86. https://doi.org/10.1016/j.jaerosci.2015.07.002.

Tiseo, Ian. 2021. "Plastics Industry in the U.S." *Statista*. https://www.statista.com/topics/7460/plastics-industry-in-the-us/#topicHeader__wrapper.

Toole, Justin R., Lindsay Renbaum-Wolff, and Geoffrey D. Smith. 2013. "A Calibration Technique for Improving Refractive Index Retrieval from Aerosol Cavity Ring-down Spectroscopy." *Aerosol Science and Technology* 47 (9): 955–65. https://doi.org/10.1080/02786826.2013.805875.

Visalakshi, N. A., T. T. Mariappan, Hemant Bhutani, and Saranjit Singh. 2005. "Behavior of Moisture Gain and Equilibrium Moisture Contents (EMC) of Various Drug Substances and Correlation with Compendial Information on Hygroscopicity and Loss on Drying." *Pharmaceutical Development and Technology* 10 (4): 489–97. https://doi.org/10.1080/10837450500299883.

Vu, Diep, Shaokai Gao, Tyler Berte, Mary Kacarab, Qi Yao, Kambiz Vafai, and Akua Asa-

Awuku. 2019. “External and Internal Cloud Condensation Nuclei (CCN) Mixtures: Controlled Laboratory Studies of Varying Mixing States.” *Atmospheric Measurement Techniques* 12 (8): 4277–89. https://doi.org/10.5194/amt-12-4277-2019.

Vu, Tuan V., Juana Maria Delgado-Saborit, and Roy M. Harrison. 2015. “A Review of Hygroscopic Growth Factors of Submicron Aerosols from Different Sources and Its Implication for Calculation of Lung Deposition Efficiency of Ambient Aerosols.” *Air Quality, Atmosphere and Health* 8 (5): 429–40. https://doi.org/10.1007/s11869-015-0365-0.

Wang, Shih Chen, and Richard C. Flagan. 1990. “Scanning Electrical Mobility Spectrometer.” *Aerosol Science and Technology* 13 (2): 230–40. https://doi.org/10.1080/02786829008959441.

Weinmüller, C., C. Langel, F. Fornasiero, C. J. Radke, and J. M. Prausnitz. 2006. “Sorption Kinetics and Equilibrium Uptake for Water Vapor in Soft-Contact-Lens Hydrogels.” *Journal of Biomedical Materials Research - Part A* 77 (2): 230–41. https://doi.org/10.1002/jbm.a.30598.

Wiedensohler, A. 1988. “An Approximation of the Bipolar Charge Distribution for Particles in the Submicron Size Range.” *Journal of Aerosol Science* 19 (3): 387–89. https://doi.org/10.1016/0021-8502(88)90278-9.

Williams, J, M De Reus, R Krejci, H Fischer, and J Ström. 2002. “Atmospheric Chemistry

and Physics Application of the Variability-Size Relationship to Atmospheric Aerosol Studies: Estimating Aerosol Lifetimes and Ages." *Atmos. Chem. Phys* 2: 133–45. www.atmos-chem-phys.org/acp/2/133/.

Winklmayr, W., G. P. Reischl, A. O. Lindner, and A. Berner. 1991. "A New Electromobility Spectrometer for the Measurement of Aerosol Size Distributions in the Size Range from 1 to 1000 Nm." *Journal of Aerosol Science* 22 (3): 289–96. https://doi.org/10.1016/S0021-8502(05)80007-2.

Wolf, Bernhard A. 2003. "Chain Connectivity and Conformational Variability of Polymers: Clues to an Adequate Thermodynamic Description of Their Solutions, 2." *Macromolecular Chemistry and Physics* 204 (11): 1381–90. https://doi.org/10.1002/macp.200350002.

Yang, Tong, Jialuo Luo, and Bernd Nowack. 2021. "Characterization of Nanoplastics, Fibrils, and Microplastics Released during Washing and Abrasion of Polyester Textiles." *Environmental Science and Technology* 55 (23): 15873–81. https://doi.org/10.1021/ACS.EST.1C04826/SUPPL_FILE/ES1C04826_SI_001.PDF.

Yin, Kai, Yu Wang, Hongjing Zhao, Dongxu Wang, Menghao Guo, Mengyao Mu, Yachen Liu, et al. 2021. "A Comparative Review of Microplastics and Nanoplastics: Toxicity Hazards on Digestive, Reproductive and Nervous System." *Science of The Total Environment* 774 (June): 145758. https://doi.org/10.1016/J.SCITOTENV.2021.145758.

Zangmeister, Christopher D., James G. Radney, Kurt D. Benkstein, and Berc Kalanyan. 2022a. “Common Single-Use Consumer Plastic Products Release Trillions of Sub-100 Nm Nanoparticles per Liter into Water during Normal Use.” *Environmental Science & Technology*, April. https://doi.org/10.1021/ACS.EST.1C06768.

———. 2022b. “Common Single-Use Consumer Plastic Products Release Trillions of Sub-100 Nm Nanoparticles per Liter into Water during Normal Use.” *Environmental Science & Technology* 56 (9): 5448–55. https://doi.org/10.1021/ACS.EST.1C06768.

Zarzana, Kyle J., Christopher D. Cappa, and Margaret A. Tolbert. 2014. “Sensitivity of Aerosol Refractive Index Retrievals Using Optical Spectroscopy.” *Aerosol Science and Technology* 48 (11): 1133–44. https://doi.org/10.1080/02786826.2014.963498.

Zhang, Q., J. L. Jimenez, M. R. Canagaratna, J. D. Allan, H. Coe, I. Ulbrich, M. R. Alfarra, et al. 2007. “Ubiquity and Dominance of Oxygenated Species in Organic Aerosols in Anthropogenically-influenced Northern Hemisphere Midlatitudes.” *Geophysical Research Letters* 34 (13). https://doi.org/10.1029/2007GL029979@10.1002/(ISSN)1944-8007.GRL40.

Zhang, Xiaoning, Jun Qiu, Jun Qiu, Jun Qiu, Xingcan Li, Xingcan Li, Junming Zhao, Junming Zhao, Linhua Liu, and Linhua Liu. 2020. “Complex Refractive Indices Measurements of Polymers in Visible and Near-Infrared Bands.” *Applied Optics, Vol. 59, Issue 8, Pp. 2337-2344* 59 (8): 2337–44. https://doi.org/10.1364/AO.383831.